AN EXPERIMENTAL INVESTIGATION OF THE HARDENABILITY, TENSILE AND FRACTURE PROPERTIES OF POWDERED METAL STEELS

by

Paul G. Tallon

A thesis

Submitted to the faculty of the

Materials Engineering: McMaster University

in partial fulfillment of the requirements for the degree of

Master of Applied Science

in

Materials Science and Engineering

Dr. Dmitri V. Malakhov, Supervisor

Professor, Materials Science of Engineering

MASTER OF APPLIED SCIENCE (2018) McMaster University

(Materials Science & Engineering) Hamilton, Ontario, Canada

TITLE: An Experimental Investigation of the Hardenability, Tensile and Fracture Properties of Powder Metal Steels

AUTHOR: Paul G. Tallon, B.Eng (McMaster University)

SUPERVISOR: Professor Dmitri V. Malakhov

NUMBER OF PAGES: XIV, 135

Abstract

Powder metallurgy (PM) steel is produced by near net shape manufacturing, which is used to fabricate alloy steels for many purposes. Designing new powder metal steels that can form a significant fraction of martensite relies on hardenability calculations developed for wrought steels. These proven tools are built upon assumptions for wrought steels that do not hold true for PM steels. One assumption is that the alloying elements are homogenized throughout the material. In admixed powder blends that are industrially sintered this is not the case. Using prealloyed powder is a solution to this issue, yet it places restrictions on alloy design and compressibility. There are tools available to computationally optimize diffusion problems, yet the complexity during the sintering of PM steel is such that a robust model has yet been produced. It is intuitive that with smaller particles of Fe sintering time can be reduced. A direct experimental investigation linking Fe-powders' sizes and hardenability on Fe-C-Cr-Mn-Mo-Ni PM steel was subject to microstructure analysis and mechanical properties (Jominy test) for comparative analysis.

Another assumption that is made for wrought steel is a consistent density of 7.87g/cm^3. This is not the case for PM steel as the press and sinter method produces pores, decreasing the density. This directly affects the thermal conductivity and phase transformation of the steel. In an effort to understand how these differences affect Grossmann's predictions of hardenability, a direct experimental investigation linking the density to hardenability was launched on prealloyed FL-4605 and FL-4605+2%Cu. Specifically the Jominy test was completed on a range of densities, as well as compared to software predictions.

The chemical variations in admixed and sintered PM steel produce a unique system where one TTT diagram cannot predict the entire final microstructure. PM steel such as this is observed in industry, and can be created through incorporating larger Fe-particles such that less alloying constituents have a chance to fully alloy these regions. Since the large

particles will not have the chance to be alloyed, they will not have the ability to form martensite. Since the regions between large particles will be alloyed, martensite will form, creating a hard matrix surrounding softer particles. This structure is characteristic of a metal matrix composite (MMC), and therefore should be treated as such. There are methods of MMC design that involve numerical methods of predicting strength and toughness. These methods, along with experimental data (tensile and Charpy testing) of Fe-C-Cr-Mn-Mo-Ni PM steels with ranging volume fractions of pearlitic inclusions were compared.

Acknowledgments

I am profoundly grateful to my supervisor, Dr. Dmitri Malakhov for his never-ending support and guidance that has had the ability to push my knowledge farther than I ever thought possible.

I would also like to extend my deepest gratitude to Roger Lawcock for his valuable advice, and expertise throughout this research program. I would also like to express my gratitude to Dr. Malakhov and Roger Lawcock for providing me with this opportunity to carry out this research.

I would like to thank the Ontario Center for Excellence and Stackpole International for the financial support during the project.

I am also so very grateful to my colleagues and friends within the Materials Science and Engineering Department who made my academic journey so fruitful, memorable and enjoyable.

Contents

List of Figures

List of Tables

List of Abbreviations and Symbols

Symbol	Definition	Unit
M_S	Martensite start temperature	ºC
DI	Ideal diameter	m
H	Severity of quench	m^{-1}
h	Heat transfer coefficient	W/m^2K
λ	Thermal conductivity	W/mK
α	Thermal diffusivity	m^2/s
ε	Void fraction	%
K_{1C}	Fracture toughness	$Mpam^{1/2}$
E	Elastic modulus	Mpa
σ_y	Yield strength	Mpa
d	Particle diameter	m
ρ_C	Target density	g/cm^3
ρ_P	Apparent density	g/cm^3
h_C	Compacted height	Cm
h_P	Die depth	cm

Abbreviation	Definition
PM	Powder metallurgy
PMS	Powder metal steel
TTT	Time-temperature-transformation
CCT	Continuous-cooling-transformation
BCT	Body centered tetragonal
FCC	Face centred cubic
BCC	Body cantered Cubic
OFHC	Oxygen free high conductivity

1: INTRODUCTION

1.1. Background on Powder Metallurgy

As of 2005, 80% by weight of “structural precision parts” were produced from ferrous and nonferrous powder metals, and 75% of these were manufactured for the transportation-automotive industry [3]. Industrial expectations are set high for these parts, where they must abide by strict dimensional tolerances. It is also imperative to have consistent mechanical properties (tensile strength, fracture toughness, fatigue strength etc.)

There are a number of different ways to produce powder metal parts in industry, with minute and large differences in the process where different powders are used to create different geometries and densities. For the purpose of this thesis only one methodology will be considered which is the press and sinter method to produce PM steel. A more in-depth representation of the industrial model can be seen in Figure 1.

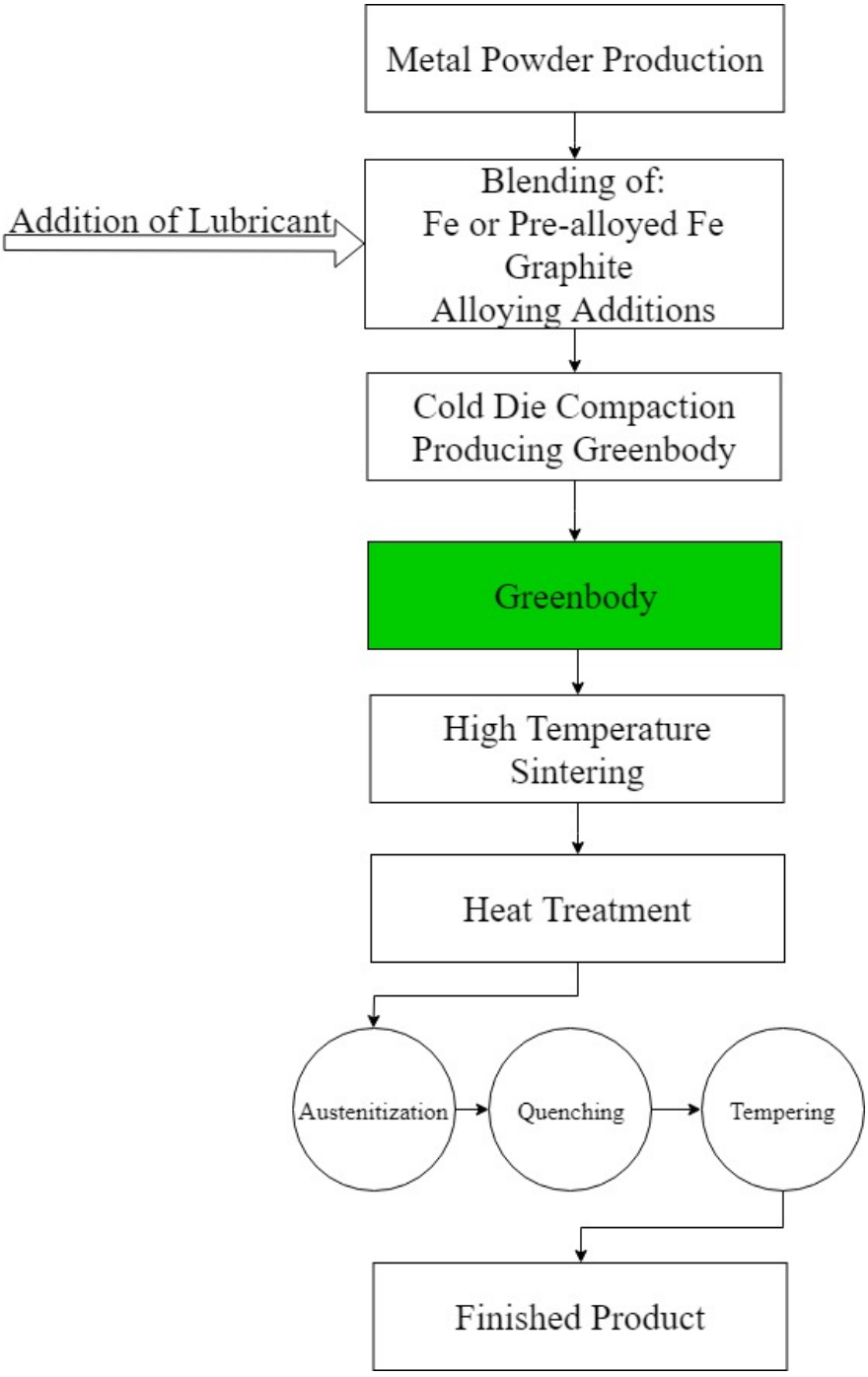

Figure 1: Flow chart of basic steps to PM process

The finely distributed metallic solids, or powder, go through multiple steps so that it is ready to be used by PM steel manufacturers. The powder must be pure, relatively soft and fit within a specific size distribution for the application. For example finer powder is commonly used in hot isostatic pressing [2].

The metal powder is then blended to produce as uniform a mixture as possible before compaction. In room temperature (or cold die compaction) the die is filled with powder and uniaxially compacted into a greenbody part. The greenbody is then sintered at below full melting temperatures of the material to produce a consolidated matrix. Further heat-treating is common in industry to produce targeted mechanical properties [2].

The ability to process the metal powder is directly related to the apparent density, compressibility, and flowability of the powder. For this reason the size distribution has been specified as one of the most important characteristics of powders used by industry [2].

1.2. Apparent density

The apparent density of a powder is defined as the amount of volume a specific mass of powder takes up, and is found via industrialized standard methods [2], [4]. This characteristic is crucial in determining the die dimensions, where the final target density ρ_c and compact height h_c can be used along with the apparent density ρ_p of the powder to calculate the depth the die must be h_p. This can be seen in(1).

(1) $$\frac{\rho_c}{\rho_p} h_c = h_p$$

1.3. Compressibility

Compressibility will relate to the final density of the part, and therefore very closely linked to the final mechanical properties. A powder is said to be compressible if under a relatively realistic load it can be compacted to a high density, producing a greenbody compact with high strength. The properties of the particles (shape, density, hardness, composition, size) are directly related to the compressibility. Smooth, highly dense, soft, and pure bi-model size distributed powders are more compressible [2], [5].

1.4. Flowability

The ability to fill a die quickly and properly is a sought after powder property, which is described by the flowability of a given powder. This is a crucial characteristic that must be known for PM steel production. Before a new powder blend can be implemented into the industrial process, this characteristic and compressibility must be known so it can be used properly in the process. It is important to note that lubricant is added to increase the flowability, and compressibility of metal powder blends.

Despite the dominating influence of the base iron powder, the alloying powders used will also have an effect on these properties. This connection has led to different methodologies of adding alloying elements to ferrous blends, each having strengths and weaknesses, these methods are outlined below [6].

- Admixed: The alloying elemental powders are added to an iron base powder, to then be mixed in an effort to create a homogenous assortment of constituents [6], [7]. This method is common because of the lower price point. The PM steel will have compositional modulations due to the limitations of solid-state diffusivity

during the sintering process. Powder segregation and agglomeration is also a possibility depending on the method of mixing the powder blend [6], [8].

- Prealloyed: The alloying elements are mixed with the base element in the liquid state and then atomized. This produces a more homogenous powder mixture, and therefore the final form of the PM steel is also more uniform in its composition and microstructure yet has poor compressibility [6] [9].
- FerroAlloys: Powders that are produced through the combination of a specific alloying element and iron. This allows for less noble metal, like molybdenum or chromium to be added to admixed powder blends without the presence of oxides.
- Master Alloys: This method is accomplished by creating a liquid melt of specific alloying elements that correspond to the final target composition of the steel, and then atomised. This powder is then admixed to a powder blend with iron, graphite to be formed into PM steel.
- Hybrids: These powder blends are defined as admixing the different kind of powders expressed above. For example ferroalloy molybdenum will be mixed with iron and elemental powders to form a completed blend [8].

1.5. Sintering

Once a compact or greenbody has been produced the part is loaded into the furnace for sintering, an example is shown in Figure 2. The pre-heat zone is where temperatures are such that the lubricant can vaporize and leave the PM greenbody, yet not high enough to start sintering. The high-heat zone is where sintering starts [11]. Sintering can be a complete solid phase process or include the formation of some liquid phase, depending on the constituents of the steel. This occurs through mass transport and controlled by the increase in temperature [2].

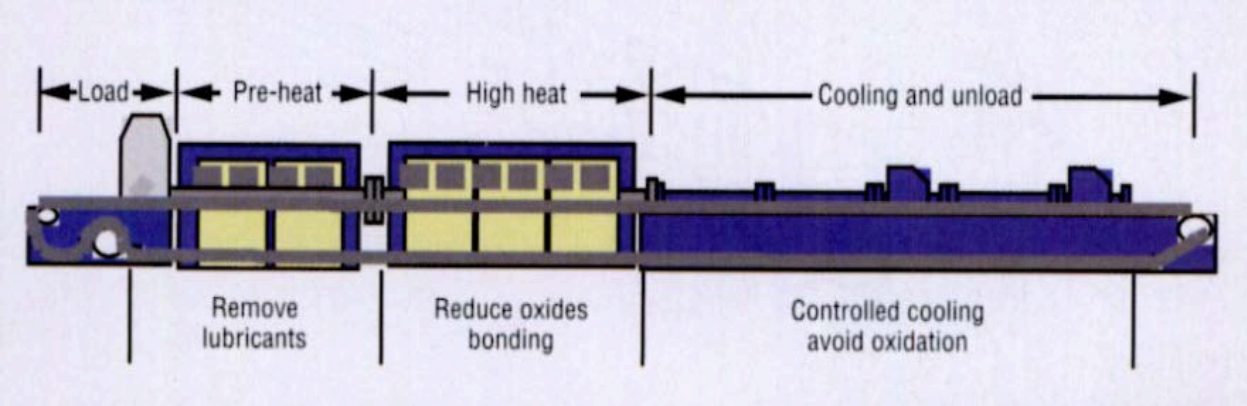

Figure 2: General Belt Sintering Furnace for PM Parts [11]

Solid-state sintering occurs at temperatures below the partial melting temperature of the compact, yet high enough to generate mass transport along concentration gradients and interfaces. A simplified model of diffusion of two spheres is shown in Figure 3. Three different pathways for mass transport are shown, the first being shown as the movement of atoms across the interface of the two particles. The second is showing movement of material from the interface outwards towards the high angle interface. The third mode of diffusion shows surface diffusion, where atoms will move along the surface of the particle, also towards the high angle interface. The second and third modes are responsible for the rounding of pores through the sintering process which act to elevate the stresses caused by the initial pressure that forced the particles in contact [2]. The movement of material in this matter produces a phenomenon called densification, where the bulk part experienced an increase in density through the sintering process.

German states the mechanism of this phenomenon as the reduction of surface energy, instead of specific mass transport mechanisms such as concentration gradients. In interrupted sintering studies it is easily seen that growth between particles is accomplished to reduce high angle solid-vapor boundaries by replacing it with grain boundary area (solid-solid lower energy boundary) [12]. Once the solid-vapor interface has been significantly reduced, grain coalescence and growth continues to reduce the incoherent grain boundary interface.

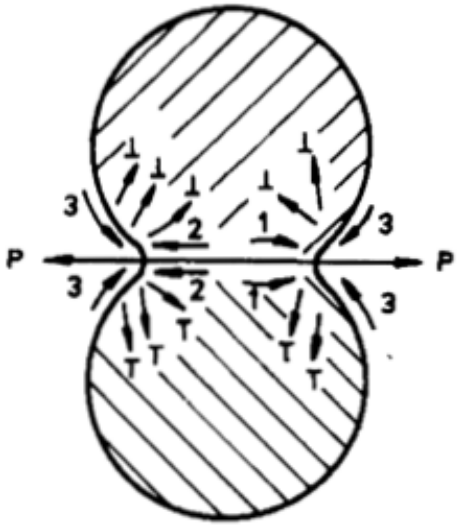

Figure 3: Diffusion routes for atoms. 1) Internal mass movement 2) Grain boundary diffusion 3) Surface diffusion [2]

1.6. Heat Treatment

With wrought steels an ingot of casted material is almost always subjected to numerous thermo-mechanical process steps that produce a homogenous microstructure. This is not the case for PM steel due to the nature of near net manufacturing where mechanical changes via physical deformation are very limited. Therefore to produce a significantly hard microstructure through austenitization and quench, dimensional stability must be kept. For this reason a gas media is used, specifically turbulent flow of cooled helium is a common practice. The use of helium is becoming problematic as its price is rapidly increasing, as can be seen in Figure 4 showing the increase in the price of helium per ton since 1938 [13].

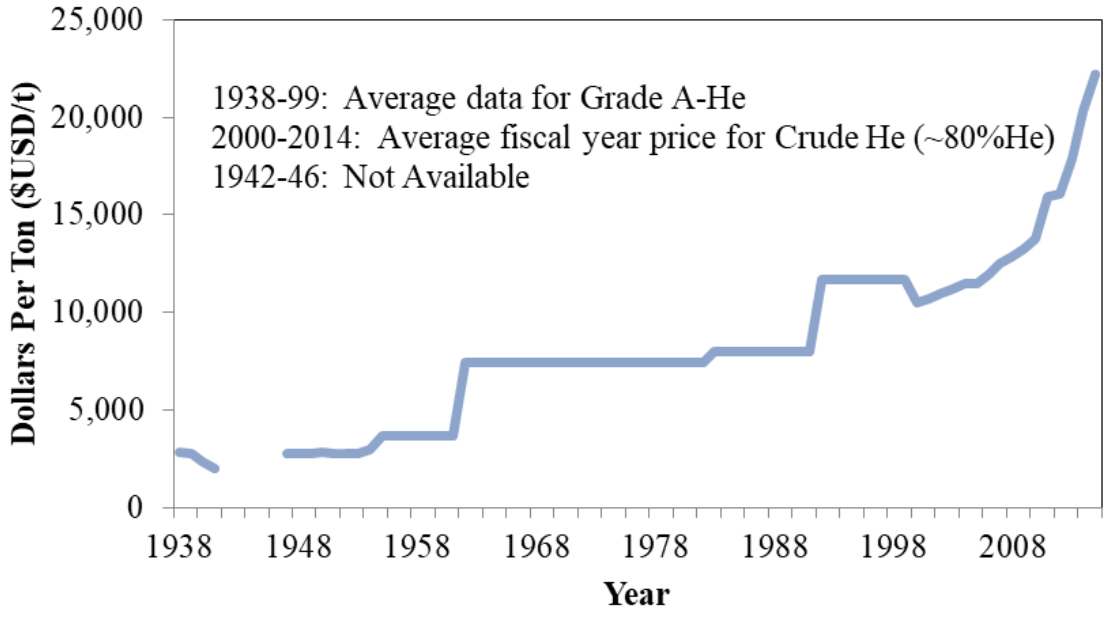

Figure 4: Helium cost per ton produces and sold in the U.S. [13]

As the trend continues it will be less and less profitable to use helium as a quenching media. In looking at other media for quenching there are pure and mixtures available, yet non with the thermal diffusivity offered by helium as shown in Figure 5 [14].

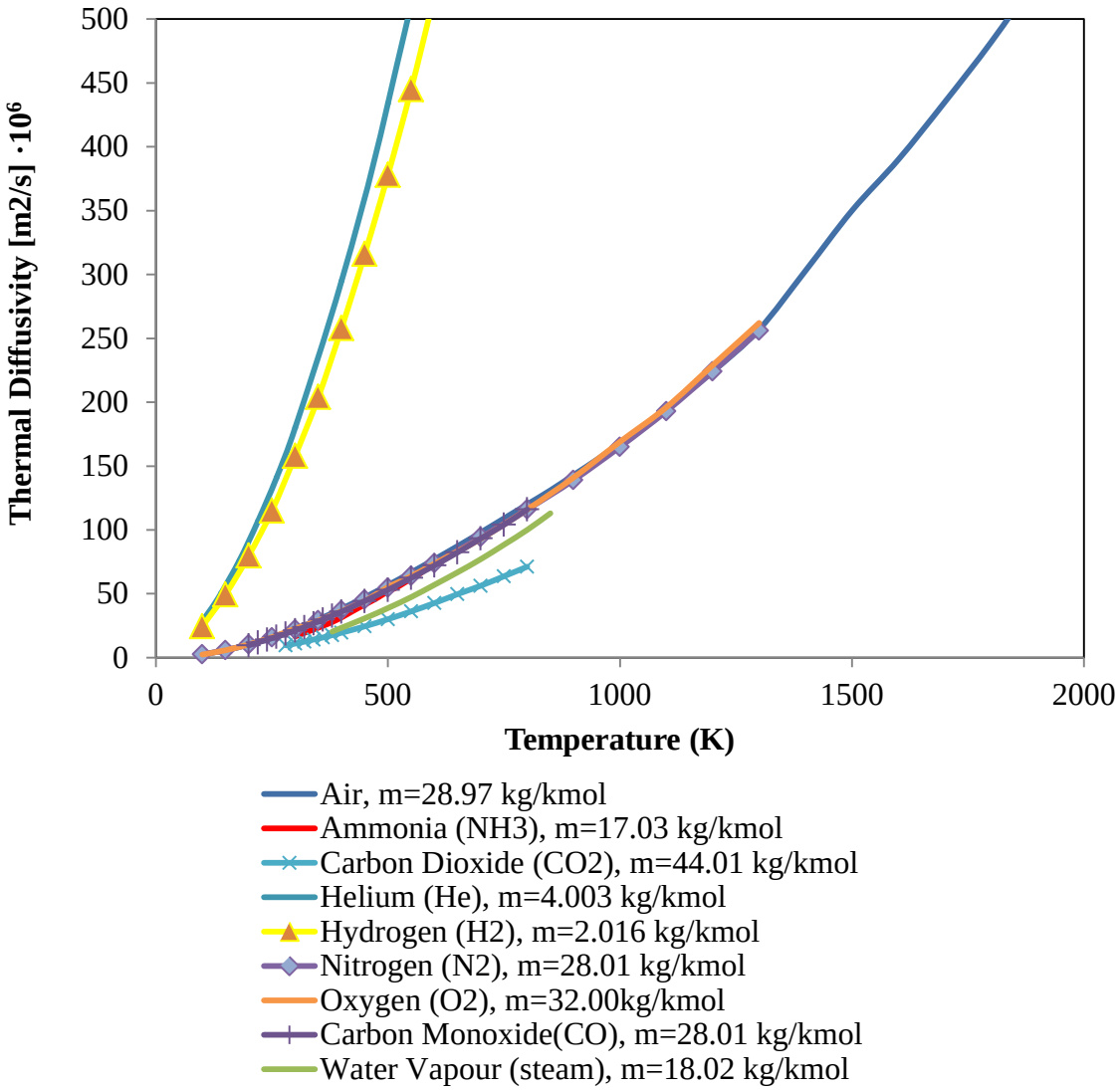

Figure 5: Thermal diffusivity of gases [14]

As Grossman pointed out, the formation of martensite is a function of the steel and quenching media. If a cheaper gas quenchant is going to be substituted with a lower thermal diffusivity, the steel must become have a higher hardenability to form the same fraction of martensite. Therefore any slight movement in increasing the hardenability of PM steel will mean a great deal to the potential profits of industry.

1.7. Research Objectives

The primary objective of this thesis is to investigate the factors that affect hardenability of PM steels. This will be done in such a way to produce recommendations, viable to industry, in producing PM parts that can produce martensite to greater depths. This has the ability to improve profits if a cheaper quenching media can be used. It can also lead to new PM designs where larger parts can be manufactured with improved mechanical proeprties. This task will be completed in the following ways:

- express the foundational knowledge of hardenability in wrought and PM steels by a literature review on hardenability of wrought and PM steels. Including historical literature, as well as up-to-date literature on the topics expressed.
- to gather quantitative and qualitative data on the effect of
    - powder sizes on hardenability
    - porosity on hardenability
- investigate the tensile and fracture properties of PM steel with a controlled microstructure.
- discuss the results in an informed manner, while concluding on industrial relevance.

1.8. Thesis Organization and Scope

Powder metallurgy (PM) is a mature manufacturing technique, which is widely used for making intricately shaped objects whose finishing into final parts requires little or no machining. Although the word "metallurgy" suggests that this technique is employed for producing metallic pieces, sintering, which is a principal and inevitable link in the PM technological chain, is utilized for producing ceramics and composites as well. Despite this passing remark, the thesis is focused on particular aspects of manufacturing and characterization of PM steels (PMS[1]). What are these specific features and how were they

[1] Depending on the context, PMS may mean either PM steel (single) or PM steels (plural); hopefully, this convention will not cause confusion.

selected? Let us attempt to answer these questions by contrasting PMS with wrought steels (WS).

Microstructure and, therefore, properties of WS are determined by an overall composition and thermo-mechanical processing. WS are typically uniform in the sense that chemical compositions of randomly chosen not-too-small volumes will be very similar; if a concentration of an alloying addition is changed, then an alteration evenly affects the whole body. Another characteristic of WS is that they are normally free of pores. Finally, WS are polycrystalline entities, in which sizes of individual grains are not dramatically different. These three circumstances along with the fact that the thermal conductivity of WS is a weak function of composition allow one to reliably predict hardenability for various steel grades.

In the case of PMS, such a reliability partially evaporates due to the following reasons.

1. Time allocated to sintering of a blended and compacted powders containing iron, graphite and metallic alloying addition is typically sufficient for densification, during which solid/gas interfaces are replaced with a lesser number of more energetically favourable solid/solid interfaces, and for a uniform distribution of carbon *via* fast interstitial diffusion. However, sintering time may not be long enough for metallic elements to relax to homogeneity. Consequently, compositional modulations result in spatially nonuniform hardenability.
2. This problem becomes especially acute if a mixture contains large Fe particles with characteristic sizes exceeding 150 μm. Even if sintering time is prolonged, their interiors will likely remain underalloyed, which means that quenching of an austenitized steel will result in soft pearlitic islands associated with these huge particles surrounded by a hard martensitic matrix.
3. Iron powders used in PM usually have a wide size distribution with heavy tails. Coexistence of small and large particles does not allow one to rely upon the average grain size as one of the factors governing hardenability.

4. Unless hot isostatic compacting is not utilized, PMS are inevitably porous. A degree of porosity can be appreciated if it is recalled that while the density of pure iron is 7.8 g/cm^3, densities of traditionally fabricated PMS varies from 6.9 to 7.2 g/cm^3. The presence of pores affects the thermal conductivity and diffusivity. Consequently, a rate of heat extraction from PMS may differ quite significantly from that for WS. In other words, porosity affects hardenability.
5. Decarburization is a detrimental side effect, which may accompany heat-treatment of steels. The usage of inert or protective atmospheres during sintering and austenitization is aimed at preventing oxidation, but it does not necessarily provide protection against carbon losses. If decarburization of dense WS happens, then only a near-surface region is affected. A porous nature of PMS suggests that an extent of decarburization may be much greater. If the density is decreased to or below 7.0 g/cm^3, then an arrangement of pores becomes more and more interconnected. As a result, in the whole body of PMS, the carbon concentration noticeably decreases in the vicinities of pores. Consequently, these near-pore regions will exhibit an inferior hardenability.

This list leaves no doubts that PMS are more complicated (or at least more multifaceted) objects than WS. In particular, due to compositional and microstructural modulations reflected in spatially varying hardenabilities, their response to quenching is not easy to comprehend and difficult to predict. Eventually, a robust physically feasible model will be developed, but an unavoidable starting point of a pass leading in this direction is acquisition of experimental data and their rationalization.

Consequently, there were no long deliberations in deciding what particular aspects of manufacturing and characterization of PMS would be worth of intellectual and experimental efforts. It was apparent that the research should be focused on the following three themes, which, surprisingly, have not been paid as much attention in literature as their scientific importance and industrial relevance deserve.

An influence of a degree of porosity on hardenability

It was intended to examine mechanical properties of Fe–C–Mn–Ni–Mo and Fe–C–Mn–Ni–Mo–Cu PMS with different and carefully controlled densities (*i.e.*, with a varying fraction of pores). A characterization of properties should include constructing of Jominy curves supported by optical microscopy observations.

An effect of size distribution of Fe powder on hardenability

It was intended to quantify the effect exerted on hardenability by a size distribution of Fe powder through making and testing Fe–C–Cr–Mn–Mo PMS, in which either only small particles or large particles or specially tailored combination of both would be utilized. It was realized that in order to get meaningful and interpretable results, samples with virtually identical densities would have to be fabricated. It was firmly believed that Jominy test would be imperative.

An impact of compositional modulations on hardenability

It was intended to observe an actual effect, which a presence of huge Fe particles in the original mixture might have on hardness and toughness of Fe–C–Cr–Mn–Mo–Ni PMS, in which a fraction of such large particles would change incrementally in a controllable manner. It was planned to see whether soft pearlitic islands were as adverse as had been suggested in literature.

Although a selection of these particular research areas may seem eclectic, they do have a common denominator: the hardenability of PMS, which is of a paramount importance in designing of news steel grades and enhancing existing ones.

In all three cases, meaningful results were obtained, and this success predetermined thesis' structure. After an overview of PM practices and an introduction of concepts related to hardenability, the reader will find three chapters devoted to individual cases. Although every chapter is conceptually linked to other two, it was deliberately attempted

to make each chapter self-sufficient and quasi-independent in the sense that it can be perused alone, that it contains all relevant information as well as conclusions and practical recommendations. Such a format will likely be welcomed by our collaborators at Stackpole, who focus on diverse R&D problems. It should be mentioned that each chapter is equipped with its own list of references for the reader's benefit; therefor there will be duplicates of some bibliographic references when similar concepts are described.

1.9. References

[1] Katerina Skotnicova, Miroslaav Kursa, and Ivo Szurman, *Powder Metallurgy*, (University Textbook). VSB-Technical University of Ostrava: Faculty of Metallurgy and Materials Engineering, 2014.

[2] Andre Salak, *Ferrous Powder Metallurgy*. 7 Meadow Walk, Great Abington, Cambridge CB1 6AZ, England: Cambridge International Science Publishing, 1995.

[3] A. Salak, M. Selecka, and H. Danninger, *Machinability of Powder Metallurgy Ssteels.pdf*. 7 Meadow Walk, Great Abington, Cambridge CB1 6AZ, UK: Cambridge International Science Publishing, 2005.

[4] ASTM International, "Standard Test Method for Apparent Density of Free-Flowing Metal Powders Using the Hall Flowmeter Funnel." ASTM International, , 100 Barr Harbor Drive, PO Box C700, West Conshohocken, PA, 2017.

[5] H. J. H. Brouwers, "Particle-size distribution and packing fraction of geometric random packings," *Phys. Rev. E*, vol. 74, no. 031309, pp. 1–14, Sep. 2006.

[6] Brian W. James, "What Is Sinter-Hardening?" Hoeganaes Corporation Cinnaminson, NJ 08077, Jun-1998.

[7] North American Hoganas, “Powder Production,” presented at the PM School, Johnstown, Pennsylvania, September 13-15.

[8] Nikolaos Vlachos and Isaac T.H. Chang, “Optimization of Metal Powder-Mixing Parameters for Chemical Homogeneityand Agglomeration,” *Int. J. Powder Metall.*, vol. 45, no. 1, pp. 19–28, 2009.

[9] P. Jones and R. Shivanath, “Powder metal alloy process,” CA2104605 C, 02-May-2000.

[10] ASTM International, “Standard Terminology of Powder Metallurgy.” ASTM International, West Conshohocken, PA.

[11] Stephen L. Feldbauer, “Advances in Powder Metal Sintering Technology,” *Industrial Heating*, pp. 51–55, Dec-2006.

[12] Randall M. German, “Sintering Simplified: Surface Area, Density, and Grain Size Relations,” *Mater. Sci. Forum*, vol. 835, pp. 50–75, Jan. 2016.

[13] T.D. Kelly, D.I. Bleiwas, and N. Pacheco, “Helium Statistics U.S. Geological Survey.” U.S. Bureau of Land Management (BLM), 2014.

[14] William D. Callister, Jr., *Materials Science and Engineering An Introduction*. Department of Metallurgical Engineering The University of Utah: John Wiley & Sons, Inc., 2007.

2: A Review of Hardenability and Heat Transfer During Quenching

The phase diagram shown in Figure 6 is a portion of the iron-carbon phase diagram. This thermodynamic data represents the equilibrium crystallographic orientations at different compositions and temperatures. Most phase transformations require a finite amount of time to come to completion[2]. Furthermore, the rate at which the transformation takes place is dependent on the heat treatment and developing microstructure [1]. The equilibrium phase diagram is useful to metallurgical engineers, yet it has a limitation without the dimension of time.

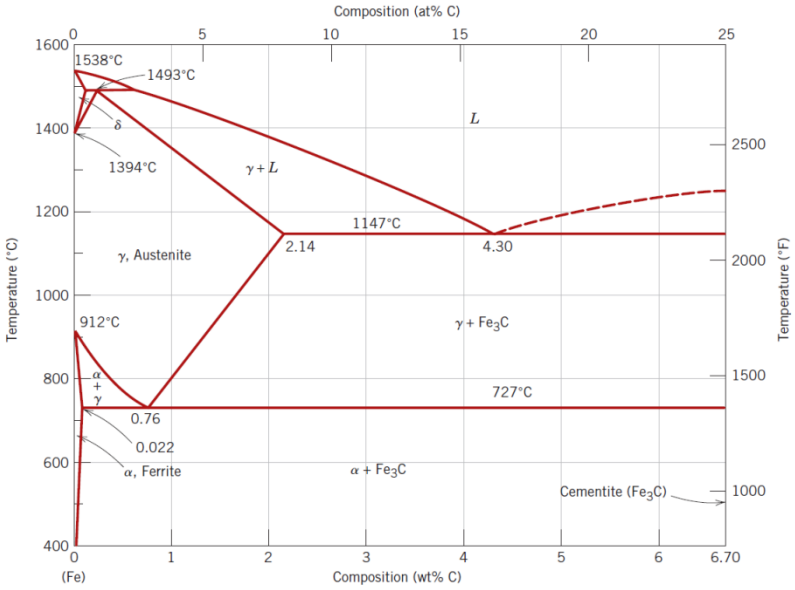

Figure 6: Iron-Caron phase diagram [1]

Davenport and Bain were the first to organize the development of isothermal transformations of austenite within a time-temperature-transformation (TTT) diagram in

[2] It is understood that true equilibrium for solid systems occurs so slowly that completely equilibrium structures are rarely achieved.

1930[2]. The original work specifies the TTT diagram shown in Figure 7 as a summary chart of the large undertaking of producing this information experimentally.

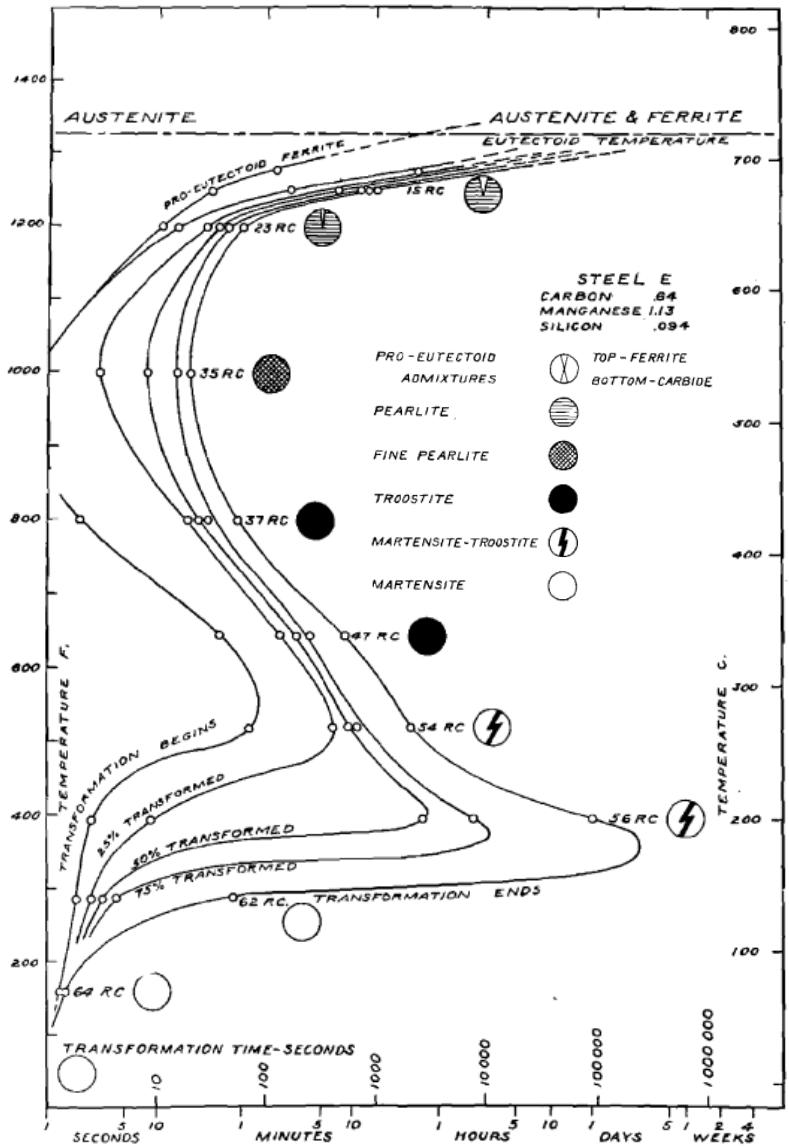

Figure 7: Summary diagram of the time-temperature-transformation information gathered for steel by experimentally holding steel at intercritical temperatures for specific times and observing the microstructure [2]

The TTT diagram expresses the volume fraction of transformed phase from austenite as a function of temperature and logarithmic time for the given composition of steel. Since 1930 TTT curves have been used in describing the isothermal phase transformations for

many steel alloys. This can be seen in Figure 8 comparing 1060 (a) and 5160 steel (b). The Ae_3 line corresponds to stable austenite, and the M_S is the starting temperature for the transformation of martensite, M_{50} and M_{90} are the 50% and 90% transformation lines. "A", "F" and "C" relate to the austenite, ferrite and cementite phases respectively.

(a) *(b)*

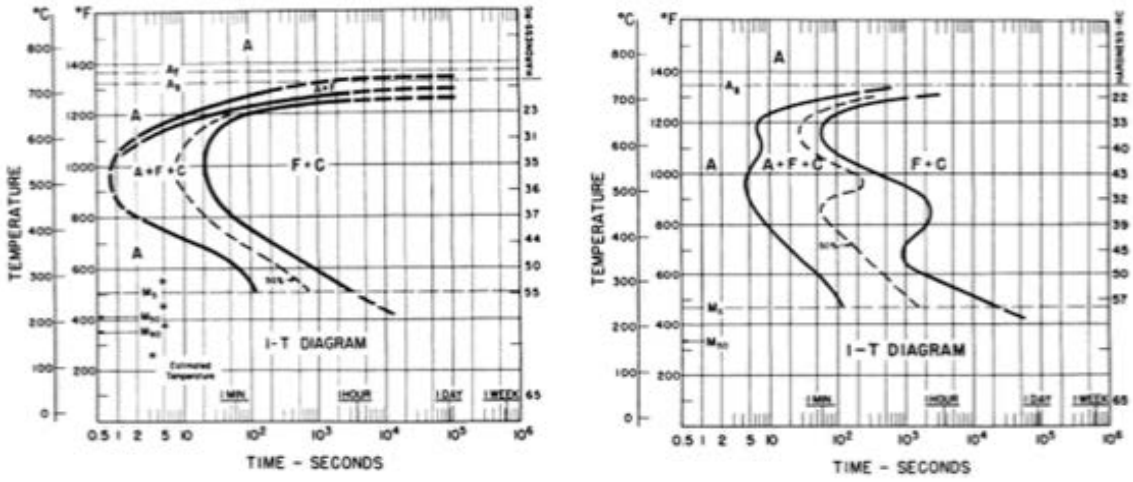

Figure 8: TTT Diagram for a) 1060 steel: 0.64wt%C, 1.13wt%Mn austenitized at 910ºC - ASTM austenite grain size of 7 b) 5160 Steel: 0.62wt%C, 0.94wt%Mn, 0.88wt%Cr austenitized at 843ºC – ASTM austenite grain size of 7 [3]

The graphs shown in Figure 7 and Figure 8 are representations of isothermal times, yet it is understandable that the reality of cooling a large piece of steel is continuous. It is therefore useful to augment these graphs with continuous cooling curves, producing continuous-cooling transformation (CCT) diagrams, as further exemplified in Figure 9.

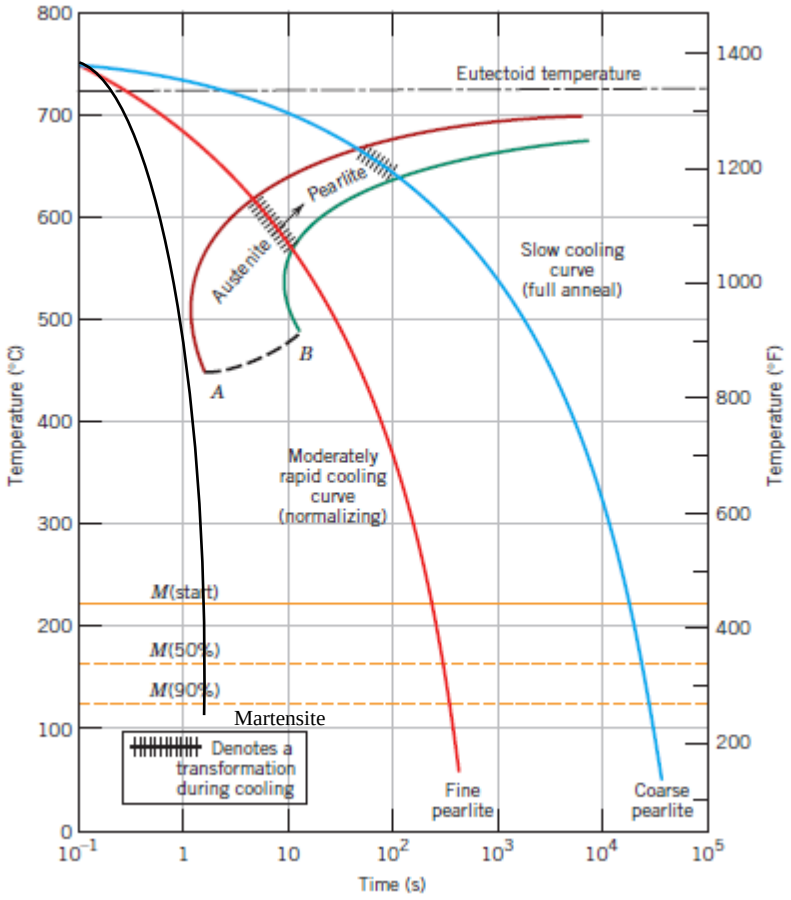

Figure 9: Continuous cooling transformation (CCT) diagram showing rapid to slow cooling curves for a eutectoid iron-carbon steel [1]

The blue and red cooling curves represent the cooling path of eutectic steel from austenite to coarse and fine pearlite. The blue curve represents a slower cooling where more time is spent within the austenite to pearlite transformation region. A longer time within this temperature range increases carbon diffusion allowing for more coarse grains. The black curve represents a very rapid cooling curve from austenite to martensite. Martensite is a nonequilibrium BCT crystallographic structure which can be formed if FCC austenite is cooled rapidly enough to prevent carbon diffusion. It can therefore be imagined that if the "C" shaped transformation region was somehow retarded, and shifted to the right; longer times could be used to form martensite. This is beneficial for very large steel parts

where even if heat was removed as fast as possible from the surface, it would still take time for heat to move from the center-out.

The “ease” of a material to form martensite, or the ability for martensite to form at longer cooling times, is defined as its hardenability. It can then be observed referring back to Figure 8 that (b) represents a more hardenable material. The differences in shape and position of the curves in comparing (a) and (b) represent how the addition of Cr can stabilize austenite at lower temperatures, allowing for more time to cool to the martensite start temperatures without a diffusional phase nucleating.

2.1. Ideal and Critical Diameter

The quantification of the hardenability of steel was found experimentally by Grossmann. This was done by austenitizing and then quenching steel cylinders with ranging diameters. The critical diameter of the steel was found when the largest cylinder formed 50% martensite in the center after quenching [4]. Using the experimental analysis it was possible to formulate a relation to the features of the steel to the depth of hardening. This is commonly used in industry, referring to the ideal diameter (DI). This assumes the quench is ideal, which refers to the heat transfer on the outside of the bar is infinitely fast. In reality this is not the case, and will be further explained at the end of this chapter. The ideal diameter is a function of the alloying constituents of the steel, austenitic grain size before quenching. This can be seen in equation(2), where the multiplying factors due to the alloying concentrations, y-axis in Figure 10 expressed as f_x, and ASTM grain size values, y-axis in Figure 11 expressed as DI_{base}.

(2) $$DI = DI_{base} \cdot f_{\mathrm{Mn}} \cdot f_{\mathrm{Si}} \cdot f_{\mathrm{Cr}} \cdot f_{\mathrm{Mo}} \cdot f_{\mathrm{Cu}} \ldots$$

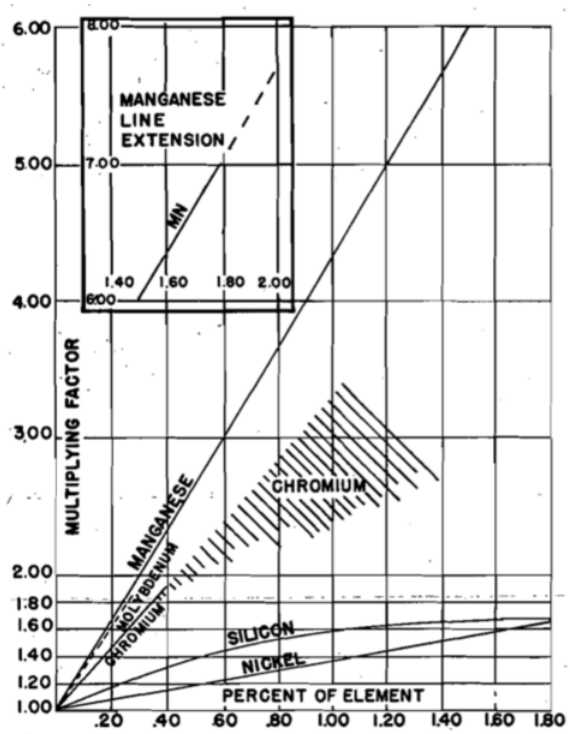

Figure 10: Alloying element's and their concentration's effect on the multiplying factor used in Grossmann's equation for ideal diameter[5]

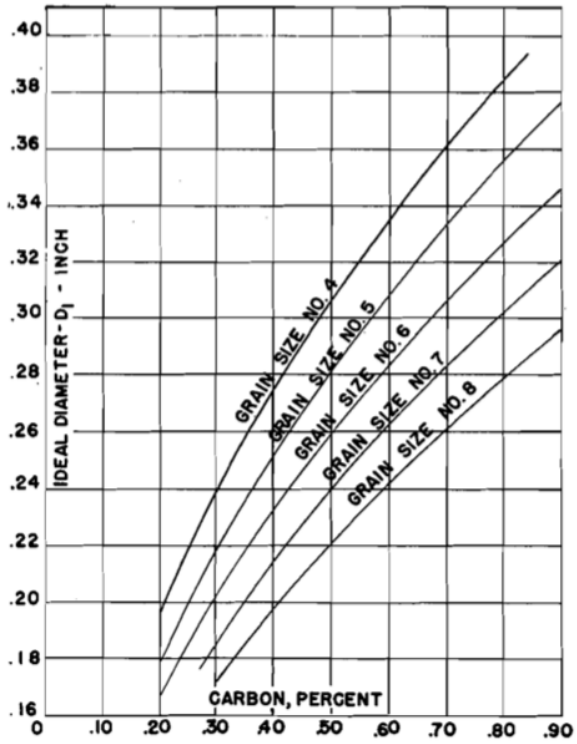

Figure 11: Ideal diameter as a function of carbon content and ASTM grain size where an increase in austenitic grain size, decrease ASTM grain size, increasing the DI[5]

When the quench is not assumed to be ideal, Grossmann also produced a common expression for the severity of quench, *H*, with the units of m^{-1}. It defines the ability for a quench to extract the heat of the steel from the surface with a ratio of the heat transfer coefficient of the surrounding media, *h*, in W/m^2K and the thermal conductivity of the steel, λ, W/mk as seen in (3).

$$H = \frac{h}{\lambda} \tag{3}$$

It is important to note that Grossmann refers to the diameter of steel and not the radii, and therefore many researchers have added a 2 in the denominator when referring to the radius [6]. The H value for unagitated water at 18ºC is 0.9-1.0m^{-1}[5]. The ideal critical diameter is used along with the severity of quench to determine the depth of hardening, or the critical diameter, in terms of the specific quenchant. For example Figure 12 shows a

graph of H values with respect to the calculated ideal diameter and the critical diameter that would be found given a realistic quench of specific steel. For example calculated ideal diameter of 2.4 inches would actually be 1.55 inches if unagitated water were used. This is found by finding the ideal diameter on the x-axis, and moving vertically until the 1.0 contour line is intersected, reading the y-axis for this point is the critical diameter.

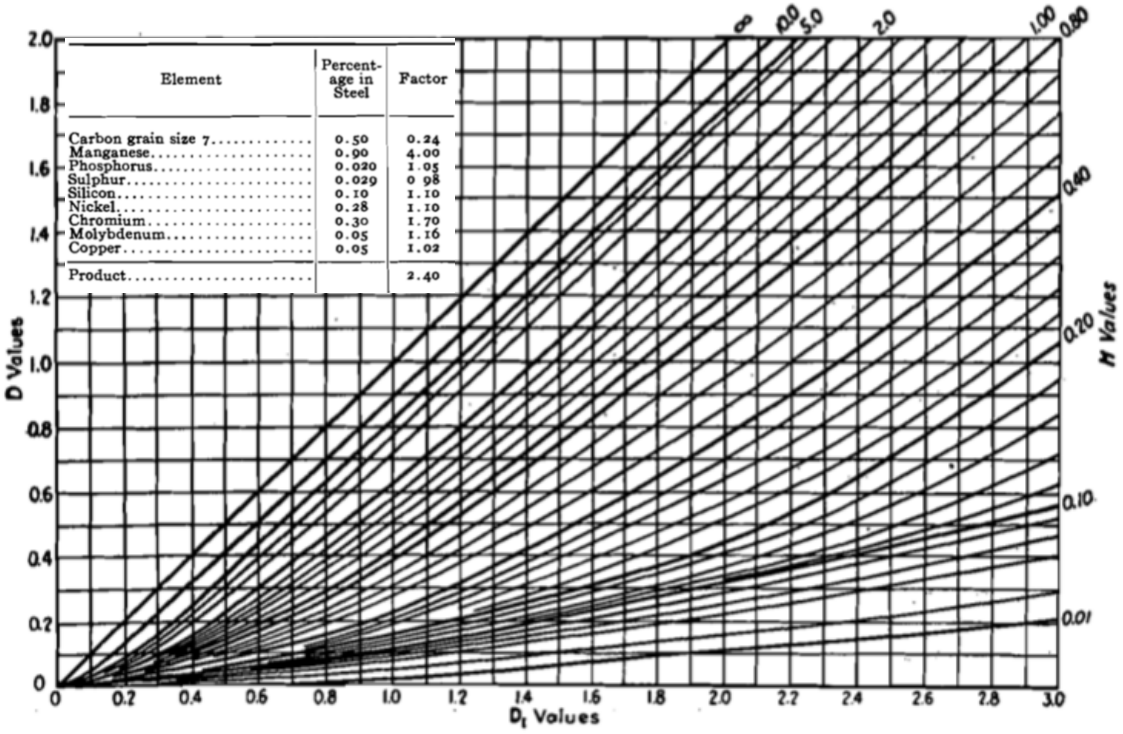

Figure 12: Graph produced by Grossmann to estimate the critical diameter for the specific steel composition shown linking the ideal critical value (x-axis) to the severity of quench (H values as contour lines) with the critical diameter (y-axis)[5]

2.2. Heat Transfer

Grossmann's severity of quench is a measurement of thermal resistance, a value of H less than 1 describes the solid being more thermally conductive than the quenching media. This is not the entire picture of the complex modes of heat transfer during quenching.

There are three modes that heat is transferred by: conduction, convection and radiation. Conduction is the transfer of thermal energy from more energetic particles to less

energetic *via* physical interaction between particles. This translation of energy occurs in gas, liquid and solid states of matter. Convection encompasses two mechanisms, energy transfer via random particle motion and interaction, as well as macroscopic motion of fluid. This bulk movement is explained by a large number of molecules moving together in the presence of a temperature gradient. Thermal radiation is transferred by electromagnetic waves and therefore does not require a material medium to transfer through.

As heat travels through a solid media in conduction it can be explained as the heat flux, q, [W/m^2] which is the heat transfer rate per area perpendicular to the heat flow. q, is related to the thermal conductivity, k, of the material and the temperature gradient by Fourier's law as seen in (4).

(4) $$q = -k\frac{dT}{dx}$$

Similarly, a relation of the heat transfer coefficient, h, and the difference between the surface and fluid temperature describes convection heat flux.

(5) $$q = h(T_s - T_\infty)$$

The heat transfer coefficient depends on the boundary between the quenching media and the steel. It can therefore be greatly affected by the geometry of the part, motion and thermodynamic properties of the fluid [8].

During quenching into a liquidized media there are four steps, shown in Figure 13. Step one is the production of a film layor, where the vaporization of the liquid occurs on the surface of the part producing a thin gas film. Since the mode of heat transfer is primarily radiation, the transfer is slow. The following step occurs when the vapour film begins to collapse and the interface alternates between solid-gas, and solid-liquid. Between this step, and step 3 the temperature of the steel will decrease and the heat flux will increase as the convection mode of heat transfer takes over, this is where the maximum critical heat flux occurs. It should also be noted that since the interface is alternating between

liquid and gas the removal of heat will not be the same everywhere. As is seen in Figure 13, step three shows bubbles nucleating on the surface of the part as the liquid is in direct contact with steel. The liquid is being superheated, and will nucleate on surface blemishes of the steel. The transfer of heat is still high in this region as there is direct contact with the liquid, transferring the latent heat of vaporization to the liquid. Once the steel has cooled to below the vaporization temperature, step 4 will occur where convection will continue until the temperature of the steel equalizes to the liquid [9].

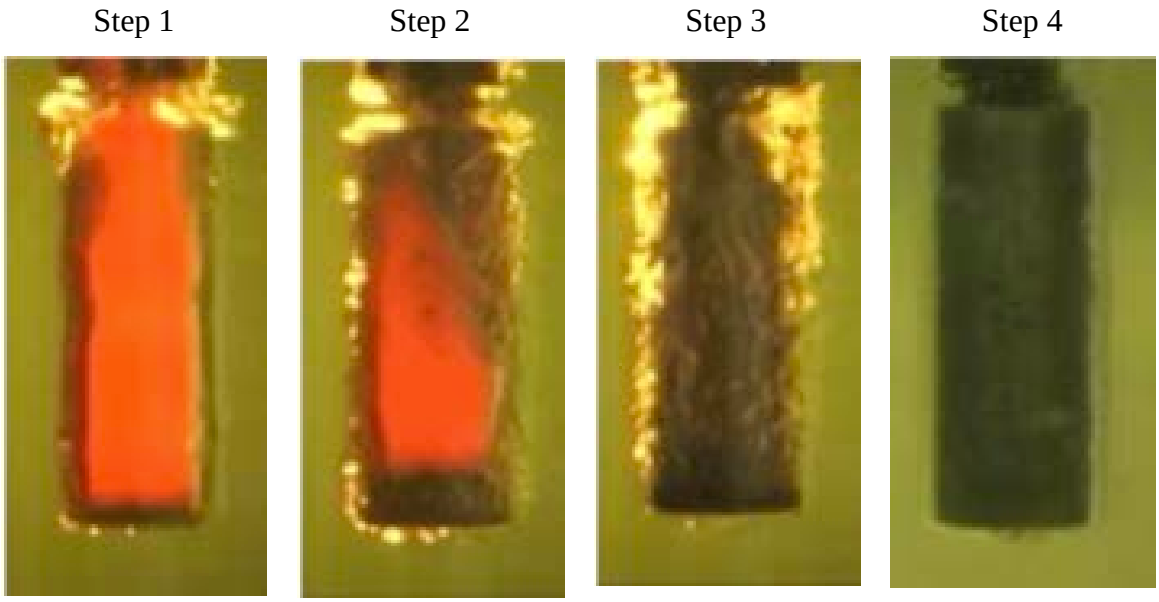

Figure 13: Steps of quenching a relatively hot steel part in a liquid quenching media

As expressed above, a liquid quench will unevenly remove heat during the quench. This creates internal stress within the part, which could lead to warping or bending. For this reason a gas quenchant is commonly used in the PM industry. There are many works on defining heat transfer coefficients of different gases encompassing different situations which are within the reference section for the reader to explore[10]–[12].

The mechanisms of heat transfer have been shown to be complex, yet the simple relation specified by Grossmann is commonly used in industry. It works extremely well with wrought steel, where the thermal conductivity, k, does not change much by the addition or subtraction of different alloying elements. It is also well used in the production and

designing of PMS, yet there is a potential flaw to this. As is known PMS could have an array of pores as the density decreases from 7.87g/cm^3. It is also known, and will further be expressed in this thesis, that as PMS density decreases so does its thermal conductivity. Grossman's relation then begins to give falsehoods, as "k" decreases at a constant h the severity of quench will increase. This represents an ability to form martensite to greater depths. There is an obvious problem, yet not an easy or even singular solution, of defining the hardenability of PMS. It is therefore the hope that the following chapters will add to the pursuit of a solution to this problem.

2.3. References

[1] William D. Callister, Jr., *Materials Science and Engineering An Introduction*. Department of Metallurgical Engineering The University of Utah: John Wiley & Sons, Inc., 2007.

[2] E. . Davenport, E. . Bain, and N. . Kearny, "Transformation of Austenite at Constant Subcritical Temperatures." United States Steel Corp, 1930.

[3] George F. Vander Voort, *Atlas of Time-temperature Diagrams for Irons and Steels*. ASM International, 1991.

[4] M.A. Grossmann, *Elements of Hardenability*. Cleveland Ohio: American Society of Metals, 1952.

[5] M. A. Grossmann, "Hardenability Calculated from Chemical Composition," *Am. Inst. Min. Metall. Eng.*, vol. 299, no. Technical Publication No. 1437, Feb. 194AD.

[6] Rosa Lucia Simencio Otero, Walker Roberto Otero, George Edward Totten, and Lauralice C.F. Canale, "Quench Factor Characterization of Steel Hardening: A Review," *Int. J. Mech. Eng. Autom.*, vol. 1, no. 3, pp. 119–128, 2014.

[7] ASTM International, "Standard Test Methods for Determining Hardenability of Steel." ASTM International, West Conshohocken, PA.

[8] Theodore L. Bergman, Adrienne S. Lavine, Frank P. Incropera, and David P. Dewitt, *Introduction to Heat Transfer*, 6th ed. John Wiley & Sons, Inc., 2011.

[9] Virendra S. Warke, “Predicting the Response of Powder Metallurgy Steel Components to Heat Treatment,” Doctor of Philosophy in Materials Science and Engineering, Worcester Polytechnic Institute, 2008.

[10] Heming Cheng, Jianbin Xie, and Jianyun Li, “Determination of surface heat-transfer coefficients of steel cylinder with phase transformation during gas quenching with high pressures,” *Elsevier Comput. Mater. Sci.*, vol. 29, pp. 453–458, 2004.

[11] Bowang Xiao, “Influencing Factors of Heat Transfer Coefficient in Air and Gas Quenching.”

[12] Yuan Lu, Yiming Rong1, Richard D. Sisson Jr, “Equivalency Comparison of Heat Transfer Coefficient in Liquid and Gas Quenches,” *TMS Miner. Met. Mater. Soc. 2015*, 2015.

3: An Experimental Study on The Influence of Porosity on Hardenability

3.1. Abstract

The ability to predict the hardenability of steel is a key tool used in designing high performance alloys. Classically this is easily computed within reasonable error using a projected ideal diameter. Bulk PM and wrought steel can be chemically identical, yet differ in properties due to porosity, and chemical variation. Using a proven method for wrought steels to predict the final properties of a designed PM alloy is therefore inappropriate. In an effort to reclaim Grossmann's predictions of hardenability for PM steel, a direct experimental investigation linking the density to hardenability was launched on prealloyed FL-4605 and FL-4605+2%Cu. As PM density decreases, sites for heterogeneous nucleation increase, and thermal conductivity decreases, stunting the formation of martensite. This deviation must be incorporated in the computation of the severity of quench, and projected ideal diameter to grant more accurate results.

3.2. Introduction

The final porosity is directly related to the process conditions for a PM steel part. For example decreasing the initial size of the powder and/or increasing sintering temperature will round pore morphology, decrease the size of the average pore, and allow for a larger magnitude of densification, decreasing pore volume fraction. Furthermore increasing compaction pressure will result in a higher density part [1], [2]. It is not new knowledge that porosity is a hindrance on the mechanical properties of PM steel[3]–[5] . The added porosity will decrease the cross sectional area of a loaded specimen, along with introduce

crack initiation and further propagation sites. The physical geometry is not the only issue in hindering the mechanical properties, but also the ability for strong phases such as martensite to form.

3.3. Porosities effect on Phases in PM Steel

In comparing a heat treatment of wrought steels to PM, pores increase free surfaces that are favorable to ferrite nucleation during cooling from austenite. This was seen in a study where PM steel at different densities was subject to intercritical temperatures to form ferrite before quenching. It was discovered that an increase in pores, increased the nucleation rate of ferrite, yet the growth rate of ferrite was hindered or pined [6]. A similar outcome was found in the formation of bainite where the nucleation rate increased, yet the growth rate did not show a change. This was explained to be due to the lower activation energy of carbon diffusion in more porous austenite by means of more diffusion pathways [7].

When quenching PM steel in liquids, it was found that an increase in porosity increases the rate of heat transfer out of the steel *via* breaking the surface film and bubble nucleation sites at surface pores. As explained above, past the “nucleate boiling” heat transfer regime during liquid quenching bubbles form on the surface at nucleation sites *i.e.*, surface defects. These bubbles transfer the latent heat of vaporization, and continue to produce convection currents at the surface. Warke et al. states that PM parts will react differently to this heat transfer regime than wrought steels; the surface pores will break surface films produced in stage 1, and increase the amount of heat extraction through more nucleation sites for regime 3[8].Warke et al. did a comprehensive study on phase transformation in PM steels using dilatometry, and found that an increase in pores will increase the martensite start temperature [9]. This work was also able to produce a TTT diagram for transformation of austenite to bainite, and austenite to martensite at different densities for FL-4605 PM steel seen in Figure 14[9].

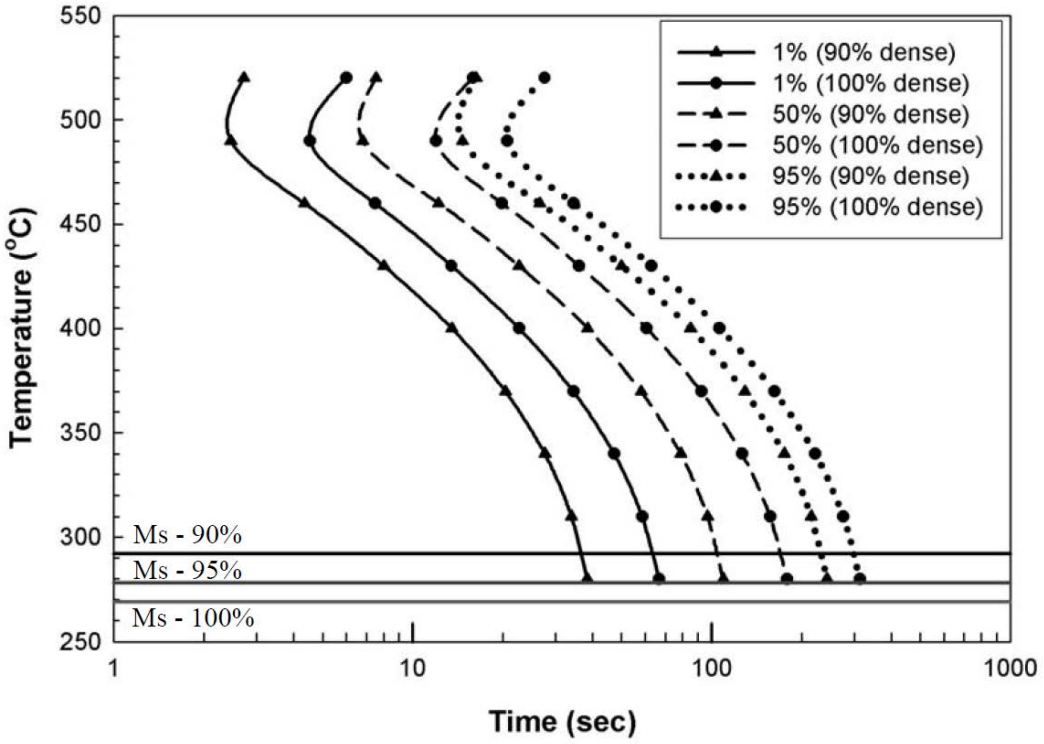

Figure 14: TTT diagram for 90% and 100% dense FL-4605[9].

In a study on dual phase PM steels, Mahesha et al. suggested that as the volume fraction of porosity increases the only grain boundaries available for austenite nucleation would be available at the pores, therefore decreasing their availability for nucleation; this relates to a lower nucleation rate and higher growth rate. This inevitably leads to larger heterogeneous grains of martensite. In the opposite case, as porosity decreases there will be an increase in available grain boundaries for austenite to form, increasing the nucleation rate over the growth rate. Therefore the austenite grains will form tighter collections leading to finer grains [10].

3.4. Thermal Conductivity

There are multiple recourses on how porosity inside metallic materials effect the thermal conductivity [11]–[14]. It has been suggested that a linear relationship between porosity and thermal conductivity exists by experiments involving PM bronze. This can be seen in (6) where the pores are represented by cylinders, the porous material thermal conductivity

"λ" to the homogenous material "λ_0" is related to the void fraction of the material ε[11].

(6) $$\frac{\lambda}{\lambda_0} = 1 - \varepsilon$$

By representing the pores as the space between mono-sized spheres (7) was found, where the maximum porosity occurs at $1 - \frac{\pi}{6}$. This was shown to fit the experimental data better than(6) up to 40% porosity when comparing to different density of bronze between 20-200C [13], [14].

(7) $$\frac{\lambda}{\lambda_0} = 1 - 2.1\varepsilon$$

Aivazov and Domashnev [14] used a statistical analysis of mixtures of inclusions, where randomly orientated and regular porous structures were considered; their work produced equation (8). This was further compared to an experimental analysis for hot isostatically pressed titanium-nitride where n (an experimentally found coefficient) was found to be 6 [14]. In [13] this model was used on 304L stainless steel and OFHC copper PM where n was found to be 11.

(8) $$\frac{\lambda}{\lambda_0} = \frac{1 - \varepsilon}{1 + n\varepsilon^2}$$

This information is summarized in Figure 15 showing the three equations as a function of porosity.

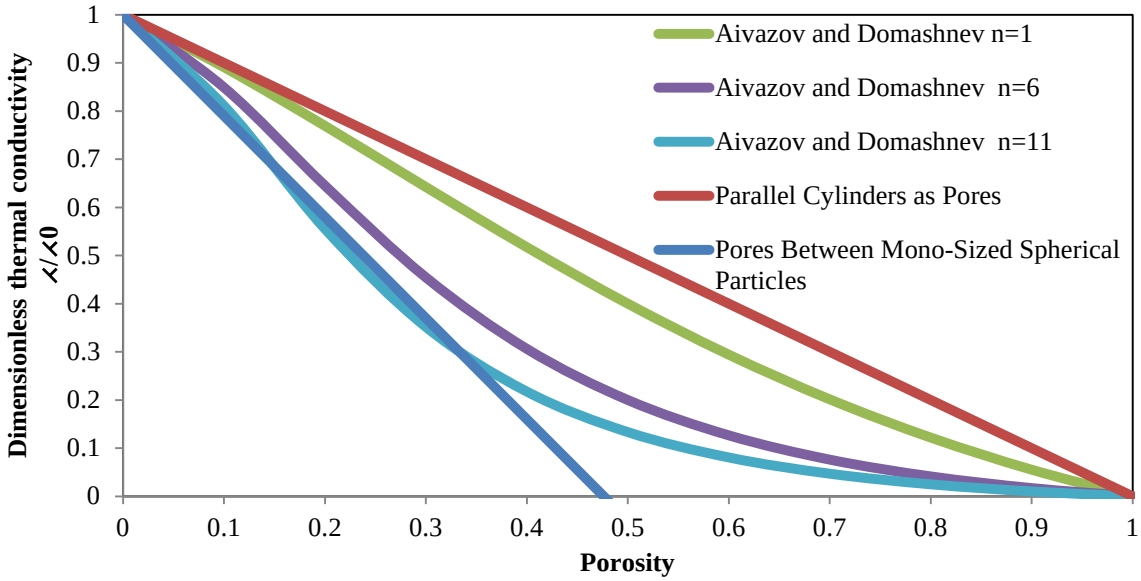

Figure 15: Comparison of thermal conductivity equations [11]–[14]

As is shown above the void fraction has been found to be inversely proportional to the thermal conductivity of the material. In [11] a three sintered steel with a range of porosity (7-16vol%) was tested via the Jominy test to investigate how the change in thermal conductivity effected the hardenability of PM Steel. Even though there is quantitative evidence that the thermal conductivity will decrease with an increase of porosity, an increase in cooling rate with porosity greater than 12vol% was found when compared to the wrought steel of the same composition.

Further experiments have been completed that have produced some controversial theories. Saritas et al. and Stiles [11], [15] found similar findings that steel hardenability increases with increasing porosity through experimentation, and Zavaliangoes and Semel through simulations as well [16]. An initial hypothesis was that water penetrated pores, increasing the heat transfer rate [11], [15]. Semel speculated that since the maximum heat decrease found in these studies was during the middle of the temperature range that the reason for this faster cooling rate could not be from external issues and therefore occurred due to the latent heat effects *via* the phase transformation of austenite to martensite. This corresponds with an increase in martensitic start temperature as observed in PM steels [9], [16].

A study was completed in using a gas phase quenchant to exclude any effect expressed above on different densities and sizes of admixed PM material. It was observed that smaller parts were more hardenable, producing a higher strength. Different phases were characterized for different densities where when placed under the same heat treatment. For example, material at 6.8g/cm^3 was primarily fine pearlite, and material at 7.0g/cm^3 consisted of upper bainite. It was further stated that this observation was due to a difference in homogeneity of alloying constituents instead of a difference in thermal diffusivity [17].

3.5. Experimental Methodology

It has been already emphasized in the preceding sections that numerous factors may affect and do affect hardenability. Since it is intended to quantify how density influences hardenability, it is important to eliminate other factors including, indeed, a possible compositional non-uniformity. In view of this, it is not surprising that instead of mixtures of Fe with alloying additions and graphite, powders of prealloyed steels were utilized. Since the outcome of the experimental investigation should be compared with data already given in the literature, it was decided to use a composition of steel closely resembling that of a widely used grade FL-4605. The composition of the steel powder is given in Table 1.

Since it is known that a presence of Cu may enhance the hardenability, a copper-containing version of FL-4605 was also used in the experiments. The chemical composition of this modified grade is also given in Table 1.

Table 1. Chemical composition of steels

	Concentration, wt.%					
Grade	C	Mn	S	Ni	Mo	Cu
$\overline{\text{Cu}}$	0.52	0.20	0.007	1.81	0.55	0.02
Cu	0.52	0.20	0.006	1.79	0.54	1.69

For each grade, a number of parallelepipeds possessing various densities were made. Those blocks were then machined into Jominy bars with sizes prescribed by the ASTM Standard A255–10[18]. In order to assist a reader in analyzing the experimental results, let us introduce a "naming scheme", which help to avoid a confusing linking an object to its properties.

For the traditional 4605 steel, the identifier $\overline{\text{Cu}}\text{-density} - \text{ID}$ is employed, where density is low, intermediate or high, and ID is just a sequential number of a specimen. For instance, $\overline{\text{Cu}}\text{-LOW} - 2$ is the 2^{nd} sample with a low density, and $\overline{\text{Cu}}\text{-INT} - 1$ is the first specimen having an intermediate density. For copper-containing entities, the identifier $\text{Cu} - \text{density} - \text{ID}$ is used; for example, $\text{Cu} - \text{HIGH} - 2$ is the 2^{nd} specimen with a high density.

Although it might be tempting to give detail of how exactly powders were compacted, such a degree of elaboration is hardly justified. It would suffice to present green body densities; these specific gravities are given in Table 2.

Table 2: Specific gravities of steels

Grade	Density, g/cm^3	Pressure, Mpa
4605	6.80	499
4605 with Cu	6.80	484

LOW samples were pressed at room temperature and sintered, where INT samples were repressed with 689Mpa of force in a dissociated ammonia gaseous atmosphere at 871°C. It must be emphasized that LOW and INT samples were sintered at 1280°C for 1 hour, but HIGH specimens were produced *via* hot pressing: after the initial compaction, they were heated to 1220°C, kept in the furnace for one hour and pressed. This procedure was repeated twice. The final sintered densities can be seen in Figure 16.

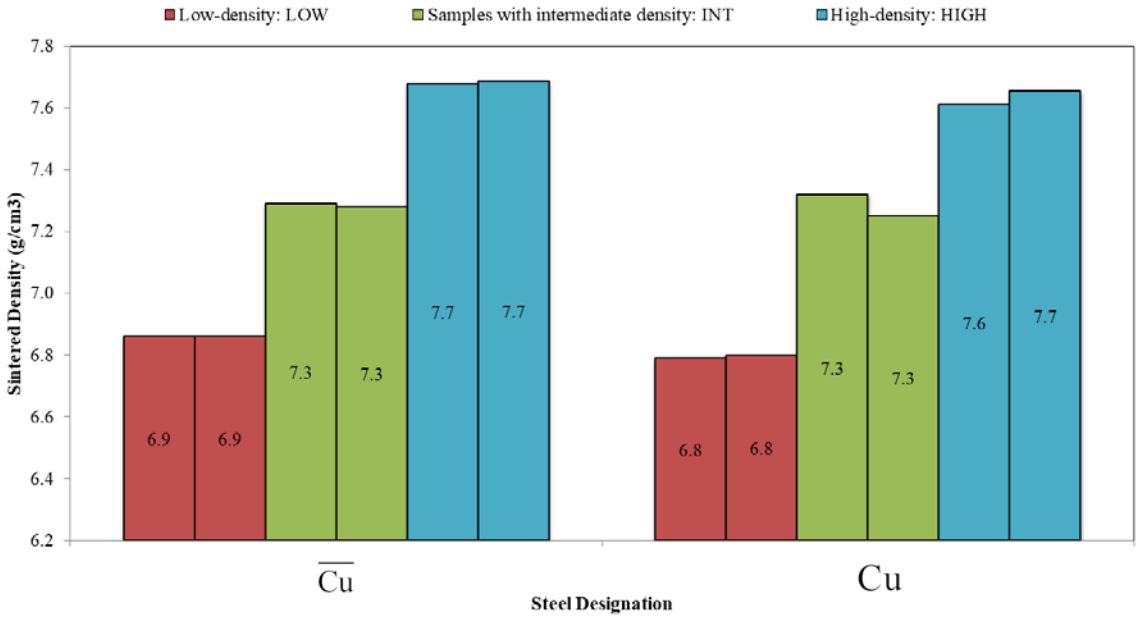

Figure 16: Sintered densities of LOW, INT and HIGH samples

3.6. Hardenability Simulations and Calculations

As stated previously, there are many methods that have been developed for the purpose of calculating the hardenability of a given steel composition, and its corresponding Jominy curve. This raises the question as to which is most accurate, and best to rely on for the purposes of this study.

3.6.1. ASTM A255 Calculated

Grossman's ideal diameter equation is used in the prediction of Jominy curves in the method outlined by ASTM-A255-10. It takes advantage of the ideal diameter calculation that uses specific coefficients referred to as multiplying factors, f_x, for each aspect that affects hardenability; grain size, and the alloying constituents. ASTM further refined the multiplying factors through extensive experimentation of 1500, 4100, 5000 and 8600 series steels [18], [19]. This refinement has placed more strict boundaries of the alloying elements used as it best describes similar steels, and therefore specific ranges are outlined. An example of a range of alloying material, and its corresponding MF

calculation can be seen in (9). A complete range of alloying elements and corresponding equations can be found in the appendix.

$$\begin{aligned} \text{Mn} \le 1.2\%,\ f_{\text{Mn}} &= 3.3333(\%\text{Mn}) + 1.00 \\ 1.2\% < \text{Mn} \le 1.95\%,\ f_{\text{Mn}} &= 5.10(\%\text{Mn}) - 1.12 \end{aligned} \tag{9}$$

These multiplying factors are then implemented in Grossman's equation for the Ideal Diameter as seen in equation (10) [18], [19].

$$DI = DI_{base} \cdot f_{\text{Mn}} \cdot f_{\text{Si}} \cdot f_{\text{Cr}} \cdot f_{\text{Mo}} \cdot f_{\text{Cu}} \cdots \tag{10}$$

In predicting the Jominy curve the ASTM standard specifies a table of dividing factors (DF) corresponding to a specific distance along the Jominy bar. The DI is used here by finding the corresponding row from this table. This DF values are used by dividing the 50% martensite hardness found via Table 7 in A255 entitled *Carbon Content, Initial Hardness, 50 % Martensite Hardness.* A sample of DF can be seen in Figure 17.

Ideal Diameter (DI), in.	Jominy End-Quench Distance (1/16 in.)																
	2	3	4	5	6	7	8	9	10	12	14	16	18	20	24	28	32
1	1.15	1.50	2.14	2.46	2.72	2.81	2.92	3.07	3.22	3.49							
1.1	1.12	1.42	1.99	2.32	2.60	2.70	2.80	2.94	3.07	3.34							
1.2	1.10	1.35	1.85	2.20	2.48	2.59	2.69	2.81	2.94	3.20	3.32	3.44					
1.3	1.08	1.29	1.74	2.09	2.38	2.48	2.58	2.69	2.81	3.07	3.19	3.30	3.53				
1.4	1.07	1.24	1.64	1.99	2.27	2.38	2.47	2.58	2.69	2.95	3.06	3.17	3.37	3.50	3.79		
1.5	1.05	1.19	1.56	1.89	2.18	2.28	2.37	2.47	2.58	2.83	2.94	3.05	3.22	3.35	3.61		
1.6	1.04	1.16	1.49	1.81	2.09	2.19	2.28	2.37	2.47	2.73	2.83	2.94	3.09	3.21	3.45	3.67	3.77

Figure 17: Example of Dividing Factors related to the Ideal Diameter from ASTM-A255 for non-Boron steels [18]

3.7. SteCal

Stecal uses expressions formulated through rigorous experimental data, similar to ASTM A255 where the ideal critical diameter is a function of grain size, carbon content and the alloying constituents. This function can be seen (11) where the Ideal critical diameter "H" is expressed as the multiplication of the coefficients of grain size C_{GS}, carbon content C_C and alloying constituents C_i.

$$H = C_{GS} \times C_C \times \prod C_i \tag{11}$$

This ideal critical diameter is used to formulate theoretical Jominy curves, where the depth of martensite formed is found *via* an experimental comparison. Rodes et al. (the developer of this method) produced a circular calculator to assist in this comparison of known information [20]. This produces the specific shape of Jominy curve produced in Stecal, where hardenabile steel will produce a Jominy curve with an initial plateau of hardness, followed by the inflection point and asymptote.

3.8. M.C.A.S.I.S

The M.C.A.S.I.S owner's manual describes the Minitech hardenability predictor as an "accurate predictor of the Jominy curve" [21]. Kirkaldy and Minitech Limited developed the methodology used in this program, where the inflection point on the Jominy curve is found semi-empirically *via* thermodynamic and kinetic calculations. The complete Jominy curve is then found from the carbon-dependent hardness and this inflection point. This method was compared with numerous measured Jominy curves for calibration and was found to be precise [21].

After careful consideration of the processes that are occurring within these programs a comparison study was launched from known literary sources to be compared to the simulated results. It was found that in steel alloys containing Nickel, M.C.A.S.I.S produced curves most resembling the experimental data. In steel alloys without Nickel the ASTM, StelCal and M.C.A.S.I.S calculations produced similar trends. This can be seen in Figure 18 and Figure 19 in comparing literary values of 4130[22] and 8740[18] steels. The manufactured steel in this project contains nickel, and therefore M.C.A.S.I.S will be used to compare the ideal case to the results.

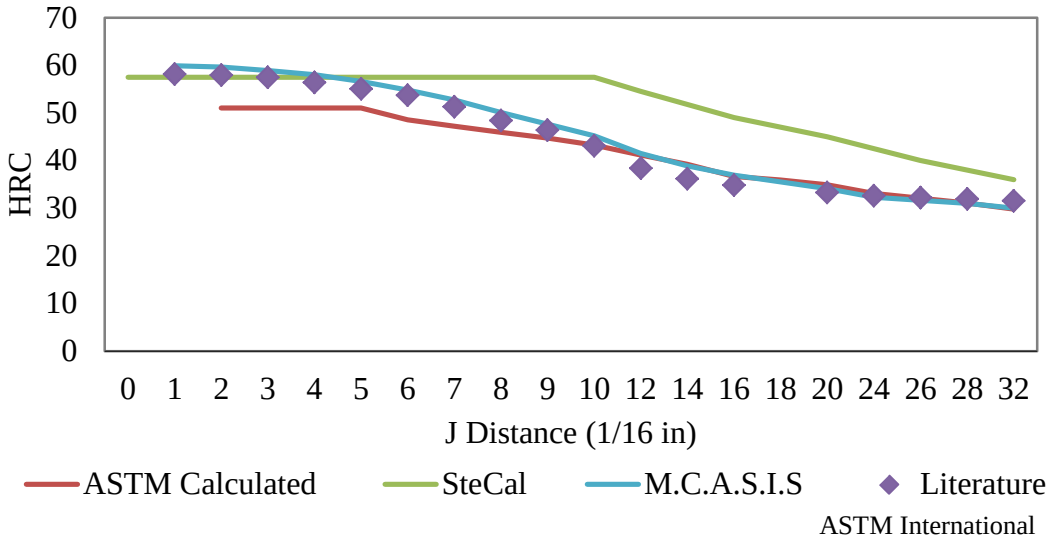

Figure 18: Jominy simulated comparison of 8740 steel(0.44wt%C, 0.58wt%Ni, 0.25wt%Mo, 0.50wt%Cr) to ASTM[18]

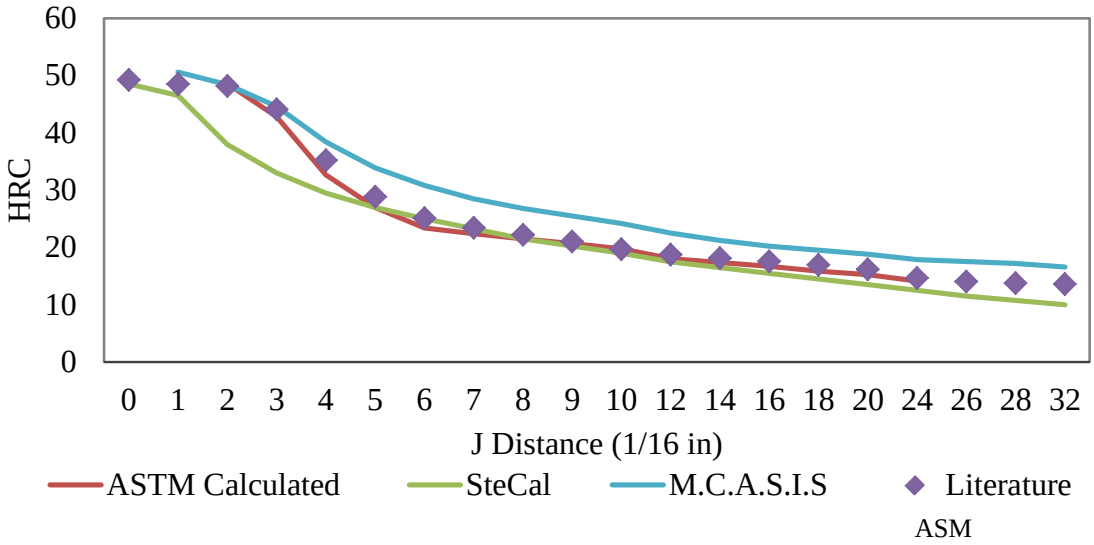

Figure 19: Jominy simulated comparison of 4130 steel (0.28wt%C, 0.40wt%Mn, 0.15 wt%Mo, 0.80 wt%Cr, 0.15wt% Si) to ASM [22]

3.9. Discussion

Table 3 Shows the depth of hardenability as per MPIF 35 represented as the depth of hardness of 65HRA (30HRC)[23]. In comparing the results found by MPIF 35 a continuous trend can be found; as the density increases so does the depth of hardening. It can also be seen that the results are in reasonable agreement with what was found in this investigation for the 4605 materials at 6.9g/cm^3.

Table 3: J-Depth as per MPIF 35 and Found via Experimentation

Density (g/cm^3)	MPIF Standard 35 J-Depth mm (16th inch) [23]	4605 J-Depth mm (16th inch)	4605+Cu J-Depth mm (16th inch)
6.76	3.18 (2)		
6.99	7.94 (5)	9.95 (6)	23.81 (15)
7.12	11.11 (7)		
7.30		17.46 (11)	Fully Hardened
7.70			Fully Hardened

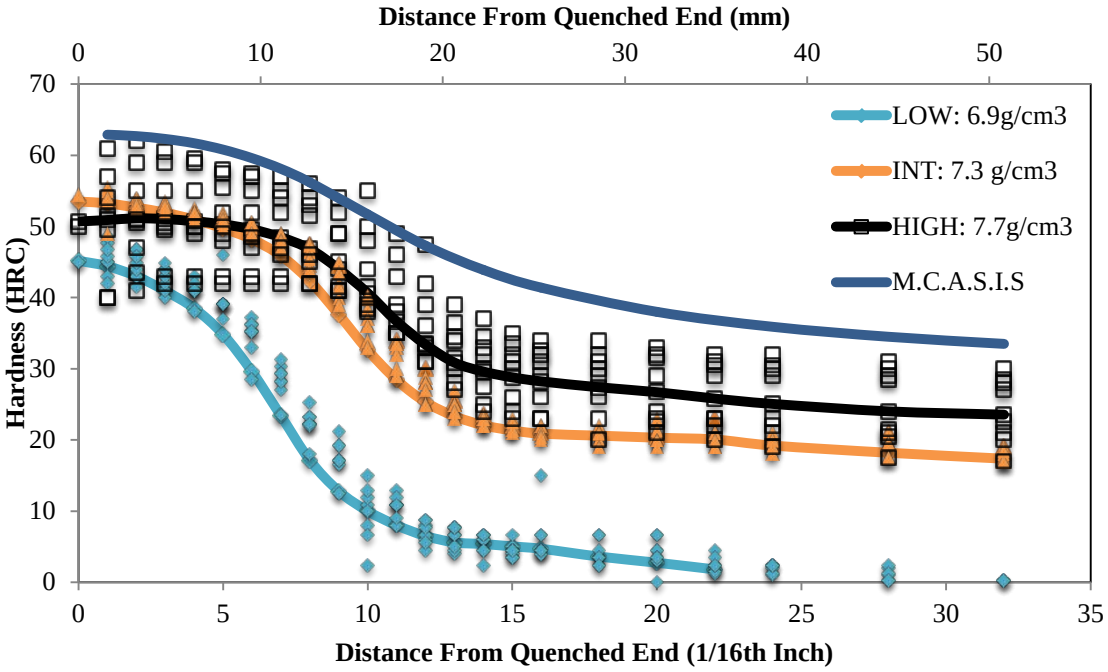

Figure 20: Averaged Jominy curves of HIGH, INT and LOW

It can be seen in Figure 20 and Figure 22 that there is a parallel shift in hardness to the Jominy curves as density decreases. The overall shape of each curve is very similar, especially in comparing the INT and HIGH results. This represents a similar depth of hardening since the increase of porosity will decrease the apparent hardness measurements observed by the hardness test. LOW has vertical shift, but also a horizontal shift of 7.9mm (5/16th inch). This shows that between 6.9g/cm^3 and 7.3g/cm^3 there is a critical density where martensite cannot form to a similar depth, thus showing a decrease in hardenability. This is confirmed when looking at the microstructure evolution shown Figure 21, where the microstructure is fully martensitic at the quenched end for all bars, yet changes with distance from the quenched end.

There are close similarities with the fraction of martensite between the INT and HIGH samples, where the LOW Jominy bar develops the diffusional phase much earlier. This is a clear indication of what was stated above by Warke, that an increase in porosity

increases the nucleation rate of ferrite and bainite [6], [7]. This information can also be interpreted by the decrease in thermal conductivity, where an increase in porosity decreases the thermal conductivity and allows for more time at intercritical temperatures for diffusion phases to form. This is however less relatable as shown in Figure 15 where the thermal conductivity is very close to that of fully dense material where the percent of porosity is 2.2%, 7.2% and 12.3% from most dense to least respectively.

martensite onset of phase duality ferrite-pearlite

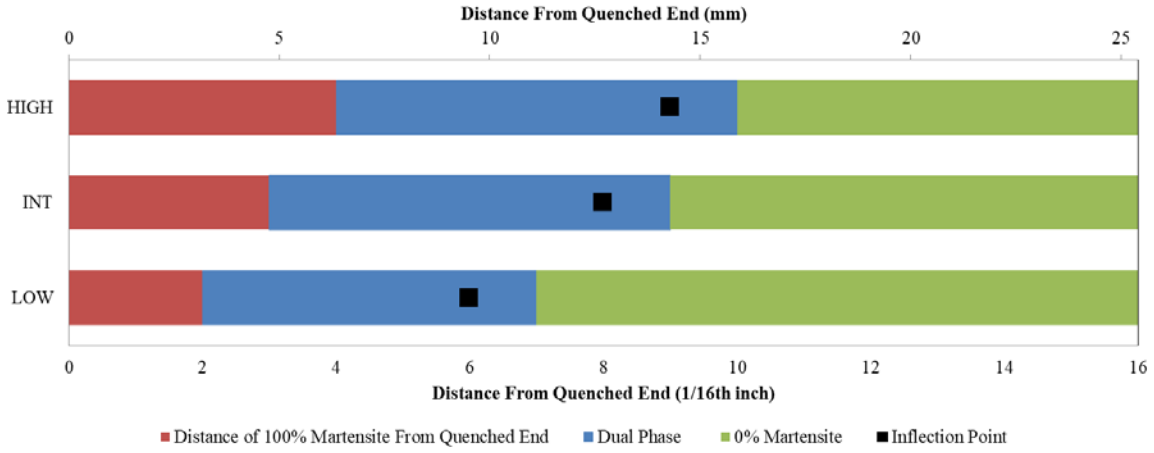

Figure 21: Extent of Martensite Formation for $\overline{Cu}$-HIGH, $\overline{Cu}$-INT, $\overline{Cu}$-LOW , martensite and dual phase micrographs are from $\overline{Cu}$-HIGH , ferrite-pearlite is from $\overline{Cu}$-LOW

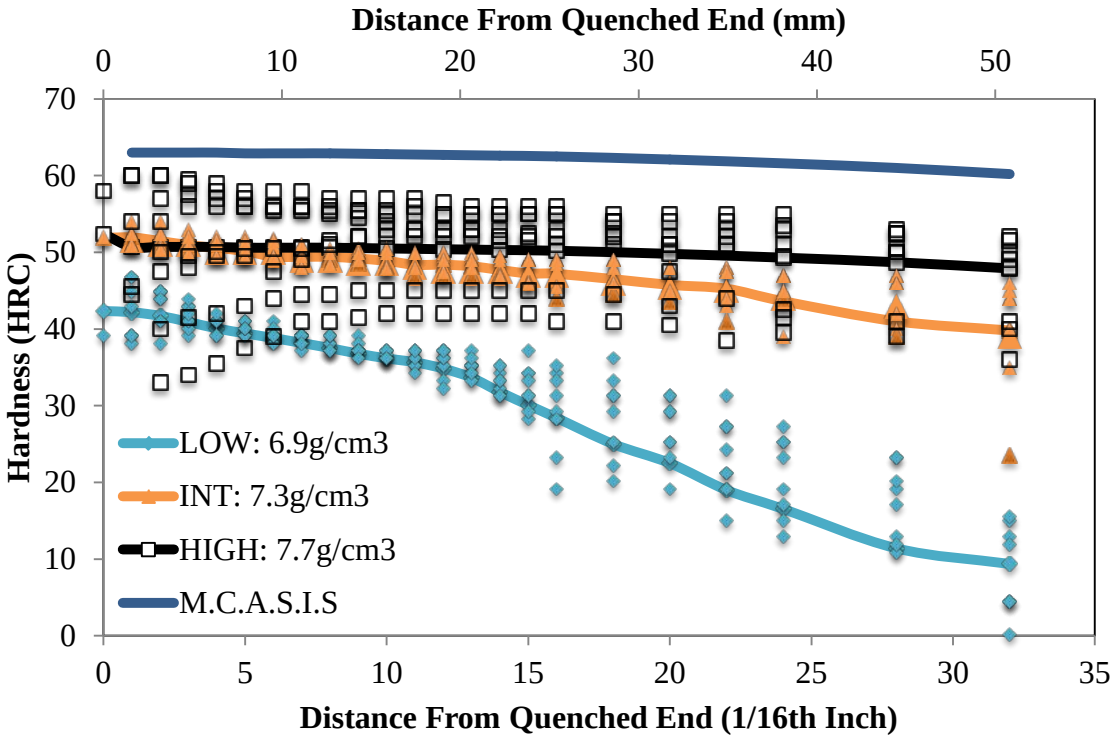

Figure 22: Averaged Jominy Curves of Cu-HIGH, Cu-INT and Cu-LOW

The addition of 2wt% copper to the 4605 powder significantly increased the hardenability of the steel. The threshold of hardenability can still be found in comparing CU_LOW to

CU_HIGH and CU_INT. It can be seen in Figure 22 that at 20.6 mm from the quenched end there is a significant change in the formation of martensite in this material. This is confirmed in Figure 23, where there is a significant fraction of martensite seen in the higher density material, and the nucleation of ferrite and cementite is seen around the porosity. It is well known that an increase in alloying elements will increase the hardenability of the material. The specific effect of copper can be quantified by its multiplying factor which can be seen here [24] and in chapter 2 compared to other alloying elements. In PM steel the addition of copper is known to increase the hardenability by other mechanisms. As seen in [5] the pore morphology becomes significantly rounder, expressing a higher magnitude of modes 2 and 3 of mass transport as described by Salak [1]. With a greater extent of closed pores there is less chance for heterogeneous nucleation of diffusional phases during slow cooling. This is potentially a reason for why there is a shallow change of hardness once the diffusional phases start to nucleate in comparing CU_LOW to LOW Jominy bars.

Martensite | Onset of phase duality | ferrite-pearlite

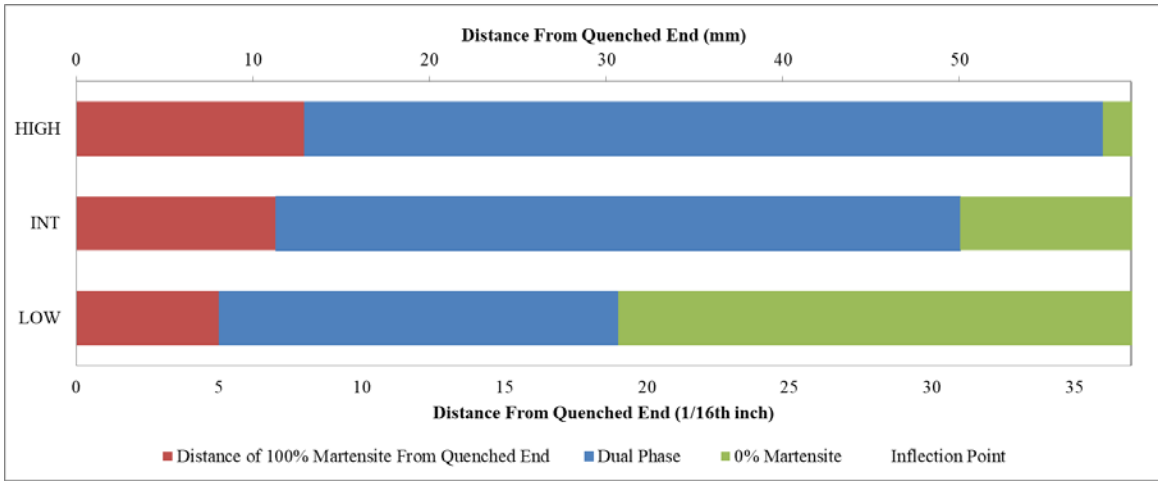

Figure 23: Extent of Martensite Formation for Cu-High, Cu-INT, Cu-LOW , martensite and dual phase are from Cu-HIGH sample, ferrite-pearlite is from Cu-INT

It should be noted that the inflection point is difficult to pinpoint, or does not exist, in copper containing Jominy curves. For this reason it is not incorporated in Figure 23.

3.10. Variations in Jominy Data

There are variations in the data seen, even though there are a total of eight data sets per density. In wrought steel these variations would suggest an extreme error in heat treating, or testing. Firstly lets remove any human errors, or an error within the test for they will only be slight and there were extensive efforts to mitigate them. The distance between indents as well as the parallelism was checked via microscopy measurements.

It is known that porosity can severely change the outcome of a mechanical testing [5]. Specifically with the Rockwell indenter the existence of a pore, or pore cluster under the indenter will produce a reading of extremely soft material.

The porosity is also known to exaggerate any decarburization, especially at densities equal to or below 7.0g/cm^3. For this reason there is a consistent decrease in hardness right at the quenched end of the Jominy bar. Due to the manufacturing steps this part of the bar has been exposed to the atmosphere through every step of the heat treatment.

Both the porosity and decarburization effects can be severely seen in the fully dense bars. As shown in Figure 24 these bars were first heated and then uniaxial pressed in the open atmosphere. During this procedure material is plastically deformed heterogeneously where the top edge, or side 4, resulting in a non-uniform distribution of density.

A B

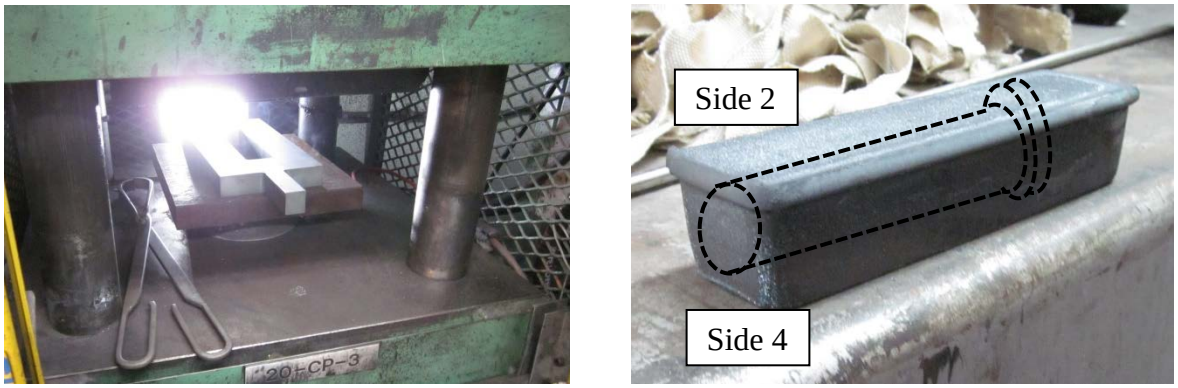

Figure 24: (A) press used on heated steel to forge steel specimen and increase density (B) Forged sample at 7.7g/cm^3

A similar phenomenon is found in green compacts where the most consolidation of powder occurs at the edges of the moving punch and die walls. This difference in porosity can be seen Figure 25, as well as the carbon content found via ASTME1091-11[25], where small samples were taken from the first 1.6mm (1/16th inch) of the quenched end of the Jominy bar. In comparing the carbon contents to the difference of martensite hardness for wrought steel, it can be seen that a 0.1wt% difference can be the cause of such a drastic difference in hardness. This along with the difference in porosity shows the ability for this processing to cause an anisotropic material. Moving farther away from the quenched end where ferrite and cementite began to form similar microstructures and hardness is seen.

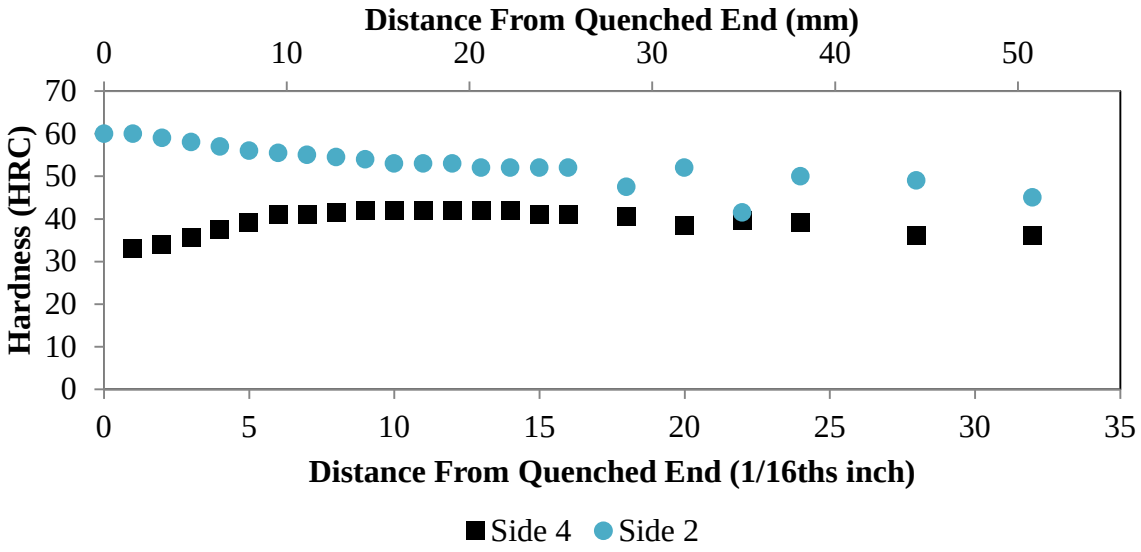

Side 4: C 0.37wt%

Side 2: C 0.49wt%

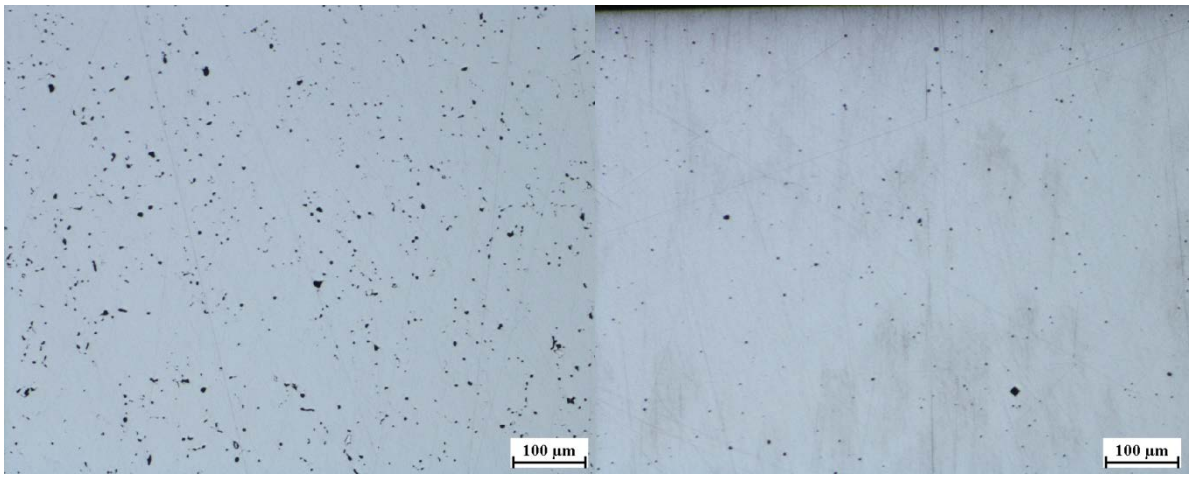

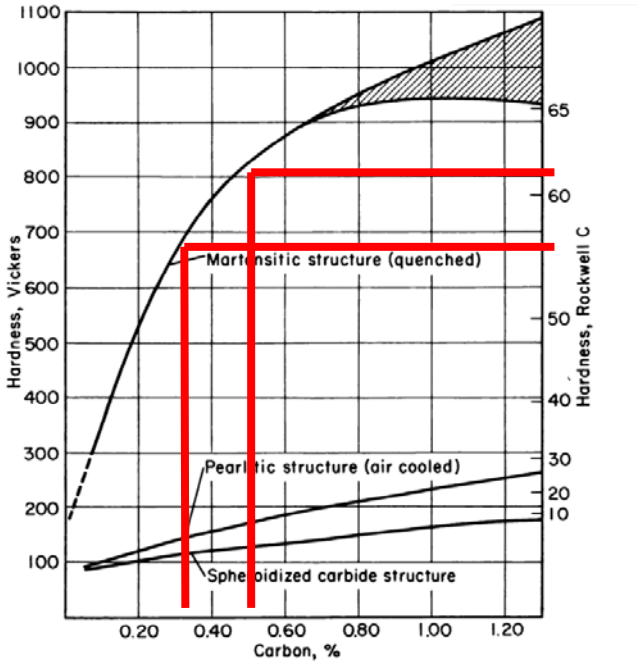

Figure 25: Comparison of side 2 and 4 of 4605 Jominy bar at 7.7g/cm^3 and the effect of carbon content on martensite hardness

3.11. Conclusion and Future Work

There is a clear effect of porosity on the formation of martensite, with a large decrease of porosity the steel will not be able to form martensite to the full extent as compared to a more dense counterpart.

Further studies should be done to find the critical density where the hardenability is most affected. If this density is pinpointed, a slight increase in density could relate to a large increase in hardenability.

The severity of decarburization should also be a warning to PM manufactures that further process steps at high temperature should always be conducted in protected atmospheres. The possibility for fluctuations in mechanical properties, such as hardness, would be detrimental to a steel product.

Considering the slight difference in thermal conductivity it is reasonable to contribute the difference of hardenability too more than just the heat extraction. With an increase in porosity, there is an increase in heterogeneous nucleation sites for diffusion phases to grow. This is balanced with an increased martensite start temperature until a critical density between 6.9g/cm^3 and 7.3g/cm^3.

From this experimental data a recommendation of decreasing the porosity to below or equal to 8% will ensure an increase in hardenability. To produce a more narrow range where this critical porosity is, and potentially increase the recommended porosity content further experiments should be done. It could be possible with a further investigation that a porosity-multiplying factor to compute a DI related to the density of the steel could be produced and tested. For example in Grossmann's equation for DI the multiplying factors have the ability to decrease the DI if they exist between 0 and 1. Therefore a multiplying factor or coefficient could be produced, related to density and the increase nucleation sites within the steel.

3.12. References

[1] Andre Salak, *Ferrous Powder Metallurgy*. 7 Meadow Walk, Great Abington, Cambridge CB1 6AZ, England: Cambridge International Science Publishing, 1995.

[2] Q.H. Zou, H. M. Zhao, D.Y. Zhang, M. Geng, Z.G. Wang, J.J. Lu, "Thermophysics characteristics and densification of powder metallurgy composites," *Powder Metall.*, vol. 49, no. 2, pp. 183–188, 2006.

[3] Liu Peisheng, Fu Chao, Li Tiefan, and Shi Changxu, "Relationship Between Tensile Strength and Porosity for High Porosity Metals," *Sci. China*, vol. 42, no. 1, pp. 100–107, 1999.

[4] R. Haynes, "A Theoretical Evaluation of the Strengths of Sintered Plain Carbon and Low-Alloy Steels," *Powder Metall.*, vol. 14, no. 27, pp. 71–77, 1971.

[5] G. Straffelini, C. Menapace, and A. Molinari, "Interpretation of effect of matrix hardening on tensile and impact strength of sintered steels," *Powder Metall.*, vol. 45, no. 2, pp. 167–172, 2002.

[6] Virendra S. Warke, Richard D. Sisson Jr., and Makhlouf M. Makhlouf, “The Effect of Porosity on the Austenite to Ferrite Transformation in Powder Metallurgy Steels,” *Mater. Sci. Eng.*, vol. A 528, pp. 3533–3538, Jan. 2011.

[7] Virendra S. Warke, Richard D. Sisson Jr., and Makhlouf M. Makhlouf, “The Effect of Porosity on the Austenite to Bainite Transformation in Powder Metallurgy Steels,” *J. Mater. Res.*, vol. 24, no. 10, pp. 3213–3219, Oct. 2009.

[8] V.S. Warke, Md. Maniruzzaman, R.D. Sisson, Jr., and M.M. Makhlouf, “Effect of Porosity on the Quenching Heat Transfer Characteristics of Powder Metallurgy Steels,” *Mater. Sci. Eng. A*, vol. 528, no. 10–11, pp. 3533–3538, Apr. 2011.

[9] Virendra S. Warke, Richard D. Sisson Jr., and Makhlouf M. Makhlouf, “A Model for Predicting the Response of Powder Metallurgy Steel Components to Heat Treatment,” *Mater. Sci. Eng. A*, vol. 518, no. 1–2, pp. 7–15, Aug. 2009.

[10] K. Mahesh, S. Sankaran, and P. Venugopal, “Microstructural Characterization and Mechanical Properties of Powder Metallurgy Dual Phase Steel Preforms,” *J Mater Sci Technol*, vol. 28, no. 12, pp. 1085–1094, 2012.

[11] Suleyman Saritas, Roger D. Doherty, and Alan Lawley, “Effect of Porosity on the Hardenability of P/M Steels,” vol. 38, no. 1, p. The International Journal of Powder Metallurgy, 2002.

[12] P. Grootenhuis, R.W Powell, and R.P. Tye, “Thermal and Electrical Conductivity of Porous Metals made by Powder Metallurgy Methods,” *Proc. Phys. Soc. Sect. B*, vol. 65, no. 7, pp. 502–511, 1952.

[13] J.C.Y Koh, “Prediction of Thermal Conductivity of and Electrical Resistivity of Porous Metallic Materials,” *Int. J. Heat Mass Transf.*, vol. 16, no. 11, pp. 2013–2022, Nov. 1973.

[14] M.I. Aivazov and I.A. Domashnev, “Influence of porosity on the conductivity of hot-pressed titanium-nitride specimens,” *Transl. Poroshkovaya Metall.*, vol. 9, no. 69, pp. 51–54, Apr. 1967.

[15] D. J. Stiles, “Effect of porosity on thermal response, hardness, hardenability and microstructure of powder metallurgy steels,” *Surf. Eng.*, vol. 21, no. 1, pp. 12–16, Feb. 2005.

[16] F. J. Semel and D. A. Lados, “Simulated effects of martensite start temperature, thermal conductivity and pore content on end quench cooling rate,” *Powder Metall.*, vol. 52, no. 4, 2009.

[17] G.F. Bocchini, B. Rivolta, G. Silva, M.G. Ienco, M.R. Pinasco, and E. Stagno, “Influence of density and surface/volume ratio on the cooling speed of sinter-hardening materials,” *Adv. Powder Metall. Part. Mater.*, pp. 60–72, 2002.

[18] ASTM International, “Standard Test Methods for Determining Hardenability of Steel.” ASTM International, West Conshohocken, PA.

[19] M.A. Grossmann, *Elements of Hardenability*. Cleveland Ohio: American Society of Metals, 1952.

[20] Rafael Calvo Rodes *et al.*, “Description and instructions for the handling of the steel calculator and the calculation of the representative properties of steels.” National Institue of Aeronautical Technology “Esteban Terradas,” 1961.

[21] Minitech Limited, “M.C.A.S.I.S The Minitech Computerized Alloy Steel Information System Version 2.1 User Manual.” Minitech Limited, 71 Paisley Ave N, Hamilton Ontario L8S 4H1, Jan-1996.

[22] ASM International, *ASM Handbook 04 - Heat Treating*, vol. 4. 1991.

[23] MPIF, “MPIF Standard 35.” Metal Powder Industries Federation, 2012.

[24] Per Lindskogt, “Controlling The Hardenability of Sintered Steels,” *Powder Metall.*, vol. 13, no. 26, 1970.

[25] ASTM International, “Standard Test Methods for Determination of Carbon, Sulfur, Nitrogen, and Oxygen in Steel, Iron, Nickel, and Cobalt Alloys by Various Combustion and Fusion Techniques.” ASTM International, West Conshohocken, PA.

4: BASE POWDER SIZE'S EFFECT ON SINTERING AND HARDENABILITY

4.1. Abstract

An ability to calculate the hardenability is built on the assumption that alloying elements are distributed evenly. This assumption is realistic for wrought steels, but questionable for PMS: time allocated to sintering may not be sufficient for relaxation to homogeneity. Using prealloyed powders resolves the problem, but such mixtures typically demonstrate poor compressibility. A question might come to you: what happens to these localized sources during sintering? Efforts have been made to answer this question numerically, yet the complexity has shown daunting [1]. It is intuitively clear that with smaller particles of Fe sintering time can be reduced. An experiment was designed to investigate the Fe-powders' sizes on hardenability. Results were quantified by comparing Jominy curves of Fe-C-Cr-Mn-Mo-Ni PM steel composed of three different size distributions of Fe powder.

4.2. Introduction

The ability to predict the depth of martensite formation of steel has been a useful industrial tool, which was first quantified by Grossman, and then further analyzed and improved by Jominy [2], [3]. The weight percent of alloying additions, along with the austenitic grain size is directly linked to the formation of martensite [4]. Great effort has been made, such as in [5], to understand how specific alloying elements affect the corresponding Jominy curves. From this a regression equation was made which provides the hardenability (D) in inches. This equation can be seen in equation(12), yet should be used with caution because it is only accurate over a very specific ranges of composition [5].

(12)
$$D = -0.172 + 0.1681C + 0.126\mathrm{Mn} + 0.0875\mathrm{Si} + 0.152\mathrm{Ni} + 0.280\mathrm{Cr} + 0.680\mathrm{Mo} + 0.246\mathrm{Cu} + \mathrm{Sn} - 0.0154GS$$

Using computations as expressed by Jominy, Grossman and other authors as shown above can be used to predict the ideal diameter and Jominy curves given the alloying concentrations and grain size. These computations rely on a significant assumption that there is a complete homogenization of alloying elements. This assumption does not always hold true to PM steel when sintering times do not allow complete homogenization. In admixed PM steel, iron powder is mixed with various sources of alloying additions and pressed into a greenbody before sintering. These sources are visible in Figure 26, where the bright regions are the sources of alloying additions.

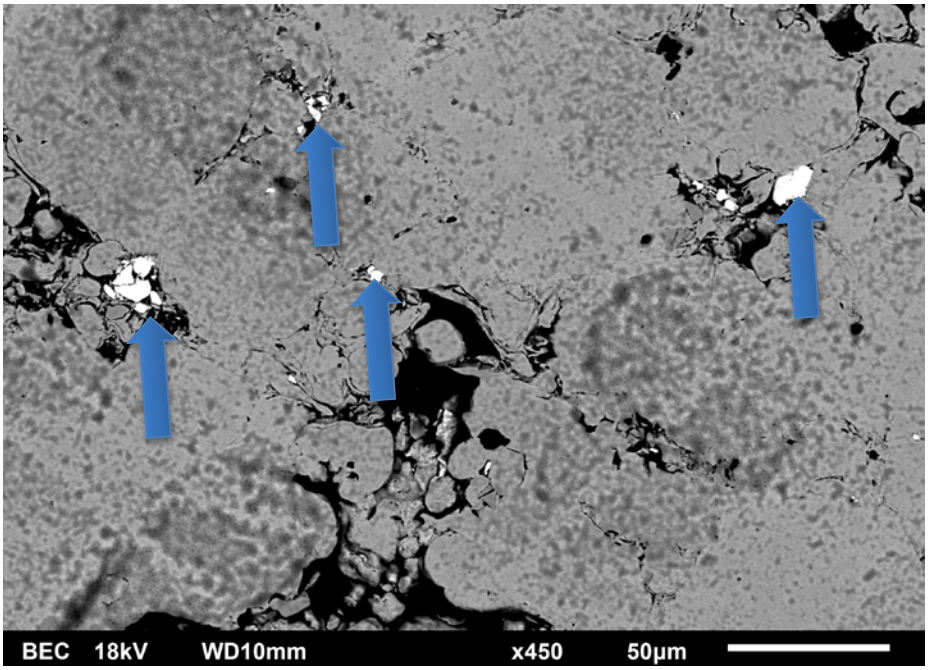

Figure 26: Backscatter electron image of greenbody sample pressed to 7.0g/cm^3, arrows showing sources of alloying additions

It is important to note the path the atoms take during sintering, that they travel first towards high surface energy regions of sharp angles along the outer surface of neighboring particles, causing necking. This was outlined in Chapter 1, Figure 3, and reiterated in Figure 27 for the reader's benefit. After this alloying elements will travel deep within the Fe matrix along concentration gradients [6].

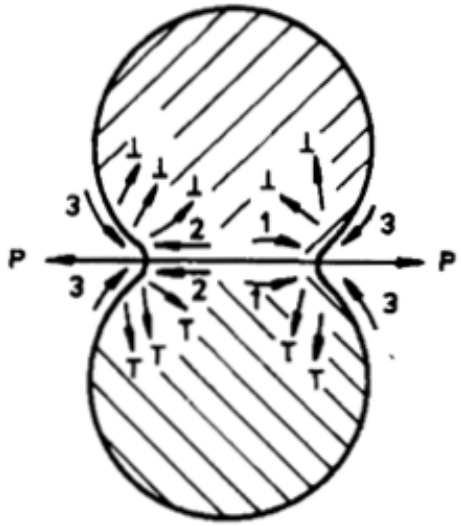

Figure 27: Diffusion routes for atoms: 1) mass moving outward 2) grain boundary diffusion 3) surface diffusion [6]

A potential “simple fix” of increasing the alloyed concentrations will produce inefficiently element-rich mixtures in which central parts of large particles remained under alloyed. This diffusion path results in a situation when formation of martensite occurs between unalloyed Fe particles, and therefore the microstructure will be uneven, with the fraction of martensite varying from point to point.

It is therefore self-evident that the reduction of size of the initial Fe particles will allow for a greater diffusion of alloying elements during sintering. This also has the potential effect of increasing density, yet also decreasing the processability of the powder.

4.3. Powder size and Shrinkage

Densification is a well-known phenomenon in powder metallurgy [7]. Densification occurs *via* the diffusion process, where atoms move towards regions to decrease high solid-gas interfacial surface energy. When this occurrence dominates over thermal expansion the greenbody part will shrink. Factors such as time, temperature, atmosphere, powders used and compacting pressure affect the densification of PM steel. It is also important to note that the densification rate is highest at the initial heating stage of the

sintering process. Factors that affect densification are outlined in many literary sources, [6], [8], [9], [7] which are further summarized in the appendix for the reader.

There is not much literature on how the initial size of PMS powder directly effects the hardenability of sintered steel. A size affect analysis on metal powder was conducted for T15 tool steel, using the powder metal method of hot-isostatic pressing, and it was concluded that the finer powder produced superior steel than the commercially available distribution due to a smaller size of the MC and M_6C carbide phases present[10].

The literature on PM stainless steel shows a focus on the uniform Cr distribution for protection against corrosion. Specifically the use of smaller particles decreases the pore volume fraction and size of PM stainless steel during high-temperature sintering. This lead to a more corrosion resistant material [11]. It was also interesting to note that ferritic powders reduced the amount of pores more than the austenitic powders of similar size. This is due to the faster solid-state diffusion in BCC ferrite, than FCC austenite [11], [12]. For example the diffusion coefficient of C in α-Fe is 2.2×10^{-4} m^2/s, where in γ-Fe it is 1.5×10^{-5} m^2/s [12].

Vivas et al. noted a difference in pore size and shape with a change of initial particle size. In the case of a small particle size distribution (less than 63 microns), and high density parts, closed pore structures were found; yet this was not the center of the investigation [13].

It is known that as density decreases there is a heterogeneity increase, seen in [14] where PM steel measured at a density of $6.6g/cm^3$ was compared to the same PM steel at $7.0g/cm^3$ and showed slightly more scatter in Ni after industrial sintering at 1120C for 25 min in the latter steel.

4.4. Synergistic Modes of Sintering

Let us reiterate that the size and composition of the initial particles have an affect on the sintering rate. In nickel containing PM steel, variations in compositional uniformity are often found. These modulations can be detrimental to the mechanical properties as Ni-rich areas that are soft due to the lack of carbon [15], [16]. An extreme example of this can be seen in Figure 28, where a very large pure Ni particles was found unalloyed in a sintered PM steel at 7.0g/cm^3 composed of 0.3wt%Ni, 0.3wt%Cr, 0.4wt%Mn and 0.4wt%C after sintering for 30 minutes at 1280℃. The WDS maps in Figure 28 were found by cooperation with Western University's geological department.

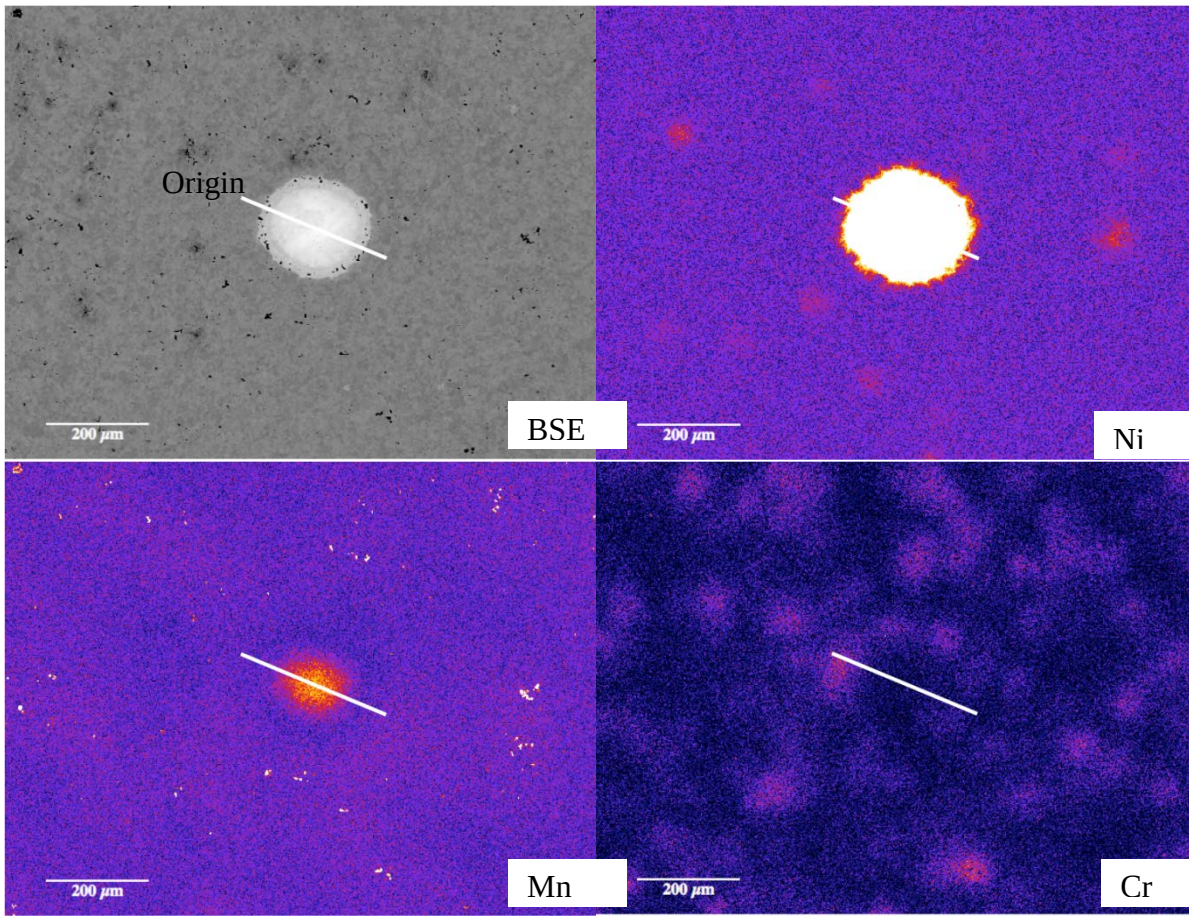

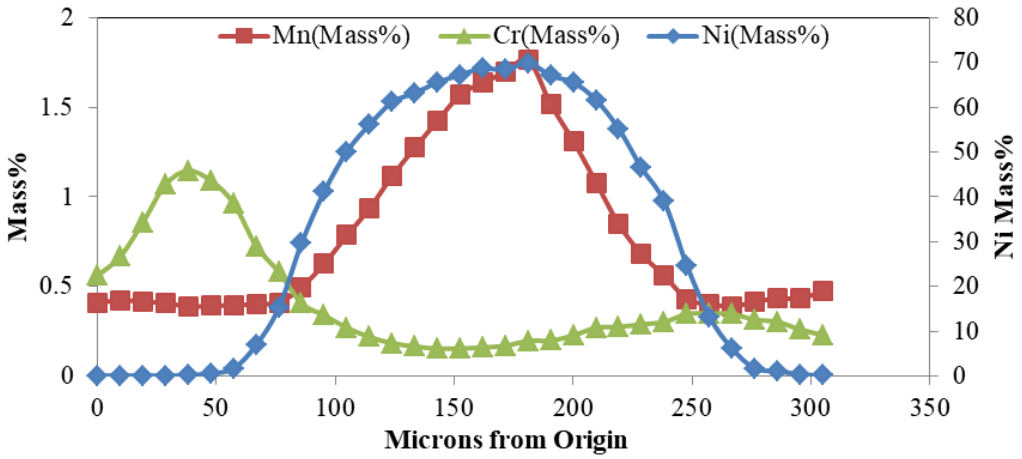

Figure 28: WDS Map of Sintered Steel

The Ni WDS map shows a lack of diffusion of Ni in Fe at the sintering time and temperature. This can also be seen in the diffusion coefficient of Ni in austenitic Fe being $7.7\times10^{-5}\,m^2/s$, and Fe in Ni being $8.0\times10^{-5}\,m^2/s$, showing a slightly higher affinity for Fe to travel through a Ni matrix than Ni traveling through an Fe matrix [13]. In light of this it was found that a smaller initial size Ni particle corresponds to more homogeneous sintered PM steel [17].

4.4.1. Mn Diffusion within Ni

It can be seen that the high concentrations of Ni is followed by high concentrations of Mn in Figure 28. It is apparent that during the sintering process the Mn not only travelled through the Fe matrix, but when in contact with the Ni particle it was drawn towards the center of the particle. This produced a lower concentration of Mn surrounding the Ni particle, and a higher concentration within the center.

In collecting what is known about Fe, Ni and Mn with regards to the affinity of diffusion a possible answer could become clear. First the system must be defined before a hypothetical solution can be imagined and defended. Imagine a large pure Ni particle within a matrix of Fe and Mn particles before sintering. Ni as stated has a lower affinity to diffuse into the Fe matrix than the Fe has to diffuse into Ni. It is also known that the

diffusion activation enthalpy of Mn is lower than that of Ni within an FCC crystal structure [18]. Pure Ni, as well as high concentration of Ni with respect to Fe and Mn exists as an FCC structure, this can be seen in the Fe-Ni and Mn-Ni phase diagrams in Figure 29.

Therefore in this situation as temperature increases such that the Fe matrix is in the FCC austenitic region, Mn and Fe will diffuse into the Ni particle, while Ni will diffuse out towards the FCC Fe-Mn matrix. After the high temperature region in the sintering furnace, the PM steel undergoes very slow cooling to room temperature. Once the temperature decreases below A3 the BCC phase will start to nucleate within the Fe matrix, where the high Ni regions will stay as FCC. Therefore in this situation if the Ni particle is looked upon as not willing to diffuse, yet Mn and Fe are, the high concentration gradient of a pure Ni particle, lacking Mn and Fe, will make the surrounding Mn and Fe move towards the center of the pure Ni. This is accelerated when the surrounding matrix is in the BCC phase.

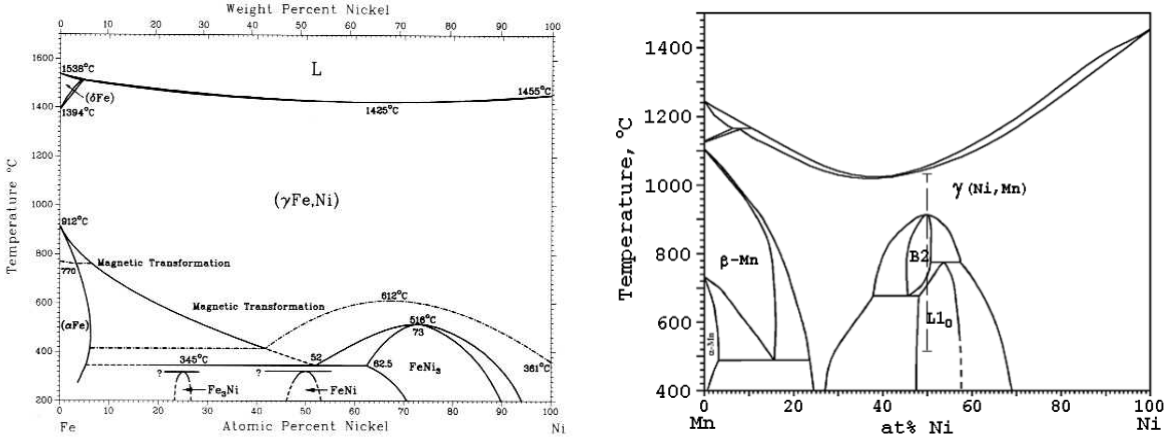

Figure 29: Fe-Ni and Mn-Ni Phase Diagrams [12], [18]

It is interesting to note that the diffusion activation enthalpies of Ni and Mn are very similar within the BCC structure. This is not the case in the FCC phase such that the Ni has a higher activation enthalpy than Mn. In a paper by Peteline where self-diffusivity of

Mn-Ni systems were found, a conclusion was stated that this could lead to a “coupled mechanism of diffusion” during the transformation of FCC to the BCC phase [18].

To increase the overall diffusion of Ni, it was found that the addition of molybdenum and carbon to the iron-nickel powder blend improved the distribution of nickel in the sintered steels, yet was not statistically verified [19]. It was also found that the addition of copper to an iron-carbon-nickel powder helps in the distribution of nickel. During the sintering of Fe-Ni PM steel, the Ni was found to move along the surface of the pores, and did not penetrate deep into the iron particle. The addition of copper allows for liquid state diffusion between the pores due to copper’s lower melting temperature. Therefore when liquid copper interacts with Ni at the surface of the Fe particles the mass transfer will be controlled by the liquid phase. The liquid Cu-Ni phase will continue to exist as a liquid up to 25wt%Ni at industry high temperature sintering temperatures, therefore the Cu-Ni liquid can now diffuse deeper into the Fe particle [12], [19].

4.5. Experimentation

Three PM Steel blends were produced with the same alloying constituent concentrations shown in Figure 30. The Fe powder used in each blend was first sieved to the prescribed, coarse, fine and reference sizes also shown in Figure 30, where the reference iron powder was composed of the entire histogram.

Element	C	Mn	Cr	Ni	Mo	Fe
Wt%	0.56 ± 0.08	0.76 ± 0.05	0.52 ± 0.07	0.48 ± 0.01	0.37 ± 0.02	Bal.

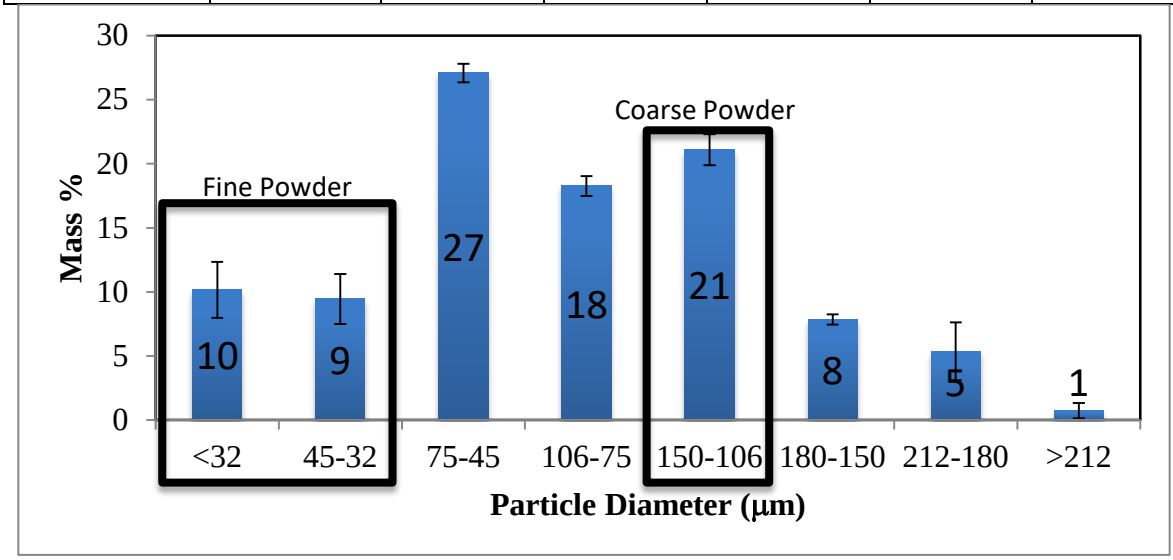

Figure 30: Alloying Constituents and Size analysis of reference industrially used Fe powder from Stackpole International via sieve analysis

The sources of Mn, Mo and Cr started from very fine (~12μm in diameter) ferroalloy sources, which can be seen in Table 4, composing mainly of the specific alloying element and Fe to hinder the formation of oxides on the large amount of surface area found on such small particles.

Table 4: Constituent sources from ferroalloy powders

FeCr			
Element	**Cr**	**Fe**	**C**
Wt%	61	30	9
FeMn			
Element	**Mn**	**Fe**	**C**
Wt%	76	17	7
FeMo			
Element	**Mo**	**Fe**	**C/Si/P/S/Cu**
Wt%	61	38	1

Following an industrial blending procedure of 45 minutes the powder blends were subject to compacting[3] at pressures found in a previous study in an effort to reach 7.0g/cm^3[17]. The fine powder blend was pressed with 621Mpa, coarse powder and reference blend was

[3] Compaction completed by PowderTech

pressed with 483Mpa to produce 2 test groups per blend in dimensions of 3.8x3.8x16cm. The greenbodys were then industrially sintered at 1280°C for a total of one hour (two heats of 30 minutes at high temperatures) to reach the sintered densities seen in Figure 33. It should be noticed the fine powder samples increased in density at a greater magnitude than the coarse samples. The increase in densification is due to the increase in surface area of the fine powder in the greenbody part before sintering. Each steel was made of two test groups, where for example, test group 1 incorporates a test sample from each steel blend type, coarse, fine and reference. This is also expressed in Figure 33. A densification summary can be seen in the appendix. The 30 min heat treatment schedule can be found in the Appendix. Jominy bars were then manufactured from the sintered bars. Before the sintering step the reference material was inspected via SEM in the greenbody state to gather an understanding of how the alloying additions were arranged.

4.5.1. Greenbody Analysis

An EDS point analysis was done on the following sites to determine the original positions of the sources of alloying elements. There was no standard used in the calibration of this analysis, so the concentrations are not supposed to be trusted quantitatively, or semi-quantitatively. Understanding this changes the results, yet does not make an analysis moot; the composition of the alloying powders are already known, so any indication of Mo, Ni, Cr or Mn will be enough to determine the origin of the particle. The results of this analysis are shown in Figure 31 and Table 5.

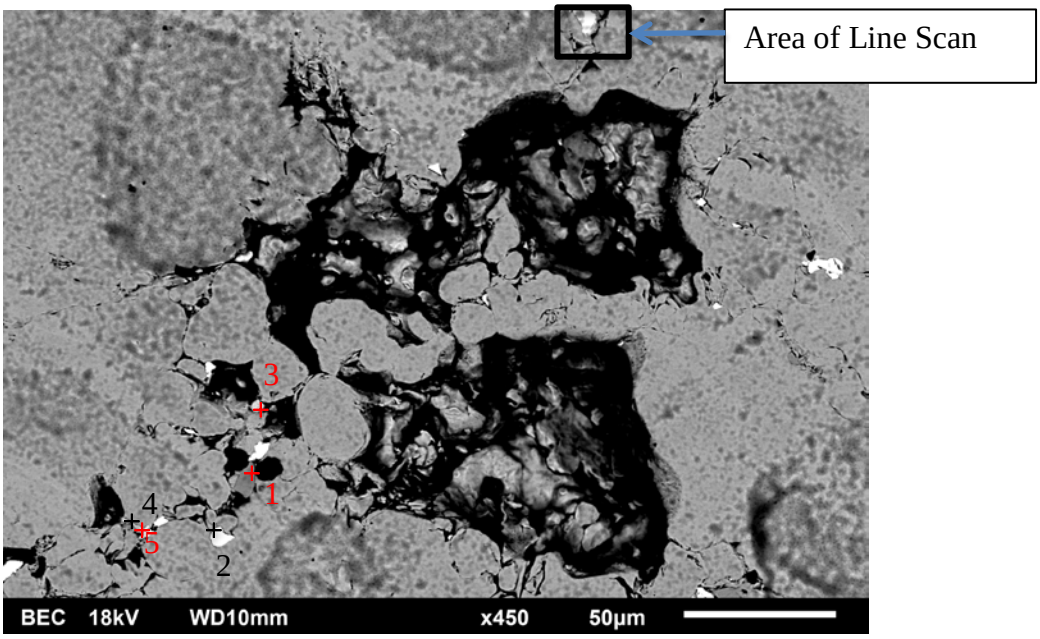

Figure 31: BSE-SEM Micrograph of reference steel blend in its greenbody state, before sintering, analyzed with EDS

Spot Number	Composition found via EDS					Original Particle	Particle Area μ^2
	Fe wt%	Cr wt%	Mn wt%	Mo wt%	Ni wt%		
1	24.2±0.2	57.5±0.3	0.3±0.1	0.0+0.1	0.1±0.3	Cr	548.4
2	27.0±0.2	0.1±0.1	0.0±0.1	55.3±0.3	0.1±0.1	Mo	313.9
3	6.8±0.1	0.2±0.0	0.1±0.1	0.0+0.1	79.6±0.3	Ni	126.6
4	10.7±0.1	0.0±0.0	0.2±0.1	0.5±0.1	69.7±0.3	Ni	114.4
5	41.7±0.3	0.1±0.1	0.2±0.1	40.8±0.3	0.1±0.1	Mo	60.5

Table 5: EDS-SEM Spot Analysis data of areas shown in BSE-SEM Micrograph

The cross sectional area was measured for each of the particles above via ImageJ, due to the non-spherical shape of the particles this measurement can express the relative sizes of the particles without assuming a constant diameter. Unfortunately a Mn particle was not found in this analysis. The particles shown in spots 4 and 5 are touching. This was further investigated, and is shown in a line scan of another area shown in Figure 31, and magnified in Figure 32.

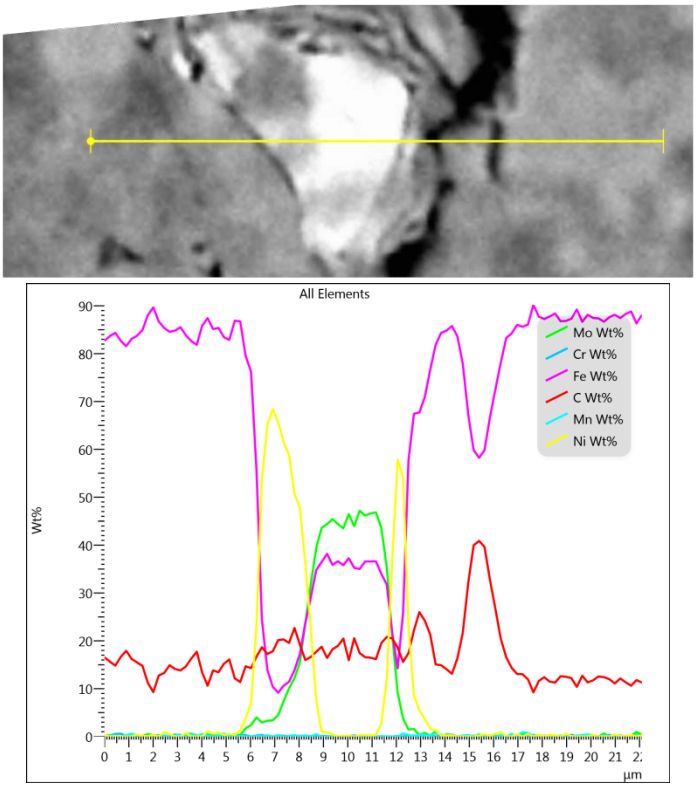

Figure 32: Line scan of magnified area from Figure 31

It can be seen that elemental Ni has become entangled with a Mo particle, showing that alloyed particle agglomeration occurred twice within this a 0.6mm^2 micrograph. If there is potential to purposely agglomerate certain admixed alloyed powders, an enhanced synergistic mode of diffusion can be designed for sintering optimization.

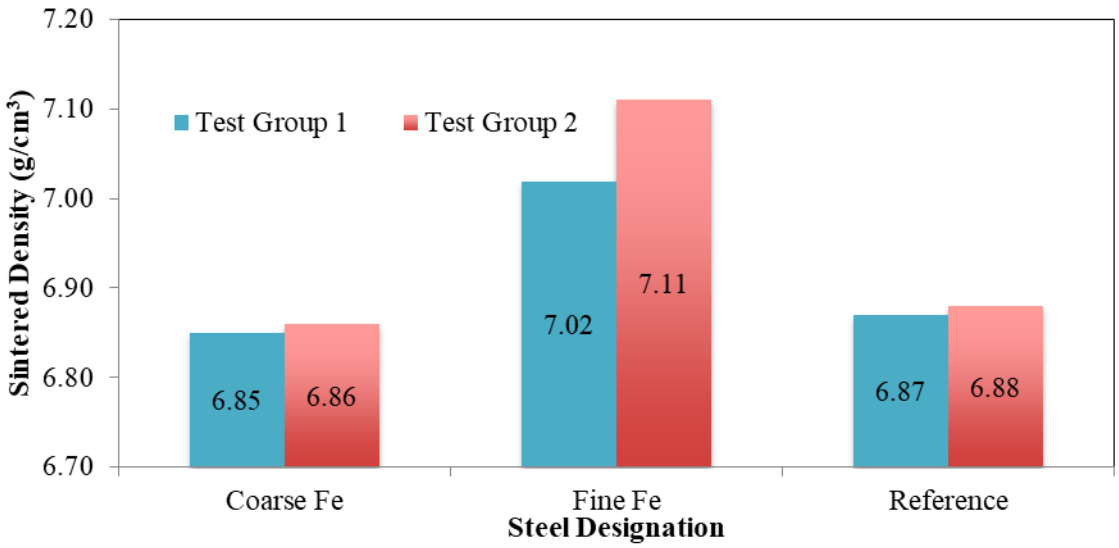

Figure 33: Sintered Density of Test Groups

The jominy bars were heat treated as per ASTMA255 for steel with a carbon content above 0.50wt%: 30minutes at 900°C surrounded in coke to prevent decarburization. The samples were then quickly removed from the heat source and placed in the end quench tank. After heat treatment four edges, 90degress separated, were machined with careful temperature control. Hardness testing was completed as per MPIF45 and ASTMA255.

4.6. Data – Jominy Curves

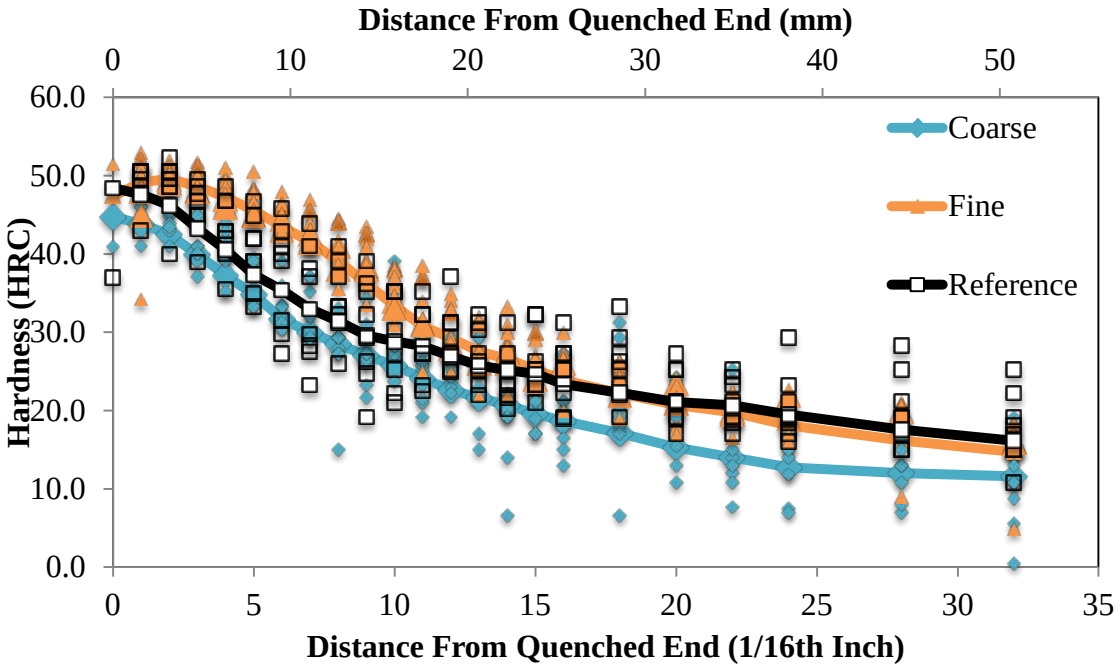

Figure 34: Jominy Curves of fine, coarse and reference material found by averaging 8 curves per blend

Table 6: J-Depth (distance to 30HRC) of fine, coarse and reference material

Sample	Fine	Coarse	Reference
J-Depth mm (1/16th inch)	17.5 (11)	9.5 (6)	12.7 (8)

The hardness test produces large plastic strains just below the indenter and therefore is a quick indication of the flow strength of the bulk material [20]. The presence of porosity is detrimental to this test, and it is therefore important to understand the potential variability of the results, this is seen in the chapter 3 and the spread of data in Figure 34 as well as the parallel shift from the simulated curve through M.C.A.S.I.S.

It can be seen that the shape of the curve produced by the fine powder material is different than the reference and coarse material. The inflection point is at very similar positions, 7.9mm (5/16th inch), where the fine material doesn't show a drastic change in hardness until 15.9mm (10/16th inch). This shows an increase in hardenability. As stated

in the previous chapter that there could be a region of porosity that has a detrimental effect on hardenability in this density range. If it is the case that the difference of 2.5% porosity of the fine and coarse material is affecting the hardenability it is doubtful that it will have an effect of this magnitude.

In Figure 35 it can also be seen that there is a significant difference in microstructure, which was not found in the previous study, and therefore must be attributed to more than a change in porosity. Specifically this can be seen at 9.6mm ($6/16^{th}$ inch) where there is still a significant amount of martensite seen in the fine material compared to the other two.

The similarity of hardness and microstructure of all samples can be seen at 17.5mm from the quenched end. The microstructure shows a similar amount of ferrite between the reference and fine material, where the coarse material shows an increase in the ferrite-cementite structure, which corresponds to the hardness in that area.

The fine iron matrix in a past study contributed to the overall uniformity of the alloying elements, such that smaller initial particles showed qualitatively more uniform distribution of Mn, Cr and Ni. It should also be noted that the grain size and porosity was also changed by the initial Fe particles, where large pores and grains are produced with larger initial Fe powder [17]. This can be seen in the hardenability of a similar material. It has been shown above that the element least willing to alloy the base Fe matrix is Ni. Lets assume that Ni could not homogenize some areas within the material. By calculating the *DI* in M.C.A.S.I.S the alloy without Ni shows a negative difference of 1mm. This is a simplified version of the complex diffusion pathways within the sintered material, yet it shows how if not every element is being used within the material, Martensite will not form to the same extent.

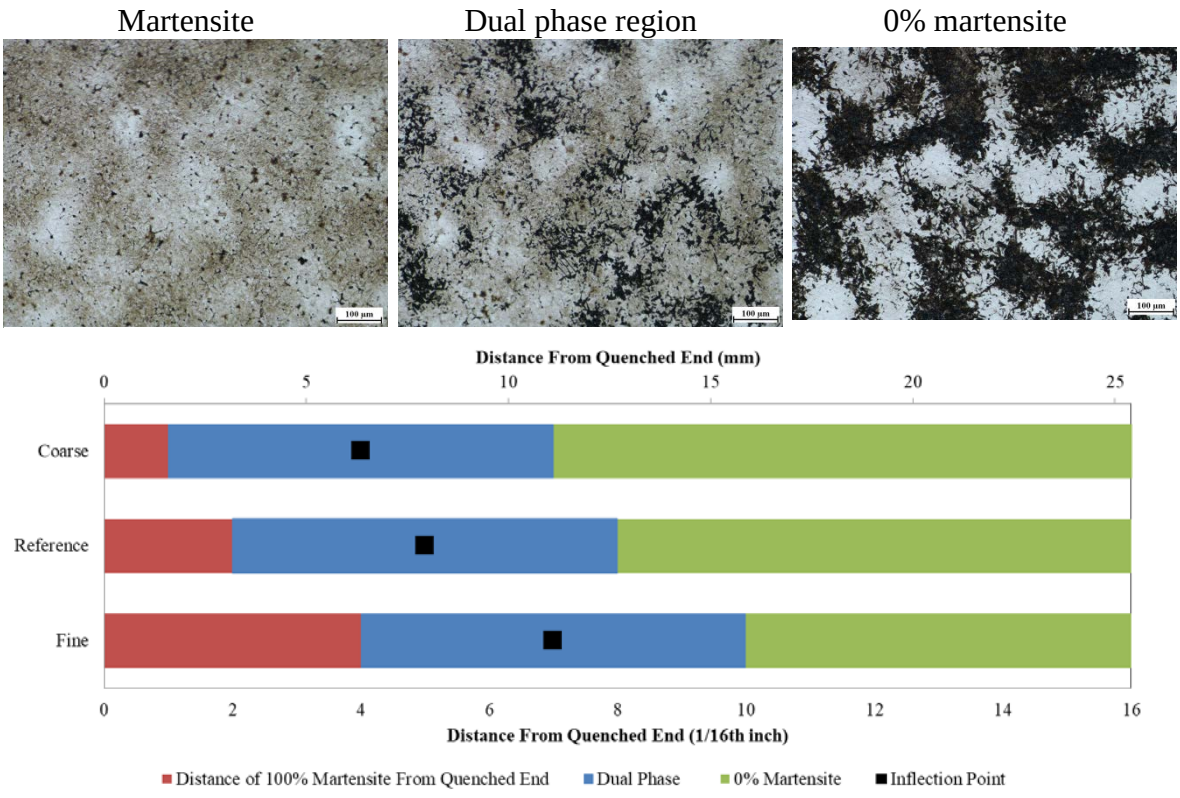

Figure 35: Microstructure Evolution of Fine, Coarse and Reference Jomniny Test, micrographs are from material made from fine Fe powder

4.7. Conclusion

The development of materials relies on the ability to predict the effect that process variables will have on the final structure. This was done by relating the difference of initial process variable, powder particle size, to the final microstructure.

There is a clear difference in the hardenability of PM steel manufactured from different sized Fe powder. Fine powder produces a more homogenous mixture of alloying elements, allowing for a greater fraction of martensite to form under the same heat treatment. The fine powder steel samples also had a higher density, which can increase the hardness measured by the Rockwell indenter. It is therefore better to compare the location of the inflection point and shape of the hardness curve. In this way it is easy to see the greater depth of hardness the fine samples.

It is also clear that since the reference and coarse material was very similar in hardenability that large Fe particles are not only detrimental on their own, but when mixed with other sizes. The next chapter will continue on this train of thought, in determining the limit to the volume fraction of these large particles.

This investigation was unable to gather clear quantitative information on the synergestic modes of diffusion for this alloy. In fact, it would be very difficult to pin-point without further investigations. This could be done with further WDS maps of sintered material. If this was the case, it should be incorporated so further recommendations can be assisted with this knowledge. A useful insight to industry would be sources of alloying elements that could be used to increase the diffusion distance of others as well.

4.8. References

[1] Nilushi C. Kariyawasam, B.ENG., "Advances In Sintering of Powder Metallurgy Steels," Masters Thesis, McMaster University, Hamilton, ON, 2017.

[2] M.A. Grossmann, *Elements of Hardenability*. Cleveland Ohio: American Society of Metals, 1952.

[3] Metal Powder Industries Federation, "Method for Sample Preparation and Determination of the Hardenability of PM Steels (Jominy End-Quench Hardenability)." 2007.

[4] Edgar C. Bain and Harold W. Paxton, *Alloying elements in steel*, 2nd ed. Metals Park, Ohio: American Society for Metals.

[5] G.T. Brown and B.A. James, "The Accurate Measurement, Calculation, and Control of Steel Hardenability," *Metall. Trans.*, vol. 4, pp. 2245–2256, Oct. 1973.

[6] Andre Salak, *Ferrous Powder Metallurgy*. 7 Meadow Walk, Great Abington, Cambridge CB1 6AZ, England: Cambridge International Science Publishing, 1995.

[7] P. R. Kalischer, "The Effect of Particle Size on the Shrinkage of Metal Compacts," *Symp. Powder Metall. Am. Soc. Test. Mater.*, pp. 31–40, Mar. 1943.

[8] Q.H. Zou, H. M. Zhao, D.Y. Zhang, M. Geng, Z.G. Wang, J.J. Lu, "Thermophysics characteristics and densification of powder metallurgy composites," *Powder Metall.*, vol. 49, no. 2, pp. 183–188, 2006.

[9] Kishor M.Kulkarni, "Effect of Particle Size and shape on Sintering of high Speed Steels," *Mod. Dev. Powder Metall.*, vol. 19, 1988.

[10] K.S. KUMAR, A. LAWLEY, and M.J. KOCZAK, "Powder Metallurgy T15 Tool Steel: Part II. Microstructure and Properties after Heat Treatment," *Metall. Trans. A*, vol. 22A, pp. 2747–2759, Nov. 1991.

[11] C. Moral and A. Bautista, "Thermogravimetric Study of the Oxidation Behaviour of Sintered Stainless Steels: Powder Size and Composition," *Trans Tech Publ.*, vol. 727–728, pp. 108–113, Aug. 2012.

[12] Wilkinson, David S., *Mass Transport in Solids and Fluids*. United States of America: Cambridge University Press, 2000.

[13] D. Vivas, P. Ortiz, F. Castro, "Effect of Process Variables and Solid Gas Interactions on Microstructure of Low Chromium PM Steels," in *Quality & Inspection*, 2009, p. 7.

[14] G.F. Bocchini, B. Rivolta, G. Silva, M.G. Ienco, M.R. Pinasco, and E. Stagno, "Influence of density and surface/volume ratio on the cooling speed of sinter-hardening materials," *Adv. Powder Metall. Part. Mater.*, pp. 60–72, 2002.

[15] Scott T. Campbell, Taj Singh, and Thomas F. Stephenson, "Improved Hardenability of PM Steels Using Extra-Fine Nickel Powder," *Adv. Powder Metall. Part. Mater.*, pp. 105–115, 2004.

[16] M.W. Wu and K.S. Hwang, "Improved Homogenization of Ni in Sintered Steels through the Use of Cr-Containing Prealloyed Powders," *Metall. Mater. Trans. A*, vol. 37A, Dec. 2006.

[17] Paul G. Tallon, Dmitri V. Malakhov, and Roger Lawcock, "An Experimental Study of Size Effects in Sintering," in *Advances in Powder Metallurgy and Particulate Materials*, Las Vegas, 2017, pp. 499–514.

[18] S. Peteline, H. Mehrer, M.-L. Huang, and Y.A.Chang, "Self-Diffusion in Nickel-Manganese Alloys," *Defect Diffus. Forum*, vol. 237–240, pp. 352–357, Apr. 2005.

[19] M. Nabeel, R. Frykholm and P. Hedstro m, “Influence of alloying elements on Ni distribution in PM steels,” *Inst. Mater. Miner. Min.*, vol. 57, no. 2, pp. 111–118, 2014.

[20] George E. Dieter, *Mechanical Metallurgy*, 2nd ed. New York: McGraw-Hill book Company, 1961.

5: PM STEEL AS A METAL MATRIX COMPOSITE

5.1. Abstract

Compositional variations in admixed and sintered PM steel produce a unique system where one TTT diagram cannot predict the entire final microstructure. PM steel such as this is observed in industry, and can be created by incorporating larger Fe-particles such that less alloying constituents have a chance to fully alloy these regions. A prescribed heat treatment involving austenization and quenching will produce PM steel with islands of different microstructures: pearlitic regions and pores surrounded by a martensite matrix. This structure is characteristic of a metal matrix composite (MMC), and therefore should be treated as such. There are methods of MMC design that involve numerical methods of predicting fracture toughness. MMC methodology was used to calculate fracture toughness and compared to experimentally achieved values. Fe-C-Cr-Mn-Mo-Ni PM steel was created with ranging volume fractions of pearlitic inclusions for toughness (Tensile testing) and fracture toughness (Charpy testing) confirmation.

5.2. Introduction

MMCs are intriguing materials as they may demonstrate better mechanical properties when compared to homogenous metallic materials. Typically these materials are used in extreme situations where a low density material must be used [1]. Metal matrix composites produced by the press and sinter, or hot isostatic pressing process are common. There are made such that a ductile metallic matrix (eg. Al) is reinforced by thermally stable, stiff particles (eg. SiC). There is an extensive amount of literature regarding the properties of MMC's produced in this manner, some being found here for the reader to explore[2]–[4]. An example of the microstructure can be seen in Figure 36, where a high volume fraction of SiC is imbedded in an Al matrix.

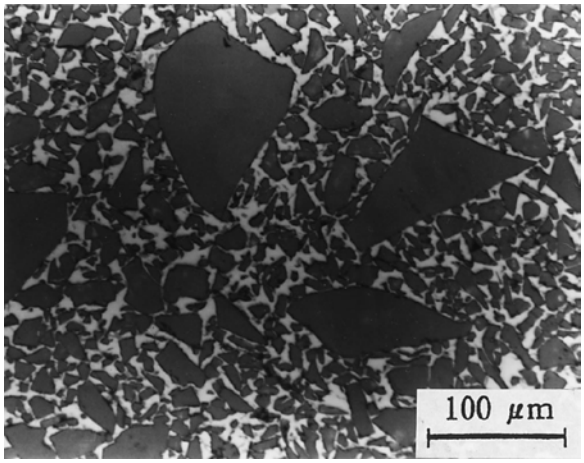

Figure 36:Squeeze casted high volume fraction SiC-Al based MMC using SiC powder with a particle size of 1 to 125 μm[3]

In the formation of PMS, by means of admixed powder blends, it is common to see large grains that were not able to become alloyed, stunting the formation of martensite. This was proven in a past study [5], as well as can be seen when looking at the initial greenbody state of the compressed admixed particles and the final microstructure in Figure 37. This is a similar structure to the traditional MMC's described above, except the matrix is stiff martensite and the inclusions are softer pearlite. It can also be seen that pores are distributed similar to imbedded particles within a matrix, except the voids that they produce do not have material properties. Even though this is a common PM steel microstructure in industry, it has not been treated as a metal matrix composite in literature.

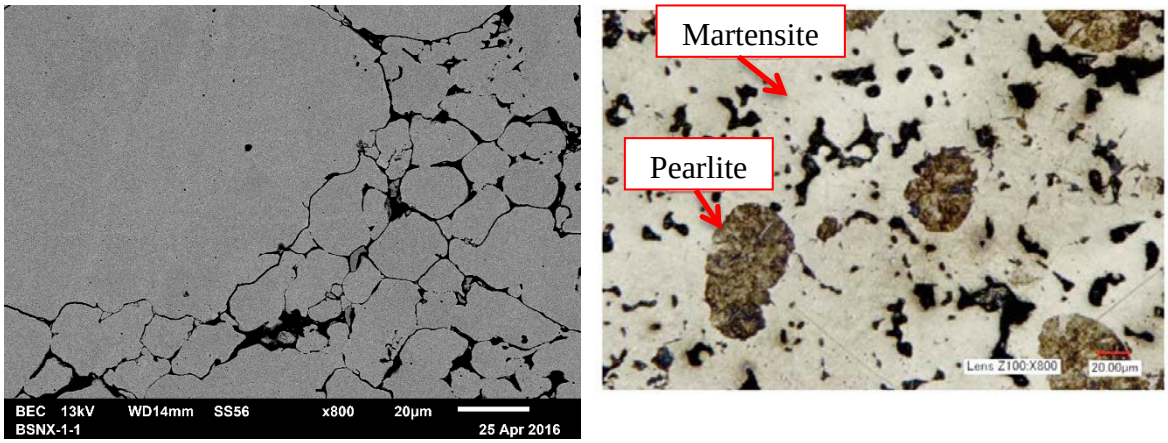

Figure 37: (left) BSE of greenbody part (right) industrially constructed microstructure after sintering, austenization and quench

If materials similar to that in Figure 37 fall into the category of MMCs, then a question arises: is there a specific volume fraction of soft particles that will enhance the mechanical properties, or for that matter, will any amount just be detrimental to the strong matrix?It should also be asked where does this material actually fit within the realm of MMCs, since this is a non-traditional MMC where the matrix is hard and brittle, and the inclusions are soft and ductile. There are three major categories for MMCs, described based on their reinforcement type: continuous fiber, short fiber and particulate MMCs [6]. There are further subcategories that become less clear in describing the multitude of structures properties and materials used [7]. The example in Figure 36 is a particulate metal matrix composite, where particles are imbedded within the matrix. The MMC produced for this study will then fall within this category.

Despite this range of MMCs if the shape of the particles are known, major mechanical properties relating to strength and toughness can be found with two pieces of information: the interfacial bond strength between particle and matrix, and the properties of the different materials [6], [8]. The properties of the individual materials can be used to approximate the bulk composite materials well. The accuracy can be increased by incorporating the interface properties, yet it is an extremely hard parameter to define, and usually requires different methods to include it.

5.3. MMC Average Deformation and Failure Mechanisms

Literature on the deformation mechanics of composites, and specifically metal matrix composites is extensive. The most common MMC is one with a ductile matrix with harder inclusions or fibers [6], [9]. It is common for these properties to be related to the imbedded particle size, shape, orientation and volume fraction. For example the SiC/Al material, shown in Figure 36, Young's modulus slightly increased with volume fraction of inclusions; particle size did not affect Young's modulus, but influenced bending strength and fracture toughness [3]. In that study the fracture behavior was related to the presence of flaws within the microstructure of the SiC. Therefore smaller particles will reduce the probability of a large flaw being present in the material, increasing the composites fracture toughness [3], [10].

Small-particle MMCs will also deform similarly to the unreinforced matrix, by material moving plastically during deformation before catastrophic failure [6]. In large particle reinforced composites, initial failure has a higher probability of originating from a particle defect [6]. It has been observed that particle cracking is an important mechanism for composite failure with particles 20 μm in size and greater [6]. Despite this probability, delamination or decohesion is one of the main mechanisms of failure when the stress surpasses the strength of the interface [9], [11]. Therefore the obvious conclusion can be made in that lower interfacial bond strength will decrease the composite strength and toughness. Figure 38 shows an FEM analysis where a composite structure with different the interface strengths, t_{c0}, was computed. It can be seen that as the interface strength increases so does the strength of the composite [11]. The simulation corresponding to a perfect adhesion at the interface was produced by using no interface elements. To produce an analysis for a debonding matrix-particle interface, the spherical reinforcements were replaced by voids [11].

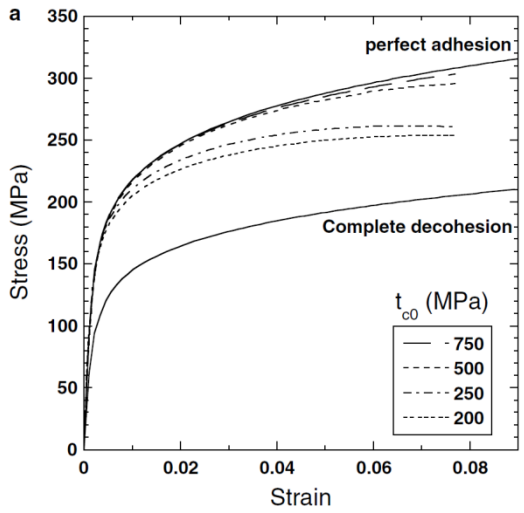

Figure 38: Interfacial strength's effect on tensile strength [11]

The properties of the matrix contribute to the composite's properties, and failure mechanisms. Kapoor and Vecchio completed a study on 6061Al that was reinforced with alumina (Al_2O_3) and mullite ($Al_6Si_2O_{13}$). The matrix was further placed under T_4 or T_6 heat treatment which showed that the bulk composite will also get stronger with the matrix. In tensile testing it was found that the matrix that was aged in the T_6 condition showed more particles cracking than in the T_4 composite. This represents that the T_4 composite failed when the ultimate strength of the matrix was reached, where in the T_6 condition the material failed from a failure in the inclusions [10]. It is also important to note that any work hardening observed during that investigation was only dependent on the matrix properties. This is consistent with most MMCs, as the metallic matrix will experience work hardening during plastic deformation, and the ceramic particles will not.

From the last study summarized it would seem that to make a metal matrix composite as strong as possible, one might try to make the metal matrix as strong as possible. This, whoever, would be wrong as that trend is not continuous. As the matrix strength increases, the potential strength increase *via* the particle reinforcements will reduce, to the eventual hindering of the overall strength[12].

5.4. Toughness

Toughness is energy a material absorbs during plastic deformation, which is commonly used in material design. The magnitude of toughness of a material is the area under the true stress strain curve, representing the energy that can be absorbed as a per unit volume of material [13]. The toughness of PM steels will increase along with the matrix or bulk properties. PMS are commonly more brittle than wrought steels due to pores, which can act as internal cracks [14] [12]. The toughness of a material is inherently related to the ability of a material to resist fracture, which is experimentally measured by the energy absorbed at fracture, observed during a Charpy testing [15].

A model for ductile fracture of MMCs was developed by Hahn and Rosenfield that has been commonly used in other literary sources shown in (13). K_{1C} is the critical stress intensity at a crack tip, or the fracture initiation toughness [12], [16], [17]. It is a function of the volume fraction, f, diameter of the particles, d, and the mechanical properties of the composite or matrix. Han and Rosenfields model, and that expressed in (14) can use mechanical properties from either the matrix, or the bulk composite. To specify the matrix material for these variables is to work under the assumption that a small plastic zone, relative to the particle spacing, is occurring. The plastic zone refers to the volume experiencing deformation before a crack tip. A small volume will not encompass a particle, and therefore will not affect the fracture. If this zone is relatively large, and encompasses the surrounding particles the composite material properties should be used.

Equation (13) assumes fracture will occur between strains of 0.02 and 0.1. It should also be noted that there are limits where the stress intensity factor can't be calculated properly. As the volume fraction, ε, decreases towards zero the fracture toughness tends to an infinitely tough material, which shows a breakdown of the model [6].

(13)
$$K_{1C} = \left[2\sigma_y E \left(\frac{\pi}{6} \right)^{1/3} d \right]^{1/2} \varepsilon^{-1/6}$$

This model assumes that crack propagation occurs by either rupture or particle-matrix separation when there is significant deformation extending the distance between unbroken particles [16]. It will therefore be seen in this investigation that the volume fraction, ε, will be that of the voids. Even though the model shown in (13) is commonly used it has accuracy within 30%, and does not fit all materials. In literature where this equation does not fit, it has been modified, for example in s study involving modeling of 7093Al/SiC MMC (14) was expressed by Majumdar and Pandey [12], [17].

In this case Hahn and Rosenfield's equation overestimated the fracture toughness so it was modified to incorporate the work hardening behavior. This was done by including the dimensionless constant d_n *and* Poission's ratio, of the matrix or composite as explained above, in the denominator. N is a function of the strain hardening coefficient: $N = 1/n$. Very specific relations for this dimensionless number d_n have been made. What is shown in (14) was tested in an FEM analysis showing good approximation for N≥0.1, yet converged to 0.66 at N=0.66 [17]. The complexity of this dimensionless fitting constant is such that an often used value from literature is 0.5. It is also interesting to note that a common value for β in literature is also 0.5 [17].

$$K_{1C} = 0.77\left[\frac{\beta\sigma_y E d}{d_n(1-\nu^2)}\right]\varepsilon^{-1/6}$$

(14)
$$d_n = 0.78 - 2.73 + 3.065N^2, N \geq 0$$
$$d_n = 0.66, N = 0$$

5.5. Controlling the Volume Fraction of Soft Islands: Powder Properties

As stated above, these soft islands are created at large Fe particles that were not fully alloyed through the sintering process. It was then pertinent to gather what sizes of large particles exist in industrially used Fe powder to create these islands. The Fe powder used at Stackpole International was subjected to a sieve analysis to build a histogram of particle sizes. This histogram can be seen in Figure 39, found in accordance with ASTM B214-16 [18].

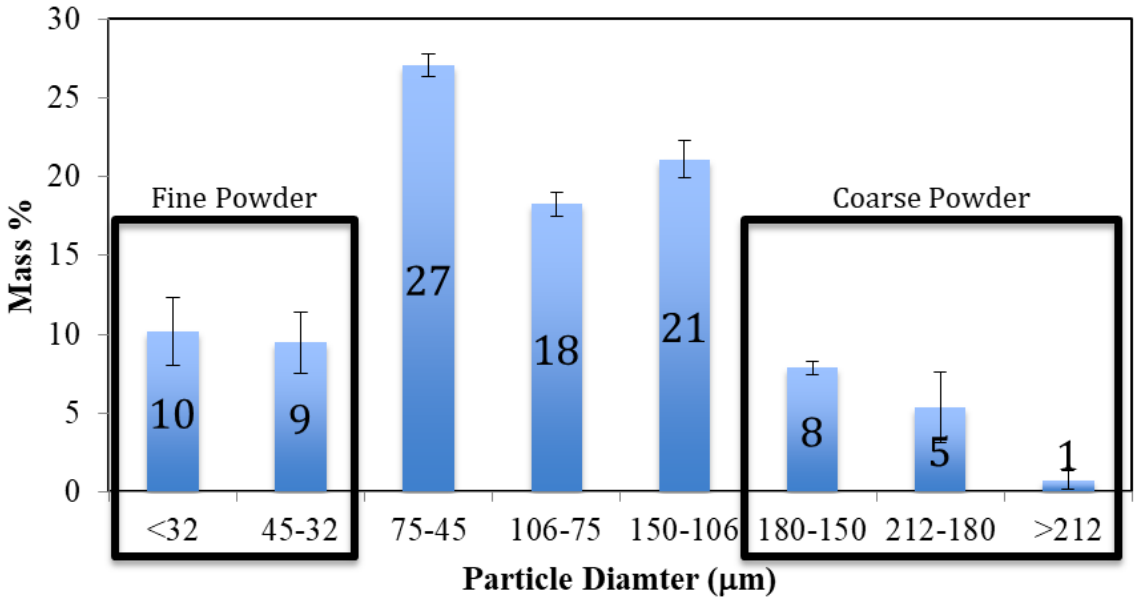

Figure 39: Size analysis of reference industrially used Fe powder via Stackpole International

Fine and coarse powders were then used in different proportions in the production of the powder blends in Table 7. Along with these powders, a reference material was manufactured with as received Fe powder. The flow-ability of each powder blend was also found by the use of ASTM B313-17 [19]. It is interesting to note that at mixtures with more than 50% of fine particles the flow-ability of the powder decreased to a point where the test could not be completed using Hall's flow meter. The use of Carney's funnel could help in this analysis due to the larger orifice of the flow meter.

The flow rates exhibited in Table 7 are indicative of typical industrial powders, as they are between 20-40s/50g [20]. It can be seen that as a greater fraction of fine particles are added a slower flow rate is observed; yet not in excess of 35s/50g where the powder could be defined as non-free flowing [20]. Flow rate of powder blends is a function related to interparticle friction, and as finer particle blends have more particle-particle interactions due to the higher surface area, the ability for powder to flow will be hindered [19].

Table 7: Sample identification with average composition and corresponding powder properties for each blend

Element	**C**	**Ni**	**Cr**	**Mn**	**Mo**
Average Wt%	0.56±0.02	0.47±0.01	0.50±0.02	0.75±0.02	0.36±0.01

Sample ID	**Mass % of Fine Fe Powder**	**Mass % of Coarse Fe Powder**	**Flow Rate (s/50g)***
0%	100	0	NA**
30%	70	30	NA**
50%	50	50	NA**
70%	30	70	30.1±0.1
100%	0	100	22.8±0.4
Reference	20	14	28.5±0.4

*Correction factor from Hall Flowmeter Funnel: 40/40.2 sec
**Powder blends could not flow through Flowmeter continuously without bridging

The apparent density is shown in Figure 40 which was found in accordance with ASTM B212-17. The particle size distribution and corresponding histogram is shown to have an effect on the apparent density of the powder blends [21]. It can be seen that specific volume fractions of coarse and fine particles can increase or decrease the apparent density. The 100% blend, where only course particles of Fe were used has the lowest apparent density. It is known that mono-sized particles do not generate a high packing factor of powders [22], yet there is a clear difference between 100% coarse particles and 100% fine particles. The particle shape is also an important powder characteristic which apparent density depends on. The large particles are less spherical, and more oblong, which decreases the apparent density by shelves and cavities being created by interlocking particles. This can be seen in Figure 41 comparing large Fe particles to fine observed through a stereoscope.

A high packing factor will occur when there is a specific ratio of larger and smaller particles that fill the spaces created by the former [22]. Mathematicians have payed particular attention to this, where depending on the size of the particles specific smaller sizes can best fill the gaps created between them. This is not a central topic of discussion for this manuscript, yet of the reader wishes to expand their understanding of this issue some literature is available [23]–[25].

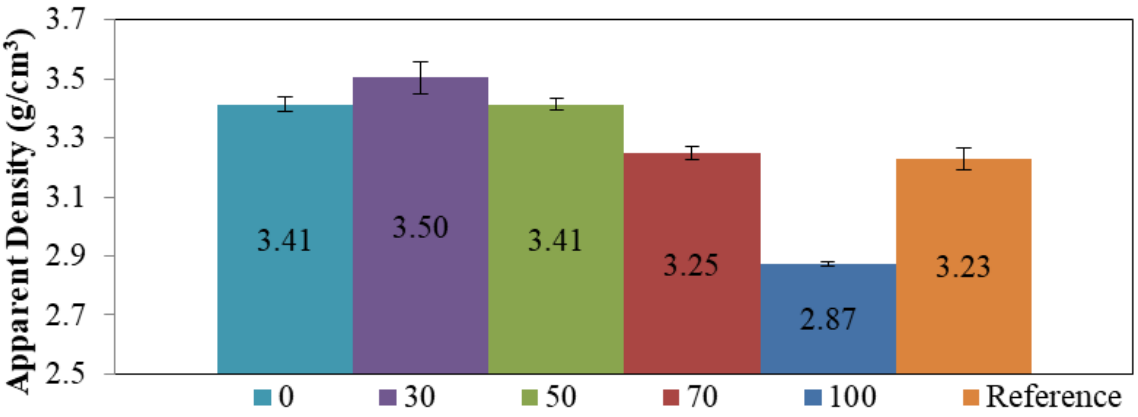

Figure 40: Apparent density of powder blends

Fine Fe particles

Coarse Fe Particles

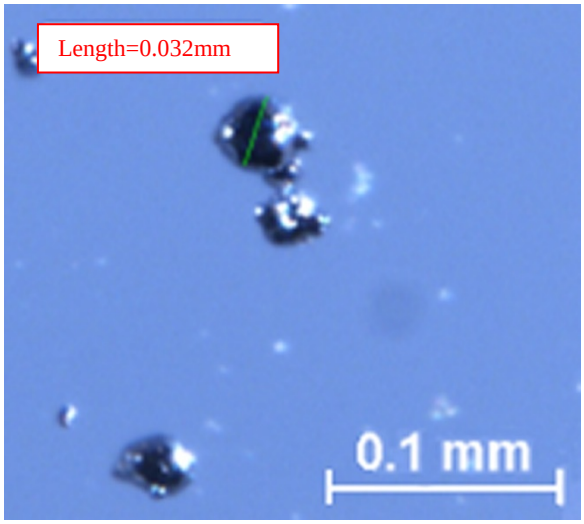

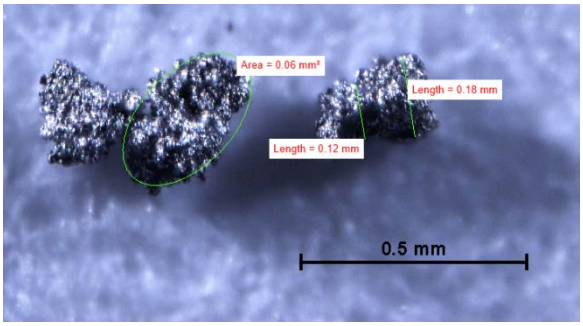

Figure 41: Comparison of fine and coarse Fe particles, showing the difference in shape

Figure 42 shows the difference in compressibility of the powder blends, and how decreasing the amount of large particles, increases the pressure needed to reach the green density of 7.0g/cm^3. Reference, 70% and 50% blends required 400-425Mpa of pressure to produced 7.0g/cm^3. The 0% and 30% blends are different in that 450-470Mpa was needed to reach 7.0g/cm^3. There are three stages to powder compaction: initial stage involving

particle rearrangement followed by stage 2 where there is elastic deformation and particle sliding. Stage three occurs when the interlocking particles begin to plastically deform and interlock [26]. The softer the material, the more plastic deformation and therefore a higher green density will be easier to reach. Comparing the 100% blend, where lower pressures resulted in higher greenbody densities it can be seen how larger particles are more compressible. The stacking of data points also shows the slight variance in the production of greenbody parts. Smaller particles will impede compaction due to more interparticle friction a higher work hardening rate [20]. It was also found that in comparing spherical and spongy (rough surface and oblong shape) Fe powder that the sponge Fe was more compressible due to its higher capability for plastic deformation [26].

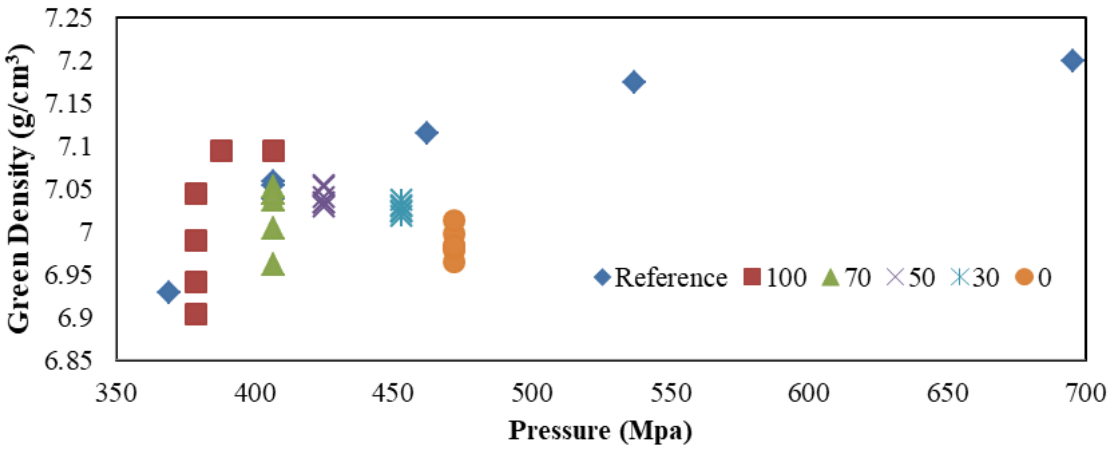

Figure 42: Compressibility of powder blends in an effort to reach 7.0g/cm^3

The blends were then compacted into 1cm x 1cm x 7.5cm impact bars and sintered in an industrial furnace at 1280°C for 30 minutes in a protective atmosphere. As can be seen in Figure 43, the sintered densities are very similar. There is a slight difference in comparing the 0-50% blends in that they reached a higher density than the other blends. This is most likely due to a higher magnitude of densification being caused by the higher amount of fine powder in the blends and increase in compacting pressure used in forming the greenbody. Densification is increased along with an increase in particle surface are in the greenbody. As the particles decrease in size the surface area will increase which will

increase the magnitude and rate of densification. A higher initial pressure has also observed being a cause for more densification [20], [27], [28], [29]. For more factors that affect the densification rate and magnitude refer to the appendix.

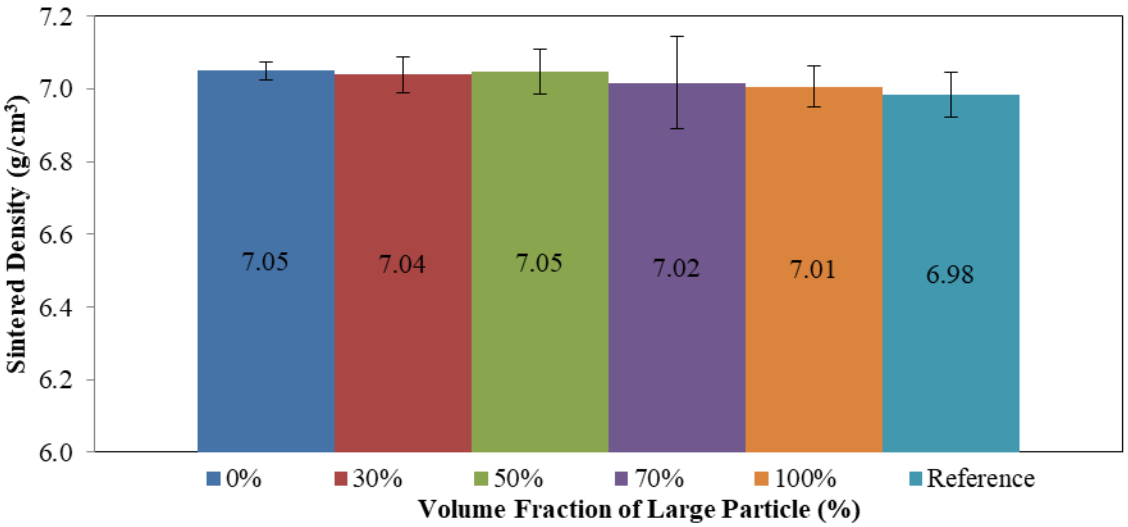

Figure 43: Sintered Density of Powder Blends after Industrially Sintering for 30 minutes at High Temperatures

5.6. Optical Microscopy

The steel was austenized at 900ºC and quenched in helium at 20atm to form a martensitic matrix surrounding incompletely alloyed, softer islands. In completing microhardness indents ion the soft islands, as well as micrographs the softer islands particles of fine pearlite and/or upper bainite. This can be seen in the following micrographs, as well as in comparing the average hardness Vickers of the islands (357±11HV) to Table 8. This data was found experimentally in a study on admixed Distaloy HP1: 4.38wt% Ni, 2.08wt% Cu, 1.5wt%Mo and 0.7wt% graphite admixed [30].

Table 8: Hardness Vickers phase analysis on Distaloy HP1 PMS at 7.0 and 6.8g/cm^3 [30]

Density g/cm^3	Martensite (HV)	Lower bainite (HV)	Upper bainite (HV)	Transforming Aust (HV)	Fine Pearlite (HV)	Residual Austenite (HV)
7.0	720-775	697	317-400	307-595	317-401	200-230
6.8	725-750	628	310-381	380-680	310-381	137-231

It is also apparent that the sizes of the particles are roughly the same, yet the number density (#/mm^2) directly increases with the increase of large Fe particles added to the powder blend. There is a common trend in the boarders of the soft islands. Instead of a gradual change of microstructure, there is a noticeable boarder. During quenching the unalloyed sections of the material would not be able to stabilize the austenitic phase as the surrounding alloyed steel, and therefore fine pearlite and/or upper bainite would seed and spread outward as if moving up the concentration gradient until the Ms temperature was reached for the surrounding area, stopping the growth of the diffusional phase. This morphology can further explain the potential concentration gradient of the alloying elements within this material.

The microstructures and pore morphology of the 7 blends can be seen in Figure 44. Even though the volume fraction of pores is similar in all the material, approximately 10%, a difference in pore morphology is noticeable. The 0% coupon has finer and more round pore structure, where the 100% blend shows larger porosity, this is shown quantitatively in Table 9. The other coupons have a very similar pore structure with the reference material, showing that moderate changes in the distribution of Fe powder do not drastically change pore geometry after sintering.

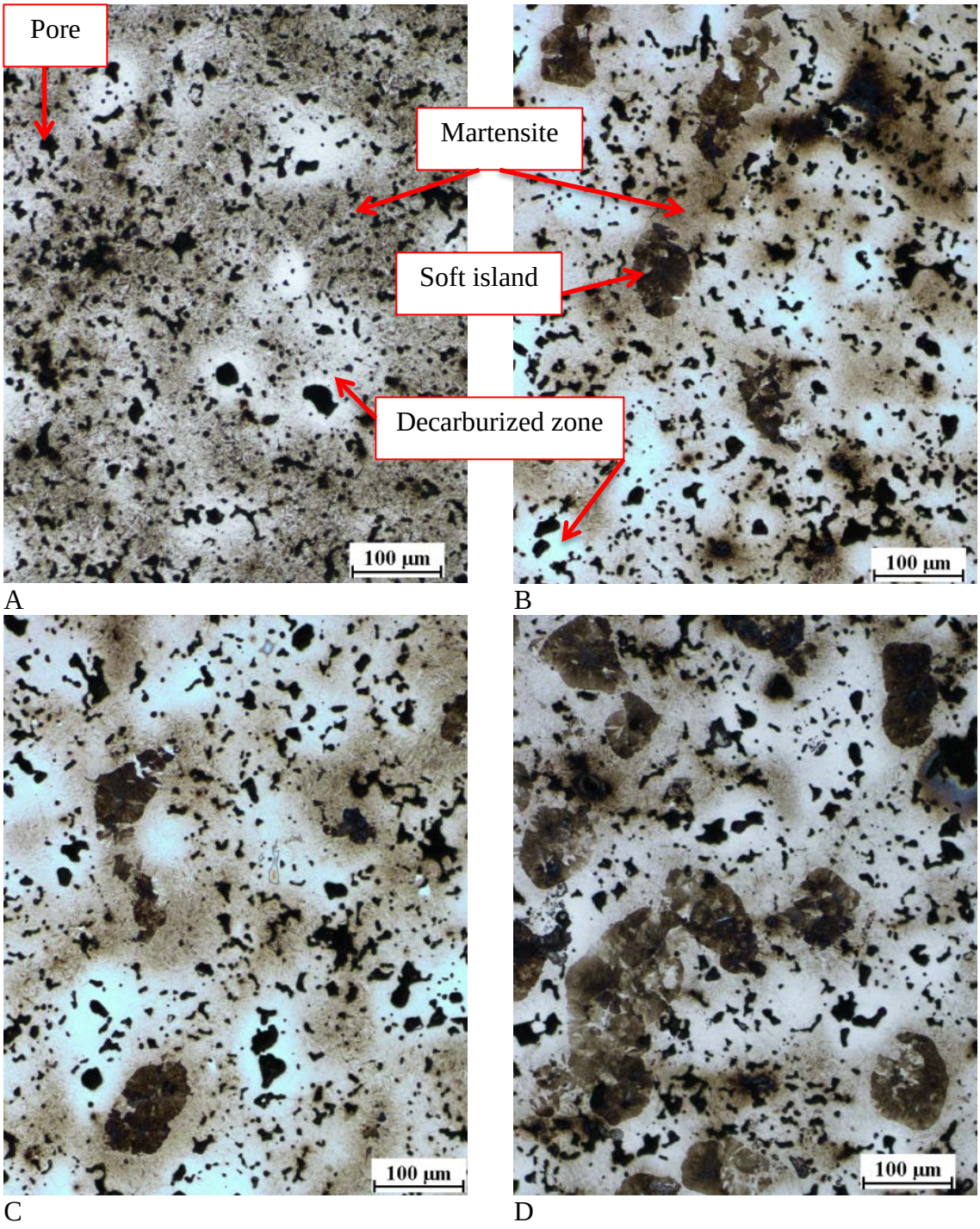
Pore
Martensite
Soft island
Decarburized zone
100 μm
100 μm
100 μm
100 μm

A B

C D

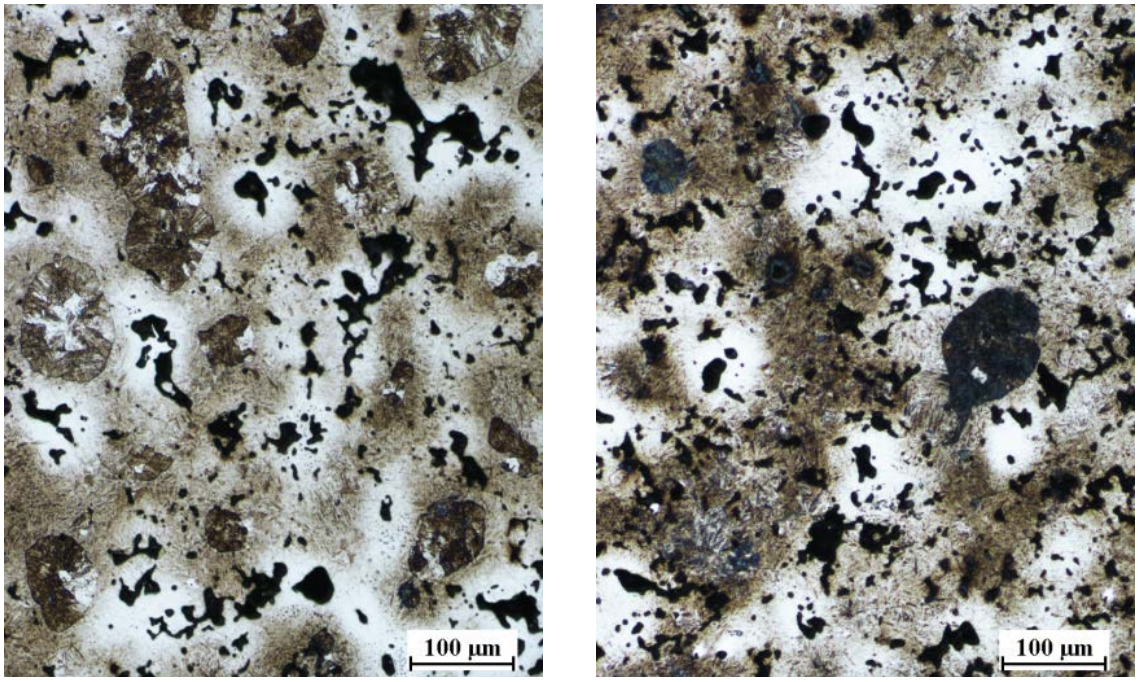

E F

Figure 44: Optical microscopy of MMC coupons etched with 2%nital, showing A) 0% B) 30% C) 50% D) 70% E) 100% of large particles and F) Reference Fe powder used

The micrographs in Figure 44 also show a lighter region surrounding pores. It can be speculated that retained austenite exists in these bright zones from greater amounts of alloying elements. An XRD analysis was completed, results in Table 9, which show a small amount of retained austenite. Yet, it is reasonable that these areas hold lower concentrations of carbon *via* decarburization from the sintering process. It is known that at 7.0g/cm^3 pore are interconnected, consequently an extent of decarburization may be significantly large, extending millimetres into the steel [31]. 2%nital was used as an etchant, which will reveal martensite, pearlite and ferrite grain boundaries. Nital is also known to darken martensite with higher carbon concentrations, relative to steel with lower concentrations. This can be seen in the micrographs as the lighter regions around the pores. This is further proven by a slight decrease in hardness found via microhardness indentions seen in Figure 45.

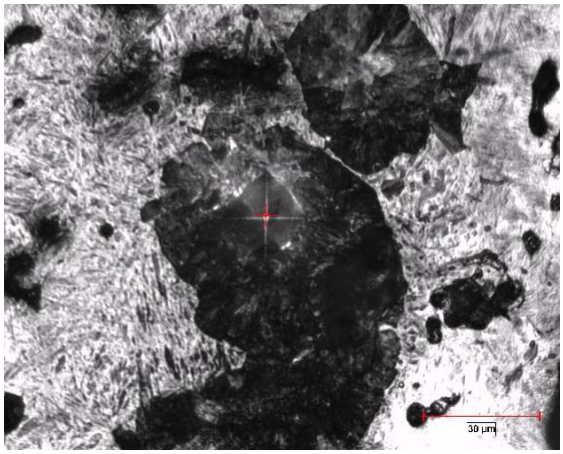

A

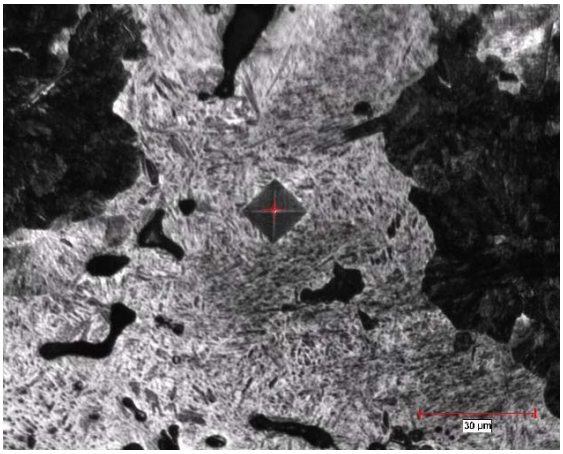

B

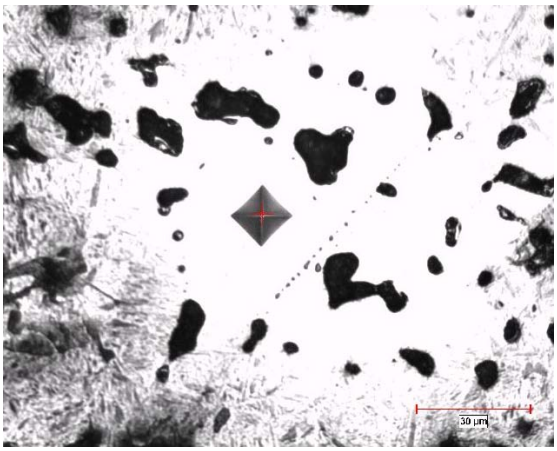

C

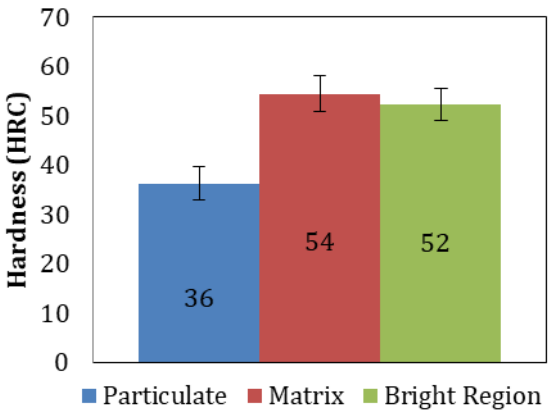

D

Figure 45:Microhardness Indentations to (A) Soft Particulate (B) Martensitic Matrix (C) Bright Region (D) Hardness summary of Regions

The microhardness measurements of the different areas seen in the morphology can also be seen in Figure 45. The dark islands are softer than the other phases within the material. The bright area seen is martensite, yet most likely was affected by decarburization during the sintering process.

It is known that carbon content can be directly related to martensite hardness, and a difference on 0.1wt% can have a change of hardness of 2-3 HRC depending on the carbon concentrations which can be seen in Figure 46 [32]. The lines drawn are representational of the bulk carbon content compared to the measured hardness of the bright regions

showing a potential 0.05wt% decrease within the bright areas; via industry knowledge of the sintering process at Stackpole, 0.1wt% carbon is lost during the sintering process.

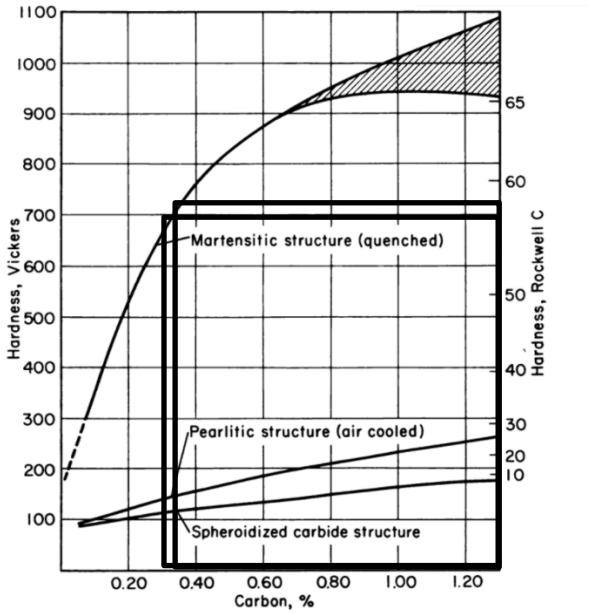

Figure 46:Hardness of martensire as a function of Carbon content [32]

5.7. Mechanical Properties

Figure 47 shows the apparent hardness of the sintered and heat-treated PM steel. Without any unalloyed large particles and smaller pores the apparent hardness for the 0% material is highest. The 30%-50% PM steel blends show a similar hardness, even though they are more unalloyed regions producing softer islands. With more than 50% large particles added the hardness drastically decreases, and is comparable to the reference Fe blend used. This threshold can be used in choosing Fe powder from distributers, in that a base Fe powder used for admixed blending will perform optimally with 50% or less of Fe powder greater than 150μm in diameter if mixed with 50% fine powder.

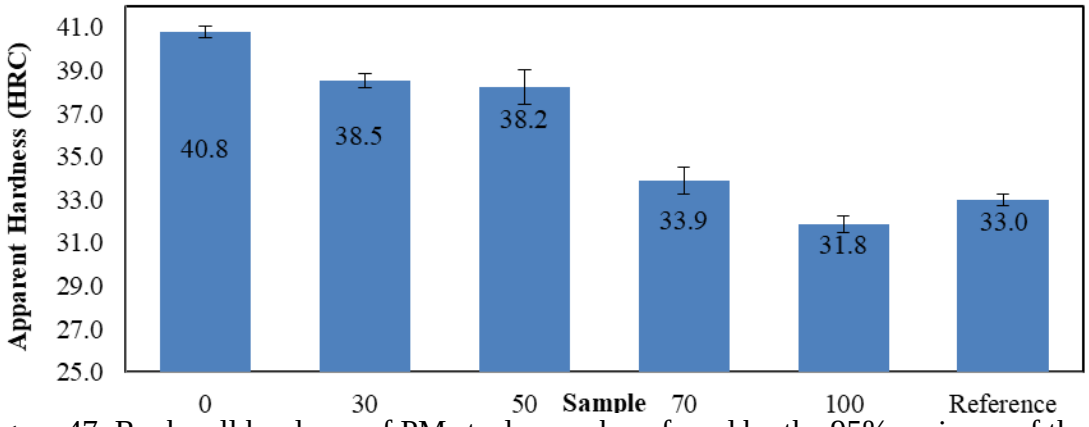

Figure 47: Rockwell hardness of PM steel, error bars found by the 95% variance of the mean from no less than 70 tests per sample

Table 9 shows the particles/mm^2, which was found by using multiple micrographs and averaging the amount seen over the area photographed. The retained austenite (RA) was found via XRD analysis, which has been shown to occur in PM steel due to the incomplete homogenization of alloying elements, specifically Ni [33]. The differences in RA are moderate, it is therefore inappropriate to make conclusions as to its effect on the hardness; other than stating it is softer than martensite.

The average major and minor diameters are an expression of size of the soft island's via elliptical measurements. There is a large jump in size for the 100% powder blend from the other samples, yet it can be seen that the aspect ratio (Major/Minor) is very similar. This intrinsically makes sense due to the smaller packing factor of mono-sized powder blends and easy deformed large Fe particles [23]. It is important to note that all blends almost have the same volume fraction of pores, and therefore this difference in size must be correlated with the initial size and shape of the Fe particles.

Table 9: Summary of pore geometry and percent of retained austenite found after sintering and heat treatment

Sample	0	30	50	70	100	Reference
Unalloyed Particles/mm^2	0.0±0.0	5.8±1.2	9.7±1.1	17.7±4.3	23.9±6.3	10.1±4.5
% Austenite-XRD	6.1	4.5	2.7	8.7	7.1	4.7
Average Major Diameter (μm)	24.4±0.9	25.9±2.3	23.8±1.6	27.9±4.7	34.0±2.5	28.6±1.3
Average Minor Diameter (μm	12.5±0.5	13.3±1.1	12.6±1.0	14.7±1.9	16.9±1.3	14.6±0.6
Aspect Ratio (μm)	2.0±0.1	1.9±0.2	1.9±0.2	1.9±0.4	2.0±0.2	2.0±0.1

The blends were machined into tensile samples and tested[4]. At least three samples for each blend were used to ensure reproducibility; the results of the engineering stress/strain data can be seen in Figure 48. The curves are typical for brittle martensite, where little to no necking occurred before fracture. In this case, such behavior is caused by the significant fraction of untempered martensite and the crack initiation zones from pores. This small amount of plastic deformation, and no necking means that the UTS and rupture strength coincide [34].

The untempered martensitic matrix is stiff and brittle and surrounds the pores. Therefore during the applied tensile stress the internal stress located at the pores cannot be relieved via plastic deformation. They will therefore act as an internal crack, or stress concentrator. Therefore final failure occurred when the internal stress reached the critical fracture stress of this region. This morphology is seen in all material samples. This is potentially a reason why the curves are very similar, since increasing the volume fraction of soft particles will occur away from the pores.

[4] The tensile test samples were manufactured and testes by Exova Inc.

The differences do express the interplay between microstructure and pore characteristics. This similar circumstance has been seen in the fracture mechanics of austenized and quenched compared to as-sintered PM steels [14]. It can therefore be speculated that any addition of unalloyed particles will decrease the UTS. This is further shown in Table 10 expressing the yield strength. This coincides with what was stated earlier, that as the strength of the matrix increases, additions of particle reinforcements will hinder the overall strength [12].

Table 10: Average 0.2% offset yield strength with errors found by a 95% confidence interval of the mean

Sample	0	30	50	70	100	Reference
0.2% Offset Yield Strength (MPa)	1140.00 ±127.06	1086.67 ±117.40	991.67 ±132.81	925.00 ±56.92	810.00 ±190.59	983.33 ±7.17

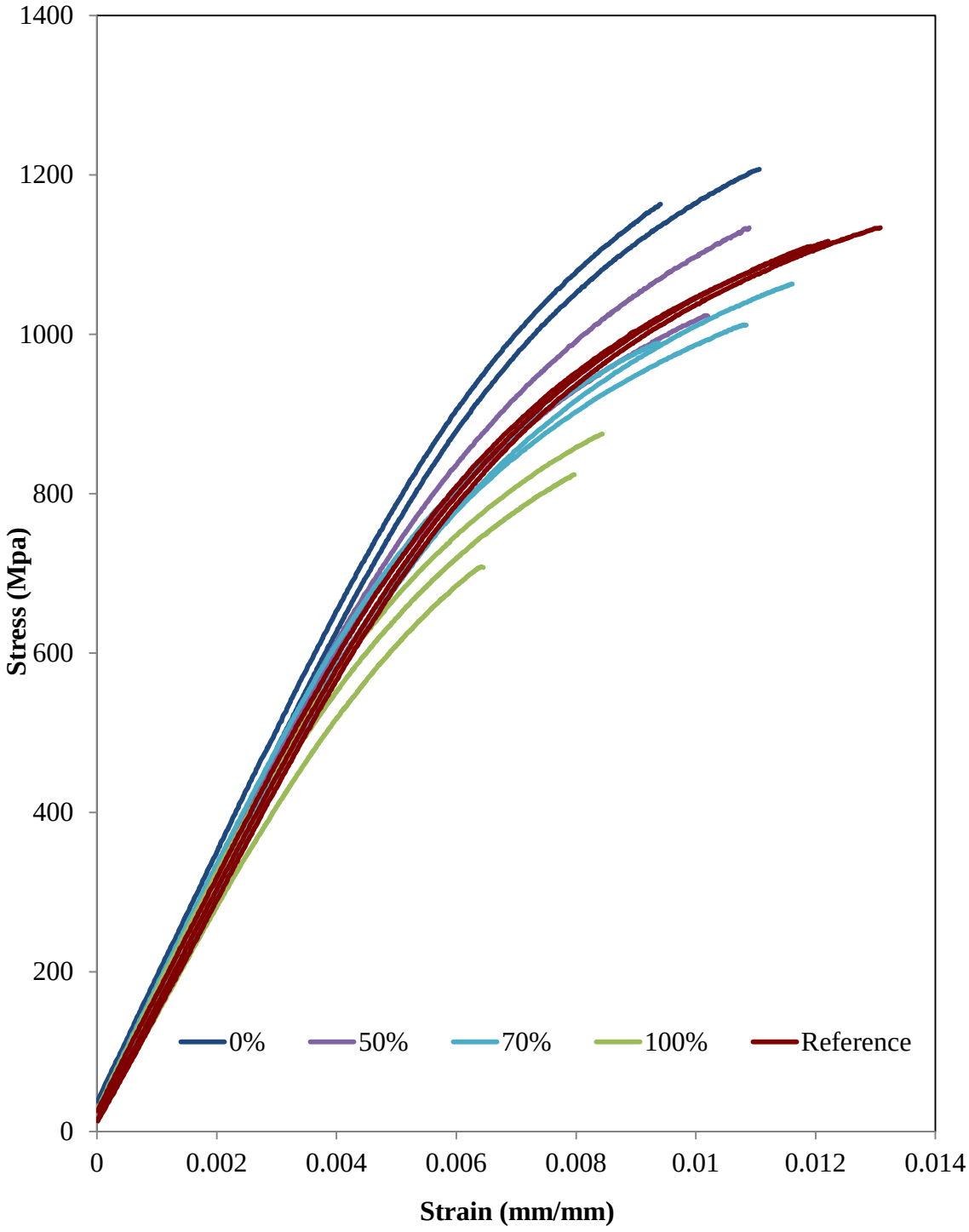

Figure 48: Engineering stress strain relationship missing data as well as 30% samples broke outside of gauge length

5.8. Toughness

The toughness was found via the trapezoid method in taking the integral under the true stress-strain curve, shown in Figure 49. The gap shown in the data represents the failed test specimens that failed outside the gauge length. The fracture toughness of the 100% specimen shows a similar trend to the hardness data in Figure 47. The larger size, and less circular shaped pores in the 100% sample, along with the decrease of the fraction of martensite, reduced the overall strength of the steel. It can also be seen in Figure 49 that the reference steel is the toughest material. This is a result of the higher strain the reference material reached before fracture. To fully understand how the differences in microstructure relate to this more valid data should be collected. Unfortunately during testing improper surface finishing resulted in unusable data. As well as the material being so brittle might have masked some information regarding the tensile properties of soft islands.

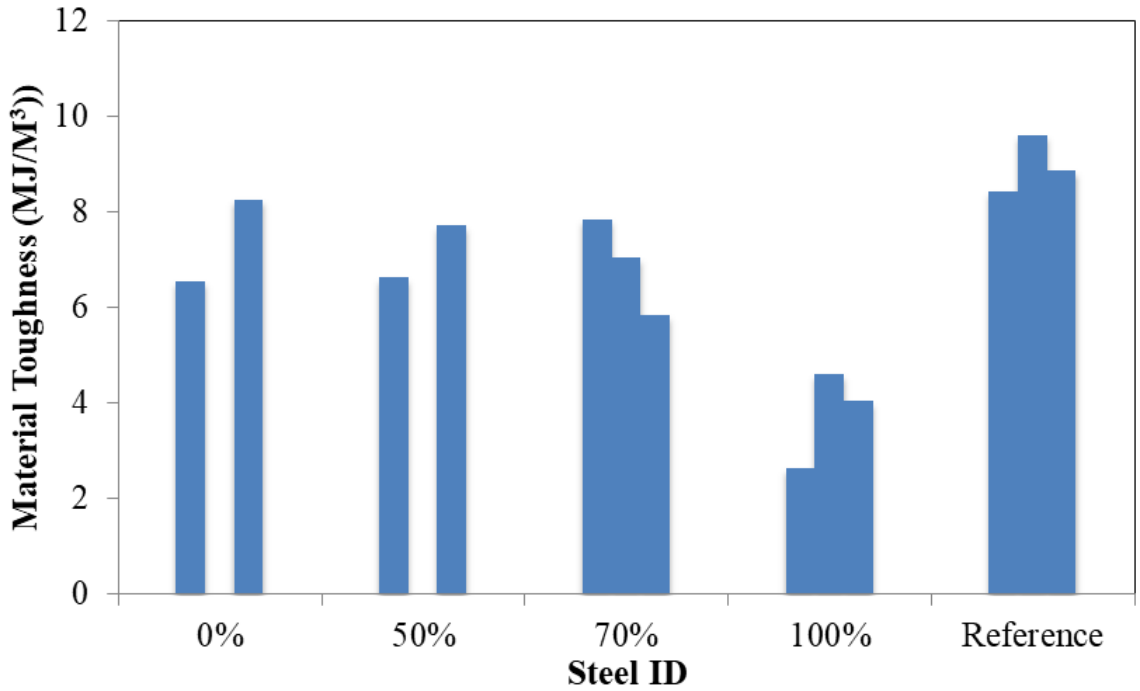

Figure 49: Toughness found by taking the integral under the true stress strain curve, data from invalid tensile failure outside of gauge length is not shown

5.9. MMC Fracture Toughness

The Charpy test was completed on all six materials and showed a constant fracture toughness of 12 Nm, corresponding to an extremely brittle material. This is most likely due to the hard matrix, surrounding porosity and therefore the material not being able to relive the stresses through yielding and fracture occurred at the critical conditions where the pores acted as internal cracks.

Figure 49 is informative as to the material properties of toughness, yet cannot be used to directly compare to matrix computations of fracture toughness since K_{1C} is a representation of fracture toughness via the first mode of fracture from an internal flaw. The first mode of fracture is from tensile stresses acting normal to a plane of a crack, opening it.

Fracture toughness was found by the methods outlined in by Han and Rosenfields, And Majumdar and Pandey reiterated in (15) and (16) respectively for the reader.

(15)
$$K_{1C} = \left[2\sigma_y E \left(\frac{\pi}{6} \right)^{1/3} d \right]^{1/2} f^{-1/6}$$

(16)
$$K_{1C} = 0.77 \left[\frac{\beta \sigma_y E d}{d_n (1-\nu^2)} \right] f^{-1/6}$$
$$d_n = 0.5$$
$$\beta = 0.5$$

The K_{1C} values can be seen in Figure 50. Han and Rosenfields express an overestimation as to what is expected to see when comparing to known wrought steels. For example the low alloy steel D6AC has a similar composition with K_{1C} values ranging from 40 – 115Mpam$^{1/2}$ with a crack of similar size to the pores[35]. These discrepancies could be for many reasons. The first model assumes fracture will occur between strains of 0.02 and

0.1, and since this material was very brittle, only a maximum strain of 0.013 was found for one of the reference blends. As specified, both models can use mechanical properties from either the matrix, or the bulk composites depending on the plastic zone. If the assumption is correct that the final failure occurred within the matrix, at a pore tip the matrix properties should be used. This was completed and the results were extremely inflated[5].

The composite mechanical properties found from the tensile test were used in (15) and (16) to produce Figure 50. Using this information could lead to another potential error, where the elastic modulus from this experiment is an approximation since only very fine strains can properly produce this number experimentally [13]. These calculations are also known to generate an estimation that is of the correct magnitude, yet potentially incorrect for certain volume fractions [6]. The use of the work hardening exponent in (16) generates a more realistic model, which was expected via literature.

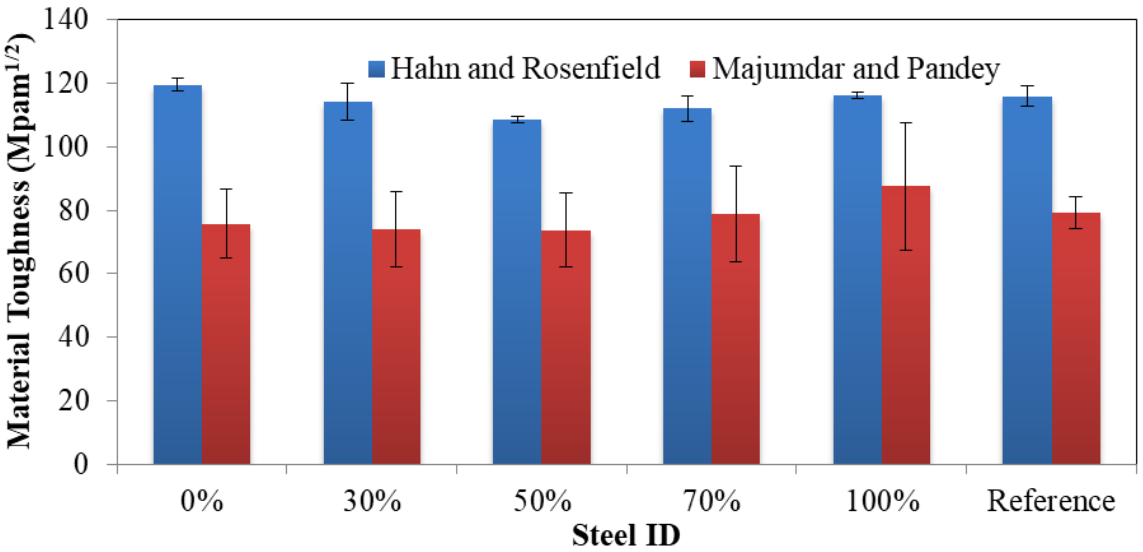

Figure 50: Comparison of two MMC fracture toughness models representing the tensile samples made for this project

5.10. Conclusion

[5] For the methodology of how this was done refer to the appendix

The production of non-traditional metal matrix composites via controlling the initial size distribution of iron powder was completed and tested. It was found that by incorporating softer particles into a strong matrix the bulk material properties will decrease. This decrease was not overly prevalent in small amounts of soft islands. This proved that an admixed powder blend made with no more than 50% large iron particles can perform closely to complete martensitic PM steel made from only fine Fe powder in hardness testing. This information has a practical importance to PMS manufactures. The histogram of an Fe powder can be a clear indication of how it will perform when alloyed. It also represents how increasing the volume fraction of smaller particles will increase the hardness and tensile properties.

This, however, is in conflict with the toughness data found by the area under the true stress/strain curves. Here the reference material performed the best, where the increase in elongation outweighed the increase in UTS of the other materials. To completely justify these claims, more experimental information must be found and statistically verified.

The fracture toughness calculations for metal matrix composites, applied to this study showed inflated values, yet a good approximation to literature. Unfortunately, the potential errors means further experimental data should be collected and compared to make a concrete statement. Furthermore a recommendation of producing more tempered, less brittle matrix for future studies.

5.11. References

[1] S.Ho and E.J. Lavernia, “Thermal Residual Stresses in Metal Matrix Composites: A Review,” *Appl. Compos. Mater.*, vol. 2, pp. 1–30, 1995.

[2] M.J. Tan, L.H. Koh, K.A. Khor, and F.Y.C. Boey, “Discontinuous reinforcements in extruded aluminium-lithium matrix composites,” *J. Mater. Process. Technol.*, vol. 37, pp. 391–403, 1993.

[3] Chang-You Chen and Chuen-Guang Chao, “Effect of Particle-Size Distribution on the Properties of High- Volume-Fraction SiCp-Al–Based Composites,” *Metall. Trans. A*, vol. 31A, Sep. 2000.

[4] Dr. E.A. Bloch, “Dispersion-Strengthened Aluminum Alloys,” *Metall. Rev.*, vol. 6, no. 22, 1961.

[5] Paul G. Tallon, Dmitri V. Malakhov, and Roger Lawcock, “An Experimental Study of Size Effects in Sintering,” in *Advances in Powder Metallurgy and Particulate Materials*, Las Vegas, 2017, pp. 499–514.

[6] T. W. Clyne and P. J. Withers, *An Introduction to Metal Matrix Composites*. Cambridge University Press, 1995.

[7] D.B. Miracle, “Metal matrix composites – From science to technological significance,” *Compos. Sci. Technol.*, vol. 65, pp. 2526–2540, 2005.

[8] Z. Hashin, “Analysis of Composite Materials — A Survey,” *J. Appl. Mech.*, no. 50, pp. 481–505, Sep. 1983.

[9] D. Hull and T.W. Clyne, *An Introduction to Composite Materials*, 2nd ed. Cambridge University Press, 1996.

[10] Rajeev Kapoor and Kenneth S. Vecchio, “Deformation behavior and failure mechanisms in particulate reinforced 6061 Al metal-matrix composites,” *Mater. Sci. Eng.*, vol. A202, pp. 63–75, 1995.

[11] Javier Segurado and Javier LLorca, “A computational micromechanics study of the effect of interface decohesion on the mechanical behavior of composites,” *Acta Mater.*, vol. 53, pp. 4931–4942, 2005.

[12] I. Sabirov and O. Kolednik, “Local and global measures of the fracture toughness of metal matrix composites,” *Mater. Sci. Eng.*, vol. A 527, pp. 3100–3110, 2010.

[13] George E. Dieter, *Mechanical Metallurgy*, 2nd ed. New York: McGraw-Hill book Company, 1961.

[14] G. Straffelini, C. Menapace, and A. Molinari, “Interpretation of effect of matrix hardening on tensile and impact strength of sintered steels,” *Powder Metall.*, vol. 45, no. 2, pp. 167–172, 2002.

[15] ASTM International, “Standard test Methods and Definitions for Mechanical Testing of Steel Products.” ASTM International, , 100 Barr Harbor Drive, PO Box C700, West Conshohocken, PA.

[16] G.T. Hahn and A.R. Rosenfield, “Metallurgical Factors Affecting FractureToughnessof AluminumAlloys,” *Metall. Trans. A*, vol. 6A, pp. 653–668, Apr. 1975.

[17] B.S. Majumdar and A.B. Pandey, “Deformation and Fracture of a Particle-Reinforced Aluminum Alloy Composite: Part II. Modeling,” *Metall. Mater. Trans. A*, vol. 31A, pp. 937–950, Mar. 2000.

[18] ASTM International, “Standard Test Method for Sieve Analysis of Metal Powders.” ASTM International, West Conshohocken, PA, 2016.

[19] ASTM International, “Standard Test Methods for Flow Rate of Metal Powders Using the Hall Flowmeter Funnel.” ASTM International, , 100 Barr Harbor Drive, PO Box C700, West Conshohocken, PA, 2017.

[20] Andre Salak, *Ferrous Powder Metallurgy*. 7 Meadow Walk, Great Abington, Cambridge CB1 6AZ, England: Cambridge International Science Publishing, 1995.

[21] ASTM International, “Standard Test Method for Apparent Density of Free-Flowing Metal Powders Using the Hall Flowmeter Funnel.” ASTM International, West Conshohocken, PA, 2013.

[22] Xiaolin Chen, “Particle Packing, Compaction and Sintering in Powder Metallurgy,” for the Degree of DOCTOR OF PHILOSOPHY, University of Alberta, Edmonton, Alberta, Canada, 1998.

[23] H. J. H. Brouwers, “Particle-size distribution and packing fraction of geometric random packings,” *Phys. Rev. E*, vol. 74, no. 031309, pp. 1–14, Sep. 2006.

[24] A.B. Yu, J. Bridgwater, and A. Burbidge, “On Modelling of Packing of Fine Particles,” *Powder Technol.*, vol. 92, pp. 185–194, 1997.

[25] A. B. Yu and N. Standish, “An Analytical-Parametric Theory of the Random Packing of Particles,” *Powder Technol.*, vol. 55, pp. 171–186, 1988.

[26] D. Poquillon, J. Lemaitre, V. Baco-Carles, Ph. Tailhades, and J. Lacaze, “Compaction of iron powders—relations between powder morphology and mechanical

properties Part I: Powder preparation and compaction," *Powder Technol.*, vol. 126, pp. 65–74, 2002.

[27] Q.H. Zou, H. M. Zhao, D.Y. Zhang, M. Geng, Z.G. Wang, J.J. Lu, "Thermophysics characteristics and densification of powder metallurgy composites," *Powder Metall.*, vol. 49, no. 2, pp. 183–188, 2006.

[28] Kishor M.Kulkarni, "Effect of Particle Size and shape on Sintering of high Speed Steels," *Mod. Dev. Powder Metall.*, vol. 19, 1988.

[29] P. R. Kalischer, "The Effect of Particle Size on the Shrinkage of Metal Compacts," *Symp. Powder Metall. Am. Soc. Test. Mater.*, pp. 31–40, Mar. 1943.

[30] G.F. Bocchini, B. Rivolta, G. Silva, M.G. Ienco, M.R. Pinasco, and E. Stagno, "Influence of density and surface/volume ratio on the cooling speed of sinter-hardening materials," *Adv. Powder Metall. Part. Mater.*, pp. 60–72, 2002.

[31] ASM International, *Powder Metal Technologies and Applications.pdf*, 10th ed., vol. 07. ASM International, 1998.

[32] Edgar C. Bain and Harold W. Paxton, *Alloying elements in steel*, 2nd ed. Metals Park, Ohio: American Society for Metals.

[33] Scott T. Campbell, Taj Singh, and Thomas F. Stephenson, "Improved Hardenability of PM Steels Using Extra-Fine Nickel Powder," *Adv. Powder Metall. Part. Mater.*, pp. 105–115, 2004.

[34] Seibert Fairman and Chester S Cutshall, *Mechanics of Materials*. John Wiley & Sons, Inc., 1953.

[35] William T. Matthews, "Plane Strain Fracture Toughness (K1C) Data Handbook for Metals," Army Materials and Mechanics Resevrch Center, Watertown, Mwassachusetts 02172 AM)M4R-TM, AMMRC MS 73-6, Dec. 1973.

6: SUMMARY AND SUGGESTED FUTURE WORK

6.1. Summary

The work is presented in the form of a series of three technical articles that explain the foundational understandings of the hardenability of PM steel, related to porosity and homogenization of alloying constituents. The limits to non-desirable phases in efforts to optimize mechanical properties is also represented in a novel relation to metal matrix composites. The findings from this research are summarized by the following.

1. An Experimental Study on the Influence of Porosity on Hardenability
    a. The effect of porosity on the formation of martensite was observed
    b. A large increase of porosity hinders the formation of martensite
    c. Considering the slight difference in thermal conductivity it is reasonable to contribute this difference too more than just the heat extraction
    d. There is a critical density between $6.8 g/cm^3$ and $7.3 g/cm^3$ where martensite formation is hindered
    e. Further work is needed to produce a porosity-multiplying factor to compute a *DI* related to the density
2. Base Powders' Sizes Effect on Sintering and Hardenability
    a. The effect of different initial sized particles on the formation of martensite was observed
    b. Fine powder produces a more homogenous mixture of alloying elements, allowing for a great fraction of martensite to form

c. Large Fe particles are not only detrimental on their own, but when mixed with other sizes

3. PM Steel as a Metal Matrix Composite
    a. The production of non-traditional metal matrix composites via controlling the initial size distribution of iron powder was completed and tested
    b. Incorporating softer particles into a strong matrix the bulk tensile and hardness properties will decrease
    c. It was found that the threshold for large particles is between 50%-70% will dramatically decrease the hardness of the material
    d. Further efforts will be needed to understand how material toughness is affected by soft islands due to
        i. inappropriate amount of data to make statistical conclusions
        ii. brittle matrix material made the material fracture before significant plastic deformation, where the soft islands should have been able to increase toughness
    e. Fracture toughness composite theories do not fully represent a brittle PM steel material

7: APPENDICES

7.1. The Determination of Basic Properties and Production of PM Steel Samples

The production of PM specimens were completed under the guidance and expertise of Stackpole International, and confirmed along with ASTM and MPIF standards. The following is the methodology of producing samples and testing the basic properties of the powder, greenbody and final sintered samples.

7.1.1. Sieving – Size Analysis

The Fe powder used in the production of test bars for *The Size Effect of the Base Powder on the Hardenability*, and *PM Steel as a Metal Matrix Composite* went through the method outlined in ASTMB214-16 [1]. The sieve shakers at Stackpole and McMaster University were used by first placing the standard sieves of desired fractions in highest to lowest as shown in Figure 51, where the top is covered by the shaker lid, and a pan at the bottom. The machine was then run for 10-15 minutes after placing between 90-110g of powder in the top sieve. The Ro-Tap shake shown uses axial and rotating movement to uniformly shake material through decreasing sized sieves to separate specific particle sizes. After this the powder was taken out of the individual sieves and weighed to produce a mass histogram of powder sizes. In cleaning the sieves it is also important not to use compressed air, since this could further imbed a stuck particle, or rupture the sieve by pushing it through [1].

Figure 51: Ro-Tap sieve shaker at McMaster University

7.1.2. Alloy Constituent Target Acquisition and Confirmation

In producing appropriate mixes of ferroalloy and elemental powders mass balance equations were used, and kept track of using an excel program such that the target composition and mass could be calculated quickly. An example of these calculations is seen below to calculate the total amount of graphite to add, incorporating the carbon content of the three ferroalloys used FeCr, FeMn and FeMo, in an attempt to reach 0.6wt% bulk carbon content in a 1kg batch. It should be noted that the prefix "C" is referring to the carbon content within the ferroalloy specified.

(17)

$$\text{Mass Graphite} = 1\text{kg}(0.006 - FeMn \times CFeMn - FeCr \times CFeCr - FeMo \times CFeMo + 0.001)$$

It was known through Stackpole Experience that the carbon content should be increased 0.1wt% above target due to the decarburization within the sintering furnace. There was also an addition of 0.7wt% of lubricant that is used consistently on the powder blends at Stackpole International.

The use of admixed elemental and ferroalloys were used in the production of test bars for *The Size Effect of the Base Powder on the Hardenability*, and *PM Steel as a Metal Matrix Composite* where prealloyed powder was used in *The Study of Porosity on Hardenability*.

In all three studies Cambridge materials was used to check the bulk concentrations of elements. They conformed to ASTM standards E1019-11, E1097-12 and E1479-16. These standards outline the appropriate use of determining the concentrations of alloying elements by means of combustion and infrared absorption, direct current plasma atomic emission spectrometer (DCP-AES) and inductively coupled plasma atomic emission spectrometer (ICP- AES) respectively[2]–[4].

7.1.3. Blending

The literature on powder segregation is mainly in the mm scale, and is therefore complicated to correlate to the micron size material used in the powder metal industry. It has been found that powders of different physical characteristics do not blend as well as powder similar in density, size and shape. There are two types of segregation defined by Parent in experiments using a horizontal rotating blender: Micro and Macro segregation. Micro-segregation refers to a difference in homogeneity on a particle-particle comparison, where the latter is defined as areas or regions having different amounts of constituents than others. Most models are derived from experiments using the same powder, coloured differently. One of these models can be seen in

Figure 52. Where the size and movement of the three layers shown are a function of the amount of material, mixer size, particle size, rpm of the mixer and the angle of repose (steepest angle found for the powder if it is allowed to be piled in one place) [5]. The Passive layer is subject to little movement, where powder moves slowly to the active layer. The shear or active layer is a smaller region, a couple of particle layers thick, where most movement occurs. The dead zone in the center can occur if too much powder is added to a blender designated for a smaller amount of powder, yet is not as apparent in more ideal situations [6].

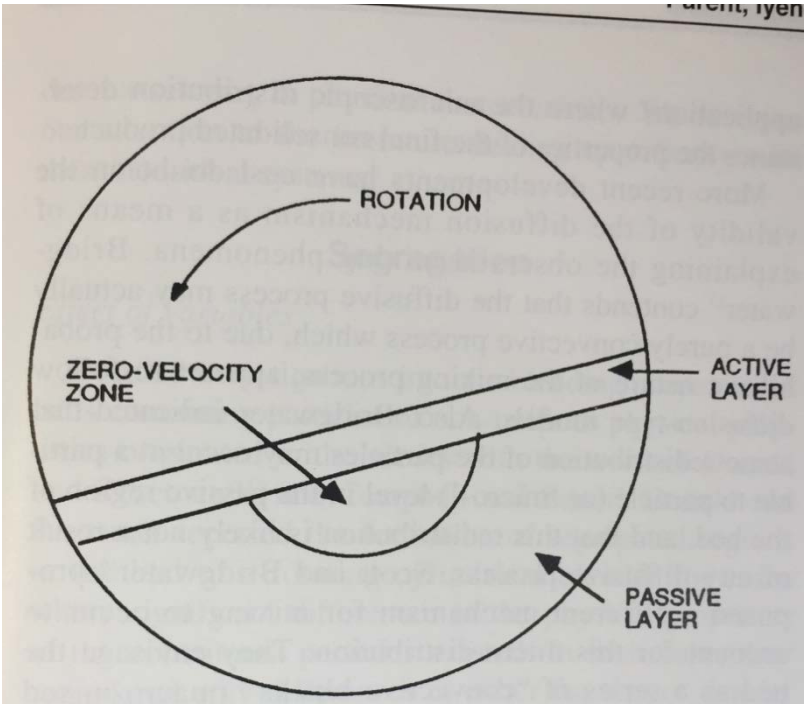

Figure 52: Blending model of similar particle sizes in horizontal cylindrical blender[6]

According to Lacey there are three mechanisms to powder mixing [6], [7]:

- Diffusion: The random motion of individual particles
- Convection: The motion of groups of particles that move together
- Shear: Regions of particles move according to a shear plane that was observed between sections of powder.

Other literature sources postulated the same mechanisms, along with postulating that the third mechanism is a combination of the diffusion and convective mechanisms working together. It was also suggested that the diffusion mechanism was the dominating factor, specifically in blends that involve mono-sized powders. In modeling this diffusion mixing it was also found that there was a relation to the number of rotations "N", which changed depending on short and long times of mixing. During short times the relation was $N^{1/2}$ where long mixing times depended on the Exp(N) [6], [7].

In the case of different sized particles it was theorized that smaller particles could get

caught in the active zone by falling into voids formed by this difference in size. Specifically in a ratio of density or size of greater than 1.2, macro-segregation occurred quickly [6].

It was also claimed that increasing this ratio would decrease the segregation, yet will increase the time needed to blend. This was specifically found when increasing the volume ratio of small vs coarse particles to 1. This is because a high packing factor of particles was observed in that smaller particles filled the voids between larger ones [6].

Even though the literature does not hold many concrete answers for mixing time, experience was used in blending at least 1 kg of powder in a *double cone mixer* for 45 minutes. This is done at Stackpole International, and produces consistent results.

7.1.4. Pressing

There is extensive effort in finding the compressibility of a powder, referring to the amount of pressure needed to produce a specific density for a greenbody and corresponding sintered part. Samples need to be pressed a known pressures, followed by density measurements before and after sintering. This project did not require this extent of information, and therefore employed a different methodology. Greenbody samples were pressed with a pressure suggested through our experienced counterparts at Stackpole International. The density was then checked, and the pressure was either increased or decreased to reach the target greenbody density.

The press itself is a unidirectional press that pushes a tool-steel plug into a die filled with a weighed amount of the blended powder. This occurs at room temperature.

7.1.5. Sintering

The high temperature sintering furnace was used at Stackpole International ant takes roughly five hours for a sample to completely move along the belt system into and out of the furnace. Figure 53 shows the thermal schedule for a sample moving through the furnace. The initial temperature at 900C is the opening stack burner, followed by the pre-

heat zone where temperatures slowly reach 775C. This is to burn off the lubricant within the part before sintering. The high heat zone then increases to 1280C for roughly 30 minutes in an Argon-5%Hydrogen atmosphere before slowly cooling. The range of temperatures shown by the error bars are from the industrial furnace specifications.

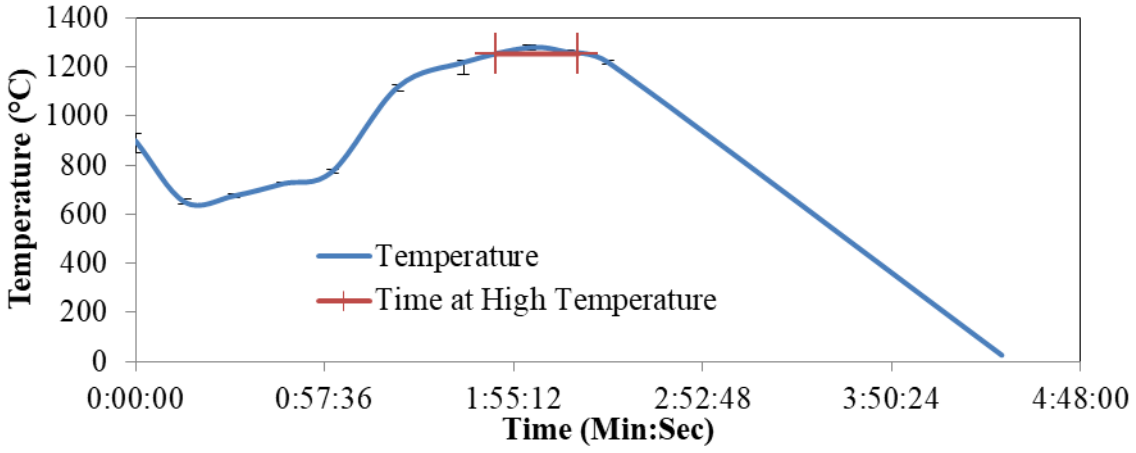

Figure 53: Sintering Temperature and Time Showing 35 Minutes above 1255ºC

7.1.6. Heat Treatment

7.1.6.1. Impact Bars

The impact bars were used in the PM Steel study in Chapter 5. After sintering the samples they were put through the industrial heat treatment shown in Figure 54 for through hardening. The initial preheating of the chamber is shown, as well as the decrease when the samples are placed into the chamber. It can be seen that there is sufficient time at 900C (75 minutes) to form the austenitic phase. This time might seem excessive at first, yet since they were industrially sintered a full furnace of components accompanied them and therefore this time is warranted to ensure a complete austenitic phase transition for every part. The atmosphere is primarily nitrogen at a very low atm, 0.01atm, to remove any residual gasses from the parts and to insure no oxidation or decarburization during the thermal treatment. The quench is completed in 12 minutes, at a rate of 73C/min using

18.26atm of cooled helium. The slight tempering stage is completed to remove internal stresses from the parts that could have occurred during the aggressive quench.

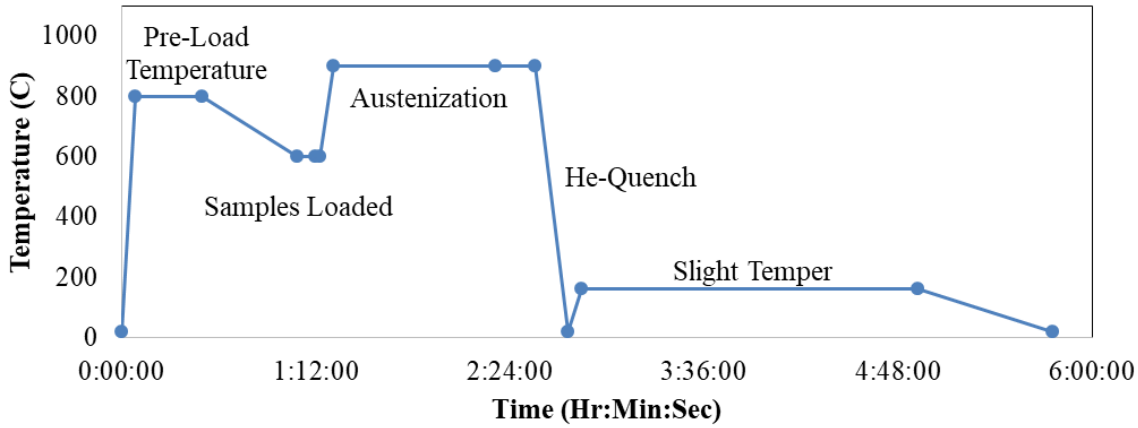

Figure 54: Austenitization and Quench of Impact Bars

7.1.6.2. Jominy

The Jominy test was completed in accordance to ASTM-A255-10[8], as well as MPIF standard 35 and 65 [9]. The heat treatment seen in Figure 55 is an example of the many Jominy heat treatments completed for this project, specifically found experimentally for the size effect project seen in Chapter 4. ASTM A255 specifies that steel with carbon contents above 0.50wt% that the furnace temperature must be 900C, and the sample must be held within a carbon neutral atmosphere for 30 minutes[8]. This is to stop any decarburization through the heat treatment, and was accomplished by surrounding the sample in pitch coke. The endothermic phase change can be observed at the intersection of the Thermo-Calc predication and the temperature. After the 30minutes the sample was quickly removed (under 5 seconds) and placed within the Jominy quench tank where water is sprayed from a 12.7mm diameter orifice at one side of the cylinder as also shown in Figure 55.

It is interesting to note that the thermocouple, which was placed beside the Jominy bar, was able to measure the change in heat associated with the phase change to austenite. This can be seen by the tip in the temperature curve, which aligns very closely to the projected austenization temperature found by Thermo-Calc.

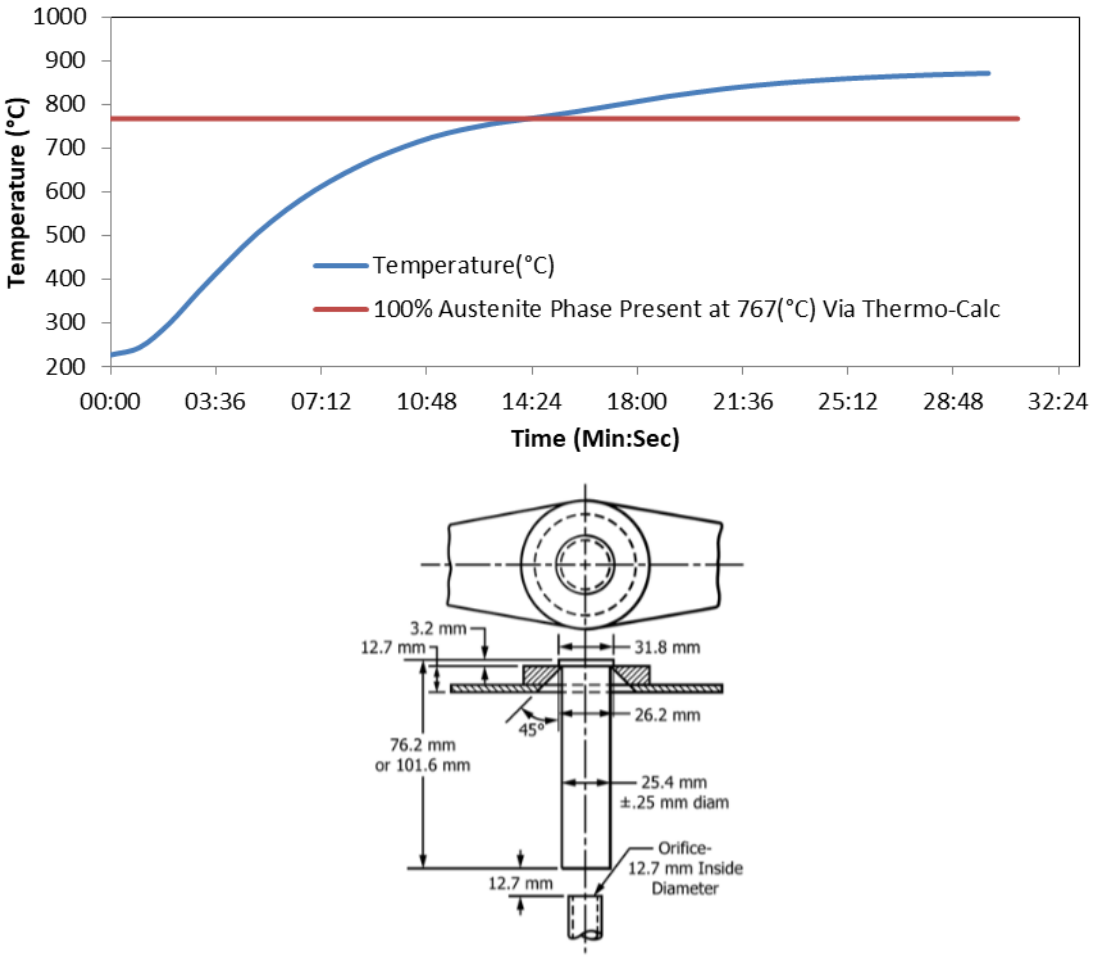

Figure 55: Jominy Bar Heating to reach Austenitic phase before End Quenching and End Quench schematic [8]

7.1.7. Density - Archimedes Principle

The apparent density found via the Archimedes principle can be seen in (18) that relates the weight of the sample "M" to the weight of the sample under water "M_w" and density

of the liquid "p_l" it is submerged in to find the density of the sample "p". Using the found water temperature, to get the exact density of the water, the density of the green body can be found. A similar method is used in finding the sintered density, except first the samples are impregnated with oil by submerging them and placing them in a vacuum chamber to force air out of the pores, and oil into the sample. After this has been completed (30-45 minutes) the Archimedes method can be used. This methodology is in line with MPIF standard

ASTM B328 was specifically used but essentially specifies the same methods as set forth in MPIF standards 42 and 57.

(18) $$\rho = \frac{M \rho_l}{M - M_w}$$

7.2. Microscopy

7.2.1. Polishing Methodology

The polishing method utilized was an industrially suggested technique for sintered steels. The presence of voids creates the need for a meticulous procedure to stop the formation of over or under polishing blemishes. These can be seen in Figure 56, showing how removing too much material, or not enough, will result in a misrepresentation of the porosity.

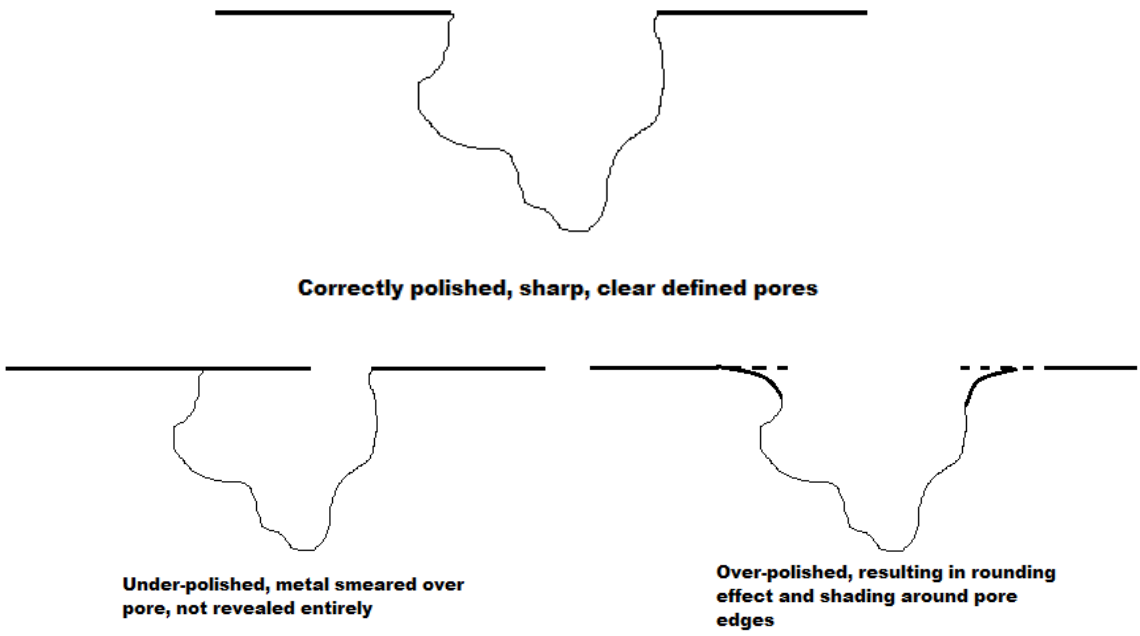

Figure 56: A properly polished pore vs an under and over-polished one [10]

7.2.2. Etching

After polishing samples were etched to reveal the microstructure. 2% nital was used to reveal the general structure and grain boundaries as stated for tempered steel from ASTM-E407[11]. Porous material etches very quickly around pores, and therefore samples were submerged or covered for one to two seconds before water or ethanol rinsed.

7.2.3. ImageJ Procedure for Total Pore-Area Calculation

To produce the ImageJ data seen in the above report the following procedure was followed:

The SEI image seen in Figure 57 is an example of a starting image and was used due to the edge charging effects around the pores gave a large enough contrast to differentiate the boundaries. The internal scale was set to the 500-micron scale of the image, and then

the scale area was taken away as to not effect the final data. The background was then subtracted creating Figure 58.

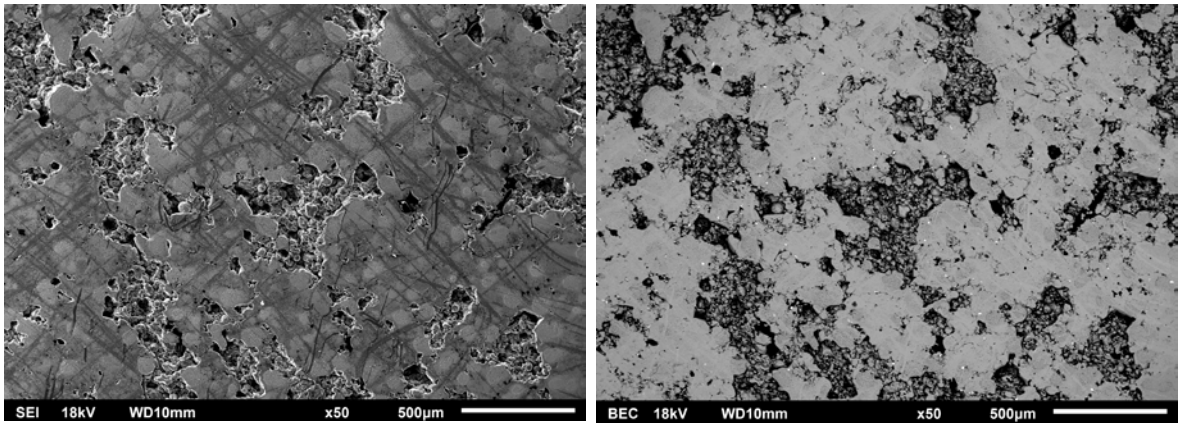

Figure 57: SE-SEM Micrograph (left) and BSE-SEM Micrograph (right) at 50X Magnification on Greenbody PM Coupon

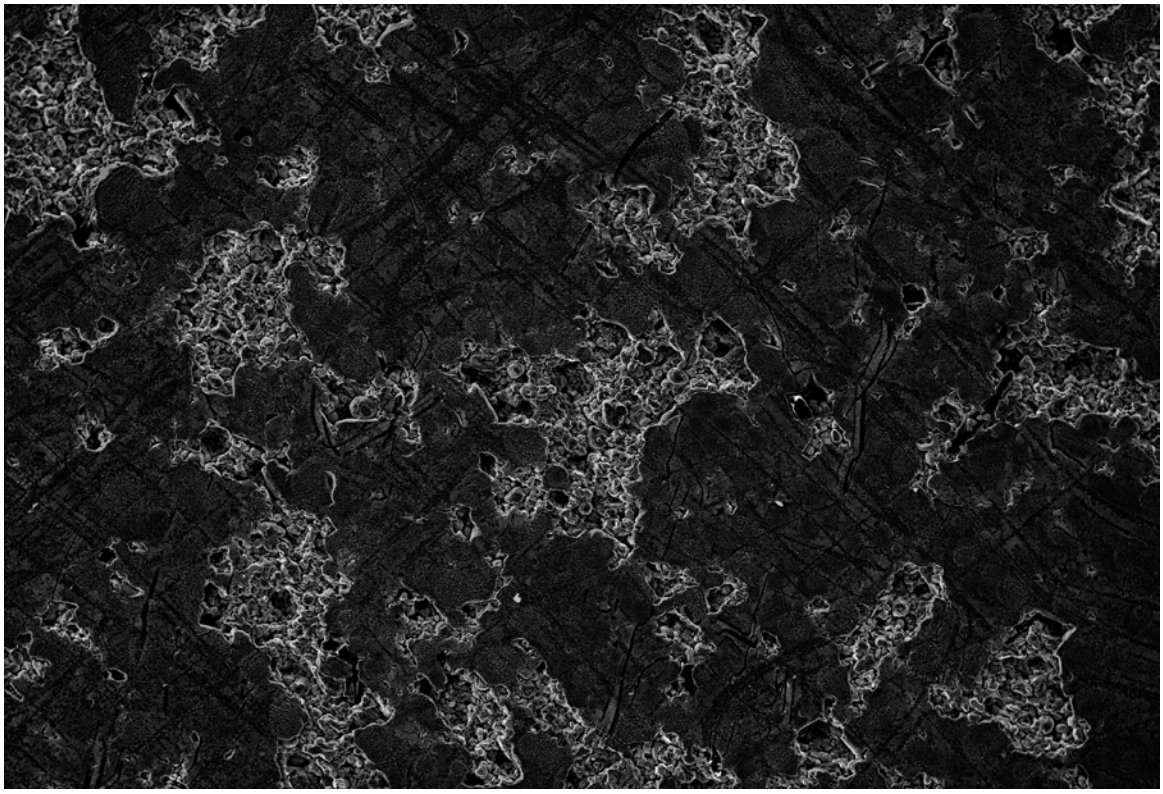

Figure 58: SE Image from Figure 57 after the background was subtracted

Next the image was processed using the threshold feature to produce a two-tone black and white image shown in Figure 59. This allowed for the software to calculate the size of the pores.

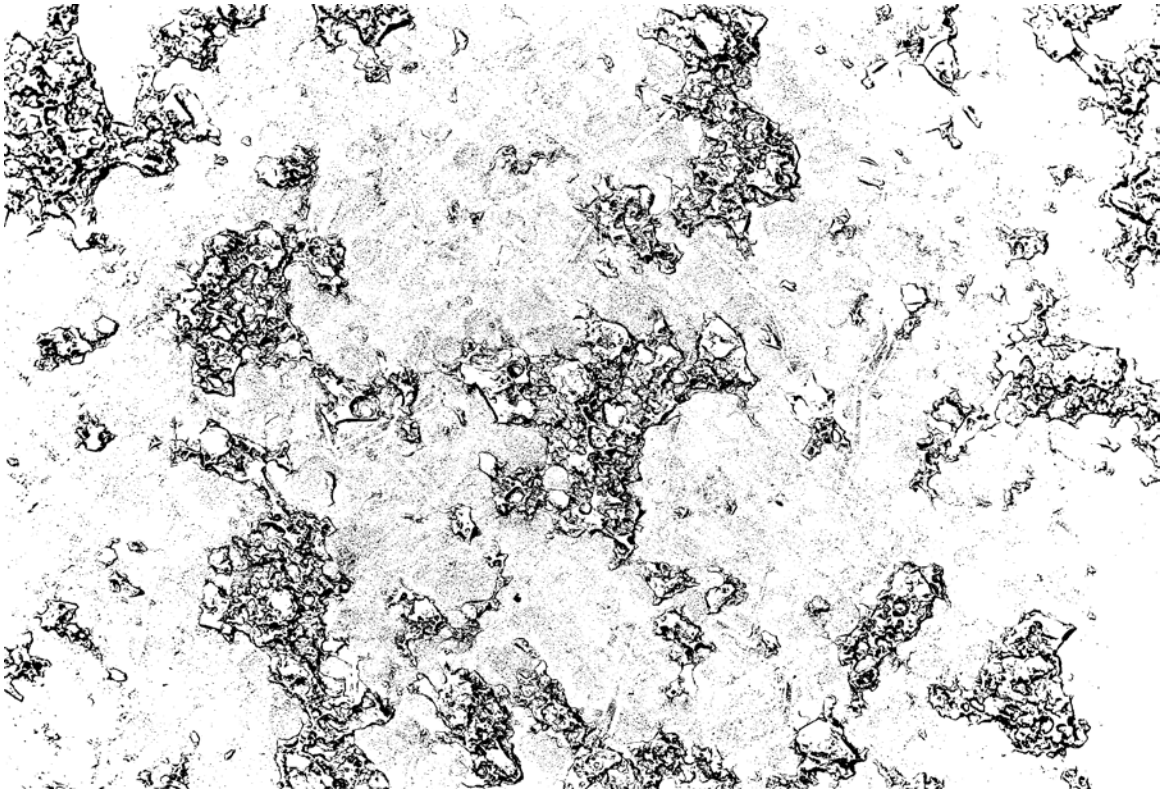

Figure 59: Threshold used to form black and white image

When using the software the minimum size of the pore was set to 10 microns in diameter by setting the minimum area to $78.5\mu^2$. Anything smaller than this will most likely be an effect from the threshold feature misreading small areas of pixels and changing the data. This produces the information explained, along with Figure 60. Once this image is produced the area within each particle is found and outputted as a text file to be imported to excel for further analysis.

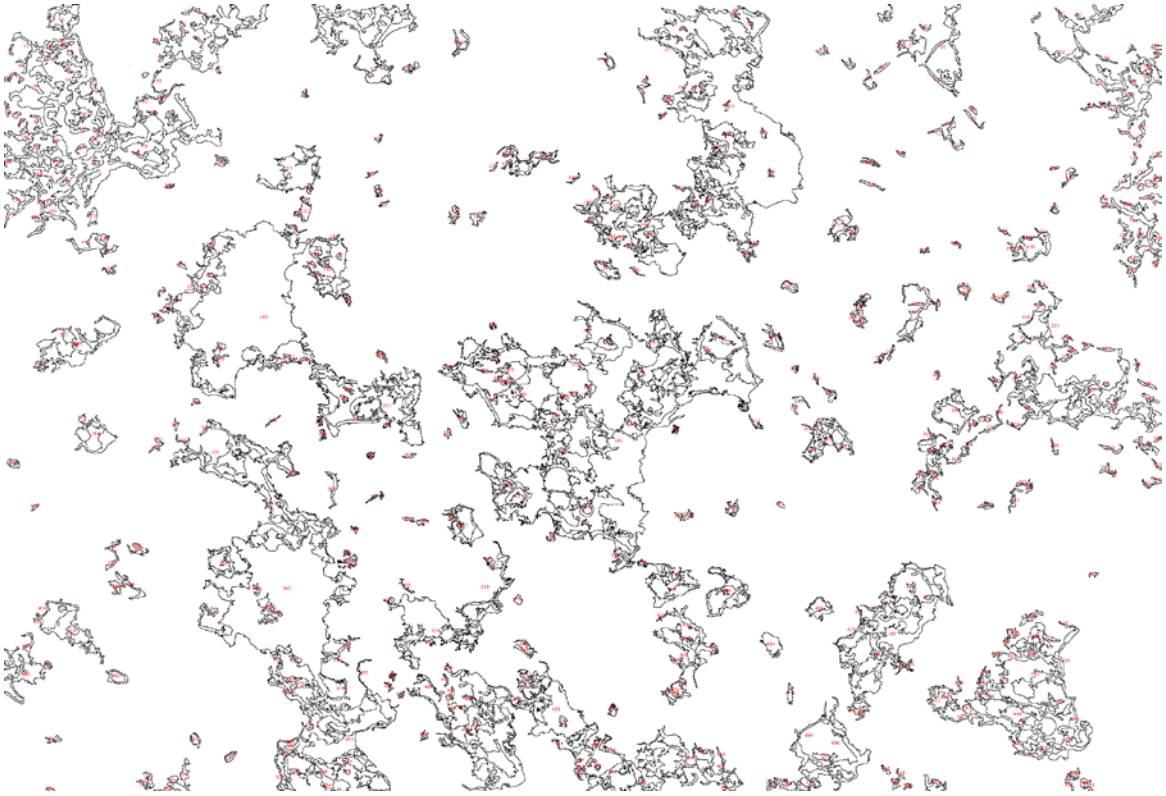

Figure 60: SE image Re-drawn, highlighting pores for counting and area analysis

7.3. WDS measurements

Wavelength dispersive spectroscopy was used, which is a method of X-ray analysis which births quantifiable date. This was done at Western University by the kind assistance of the geological department. First specific elements relative to what was going to be mapped were used to produce computational standards, and to find the X-ray peak by moving the WDS crystal. This method is very time intensive, yet can show results as low as 100ppm [12].

WDS and EDS works by the formation of X-rays caused from the removal and replacement of electrons from the atoms in the sample's crystal lattice. An electron beam is used to remove electrons from atomic shells; once this "hole" is filled a corresponding X-ray is released that is characteristic to the element. In EDS all X-rays are collected through one detector and converted to a quantity of elemental atoms. In WDS there are many detectors that have the ability to pick up a single wavelength corresponding to a

specific element within the sample. This allows for higher definition, and more accurate data.

Figure 61 shows an example of WDS maps of a sample that was industrial sintered in a high temperature furnace. The initial Ni particles were significantly small (below 45 microns in diameter) which is commonly used in industry. Even though the initial size was small, it can still be seen that the pure Ni powder was not able to completely diffuse into the surrounding Fe matrix. The fine iron matrix also contributed to the overall uniformity of the alloying elements, such that smaller initial particles shows qualitatively a uniform distribution of Mn, Cr and Ni. With this information it can be speculated that with fine Fe and fine Ni a larger fraction of martensite could form than coarse Fe and fine Ni. It should also be noted the difference in grain size and porosity, where small pores and grains are produced with fine initial Fe powder.

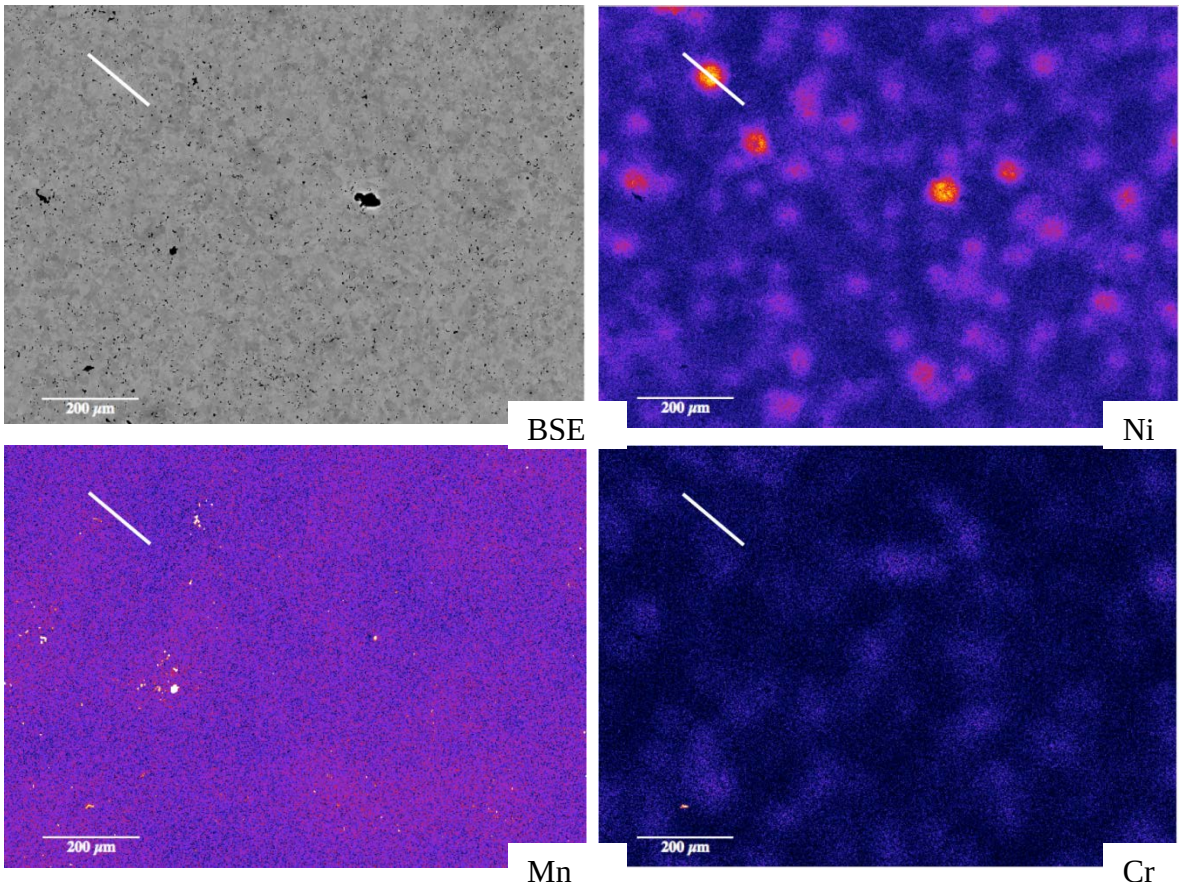

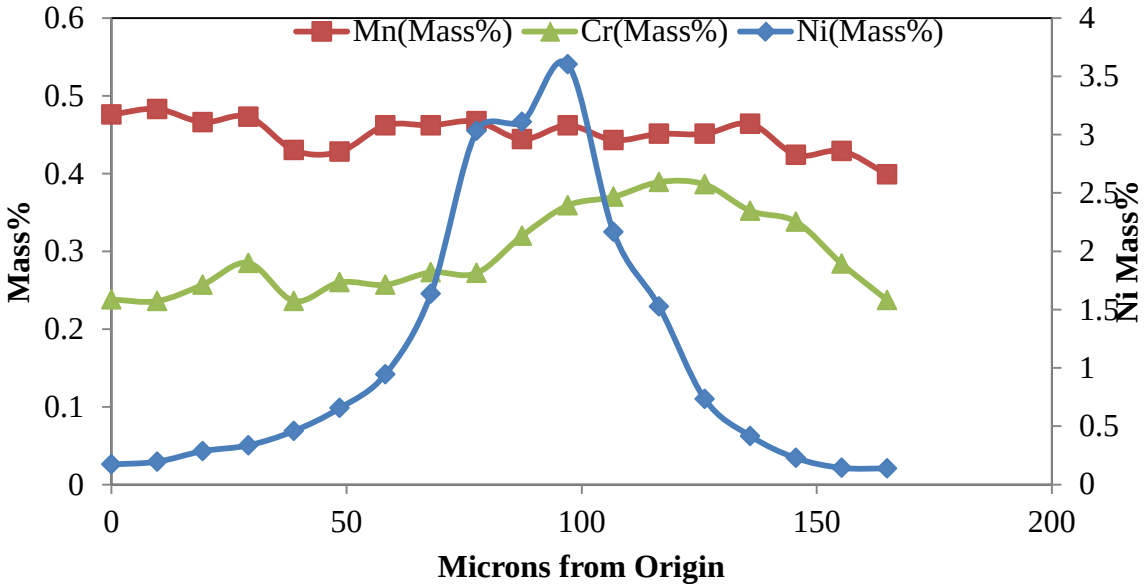

Figure 61: WDS maps of a Sintered PM Part made from Fine Fe and Ni Powder (Less than 45 Micron in diameter)

7.4. The Determination of MMC Mechanical Properties

7.4.1. Tensile Testing

The impact bars produced for the PM Steel as a MMC study were machined into round tensile bars with the dimensions in Figure 62[6]. Figure 62 was created by Stackpole International, optimizing the specimen after every test batch. They were tested at room temperature in accordance with ASTM E8/E8M-16a [13].

[6] Machining and testing was completed by Exova in Mississauga, Ontario

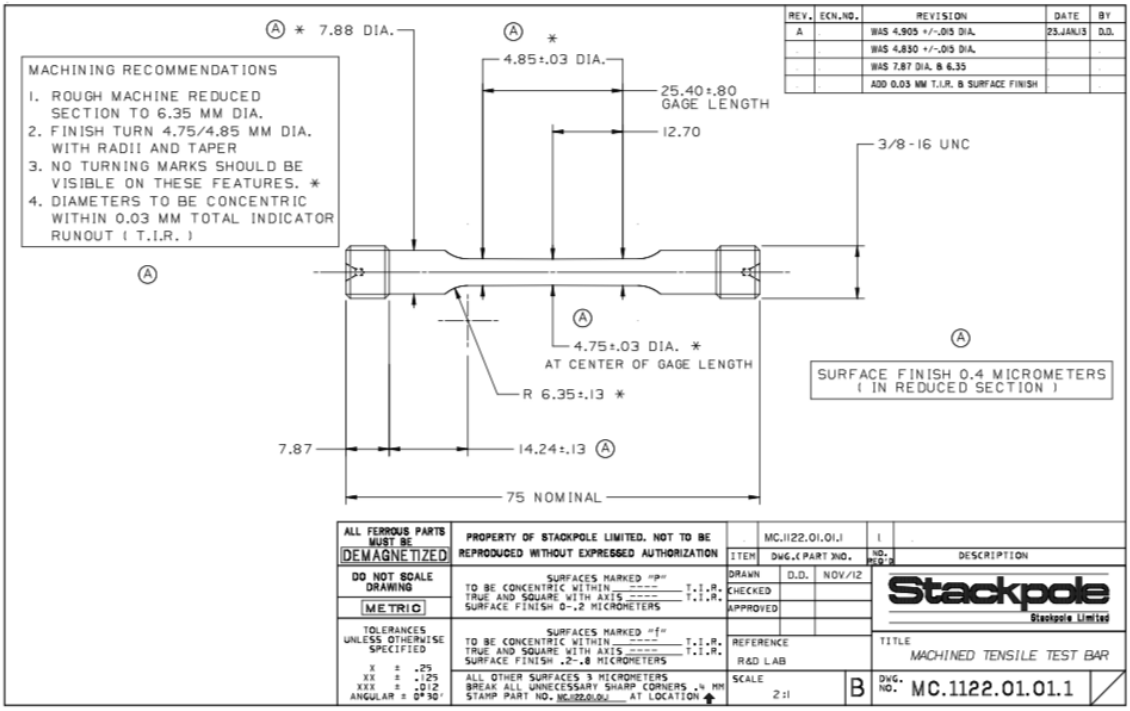

Figure 62: Design specification for the tensile specimens manufactured by Exova, addition of polishing surface to 4μm finish.

7.4.2. Charpy Samples

Chary samples were manufactured in accordance with ASTM 370 as shown in Figure 63.

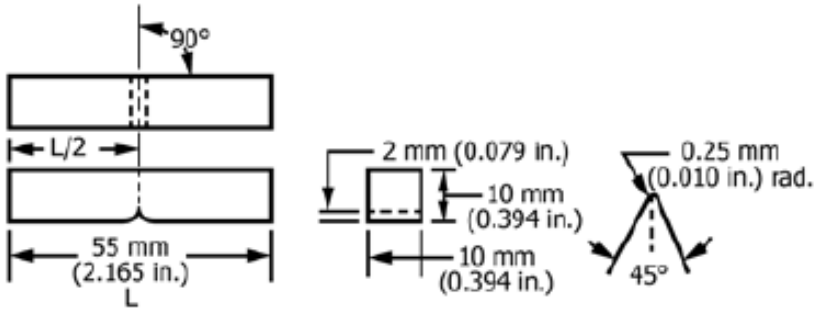

NOTE 1—Permissible variations shall be as follows:

Notch length to edge	90 ±2°
Adjacent sides shall be at	90° ± 10 min
Cross-section dimensions	±0.075 mm (±0.003 in.)
Length of specimen (L)	+ 0, – 2.5 mm (+ 0, – 0.100 in.)
Centering of notch (L/2)	±1 mm (±0.039 in.)
Angle of notch	±1°
Radius of notch	±0.025 mm (±0.001 in.)
Notch depth	±0.025 mm (±0.001 in.)
Finish requirements	2 µm (63 µin.) on notched surface and opposite face; 4 µm (125 µin.) on other two surfaces

Figure 63: Charpy samples as stated by ASTM 370 in figure 11 for full size samples [14]

7.4.3. Microhardness

Microhardness measurements were taken on unetched surfaces when possible. It was unavoidable during the MMC study because the difference in microsctruures what we were looking for.

7.4.4. Rockwell

There was extensive work in using the Rockwell machine for all three projects. It was used in accordance with ASTM E18-17 [15]. Specifically Rockwell A and C were observed, which both use a 120 degree diamond indenter, with 60kg and 150kg forces respectively. Figure 64 shows the general principal of the test. The first loading step applies 10kg to measure the baseline of depth to be used later. The second step in releasing the load will apply the force, driving the indenter into the specimen. In the last step the force is removed, and the hardness measured is an inverse relation to the depth from the baseline to this depth [15].

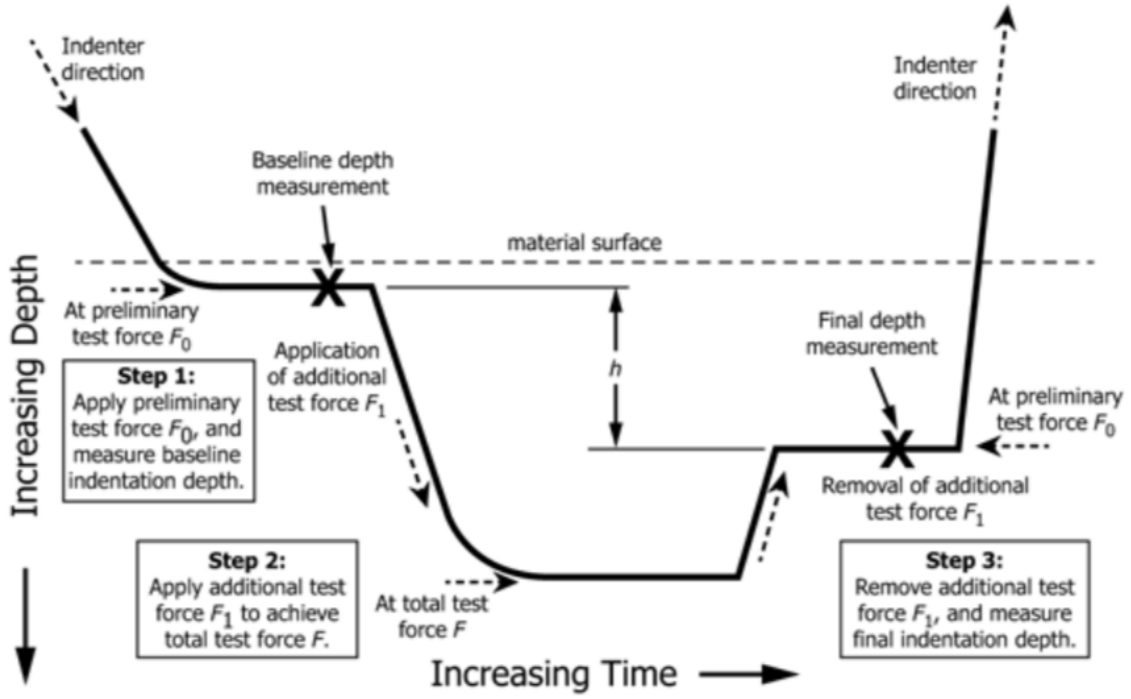

Figure 64: Rockwell hardness test as per ASTM E18-17 showing the three major steps of the test [15]

7.5. Specific Assumptions and Conditions for Simulated Values

7.5.1. ASTM values and equations

Table 11 is from ASTM A255-10 [8], and shows how the multiplying factor is calculated per alloying element. Since these relations were found experimentally, the calculation changes depending on the concentrations, and only work for specific ranges. In producing the ASTM calculator for these projects the formula had to change depending on the inputted concentration. This was completed with nested IF statements within excel such that the entire range of able concentrations was covered.

Table 11: Range of Steel Factors for ASTM A255 Jominy Hardenability Calculations[8]

Carbon/Grain Size 7	
Up to 0.39 %, incl	MF = 0.54 (%C)
Over 0.39 to 0.55 %, incl	= 0.171 + 0.001 (%C) + 0.265 (%C)^2
Over 0.55 to 0.65 %, incl	= 0.115 + 0.268 (%C) – 0.038 (%C)^2
Over 0.65 to 0.75 %, incl	= 0.143 + 0.2 (%C)
Over 0.75 to 0.90 %, incl	= 0.062 + 0.409 (%C) – 0.135 (%C)^2
Manganese	
Up to 1.20 %, incl	= 3.3333 (%Mn) + 1.00
Over 1.20 to 1.95 %, incl	= 5.10 (%Mn) – 1.12
Silicon to 2.00 %, incl	= 1.00 + 0.7 (%Si)
Nickel	
Up to 1.50 %, incl	= 1.00 + 0.363 (%Ni)
Over 1.50 % to 3.5 %, incl	= 0.3211 + 1.4501 (%Ni) – 0.6119 (%Ni)^2 + 0.1253 (%Ni)^3
Chromium to 2.50 %, incl	= 1.00 + 2.16 (%Cr)
Molybdenum to 0.55 %, incl	= 1.00 + 3.00 (%Mo)
Copper to 0.55 %, incl	= 1.00 + 0.365 (%Cu)
Vanadium to 0.20 %, incl	= 1.00 + 1.73 (%V)
Zirconium to 0.25 %, incl	= 1.00 + 2.5 (%Zr)

7.6. Densification Summary Table

Table 12: Factors that affect Densification Rate and Magnitude [16], [17], [18], [19]

Factor	Densification	
	Rate (d□/d*t*)	Magnitude (d □)
Higher sintering temperature	Increase	Increase
Higher heating rate	Increase	Increase
Higher compacting pressure	Increase	Decrease
Liquid phase sintering	Increase	Increase
Reducing atmosphere		Increase
Sintering time increase		Slight Increase
Annealed powder		Decrease
Mono-particle size distribution		Increase
Smaller particles or increase in powder's specific surface	Increase	Increase
Promoting a ferrite phase		Increase

7.7. References

[1] ASTM International, "Standard Test Method for Sieve Analysis of Metal Powders." ASTM International, West Conshohocken, PA, 2016.

[2] ASTM International, "Standard Test Methods for Determination of Carbon, Sulfur, Nitrogen, and Oxygen in Steel, Iron, Nickel, and Cobalt Alloys by Various Combustion and Fusion Techniques." ASTM International, West Conshohocken, PA.

[3] ASTM International, "Standard Guide for Determination of Various Elements by Direct Current Plasma Atomic Emission Spectrometry1." ASTM International, West Conshohocken, PA.

[4] ASTM International, "Standard Practice for Describing and Specifying Inductively-Coupled Plasma Atomic Emission Spectrometers1." ASTM International, West Conshohocken, PA.

[5] “Definition of ANGLE OF REPOSE.” [Online]. Available: https://www.merriam-webster.com/dictionary/angle+of+repose. [Accessed: 2017-04-11].

[6] G. J. . Parent, J. Lyengar, and H. Henein, “Fundamentals of Dry Powder Blending for Metal Matrix Composities,” *Int. J. Powder Metall.*, vol. 29, no. 4, 1993.

[7] P. M. . Lacey, “Developments in the theory of particle mixing,” *J. Appl. Chem.*, vol. 4, p. 257, 1954.

[8] ASTM International, “Standard Test Methods for Determining Hardenability of Steel.” ASTM International, West Conshohocken, PA.

[9] MPIF, “MPIF Standard 35.” Metal Powder Industries Federation, 2012.

[10] Katherine Jarzecki, B.Eng, B.Sc, “Powder Metal Preparations,” Stackpole International, 17-Jan-2016.

[11] ASTM International, “Standard Practice for Microetching Metals and Alloys.” ASTM International, West Conshohocken, PA, 2015.

[12] Joseph I. Goldstein, Dale E. Newbury, Patrick Echlin, David C. Joy, Charles Fiori, and Eric Lifshin, *Scanning Electron Microscopy and X-Ray Microanalysis*. 233 Spring Street, New York, N.Y. 10013: Plenum Press, 1981.

[13] ASTM International, “Standard Test Methods for Tension Testing of Metallic Materials.” ASTM International, West Conshohocken, PA.

[14] ASTM International, “Standard test Methods and Definitions for Mechanical Testing of Steel Products.” ASTM International, , 100 Barr Harbor Drive, PO Box C700, West Conshohocken, PA.

[15] ASTM International, “Standard Test Methods for Rockwell Hardness of Metallic Materials.” ASTM International, West Conshohocken, PA.

[16] Andre Salak, *Ferrous Powder Metallurgy*. 7 Meadow Walk, Great Abington, Cambridge CB1 6AZ, England: Cambridge International Science Publishing, 1995.

[17] Q.H. Zou, H. M. Zhao, D.Y. Zhang, M. Geng, Z.G. Wang, J.J. Lu, "Thermophysics characteristics and densification of powder metallurgy composites," *Powder Metall.*, vol. 49, no. 2, pp. 183–188, 2006.

[18] Kishor M.Kulkarni, "Effect of Particle Size and shape on Sintering of high Speed Steels," *Mod. Dev. Powder Metall.*, vol. 19, 1988.

[19] P. R. Kalischer, "The Effect of Particle Size on the Shrinkage of Metal Compacts," *Symp. Powder Metall. Am. Soc. Test. Mater.*, pp. 31–40, Mar. 1943.

[20] G.F. Bocchini, B. Rivolta, G. Silva, M.G. Ienco, M.R. Pinasco, and E. Stagno, "Influence of density and surface/volume ratio on the cooling speed of sinter-hardening materials," *Adv. Powder Metall. Part. Mater.*, pp. 60–72, 2002.